Dissertation

submitted to the

Combined Faculty of Mathematics, Engineering and Natural Sciences

of Heidelberg University, Germany

for the degree of

Doctor of Natural Sciences

Put forward by

Ekaterina Magg

born in Kostroma

Oral examination: 01.02.2023

CONSTRAINING STELLAR PHYSICS WITH THE NLTE RADIATIVE TRANSFER

Referees Dr. Maria Bergemann

PD. Dr. Andreas Koch-Hansen

ABSTRACT

All chemical elements in the Universe, except the very few lightest species, are produced in a nuclear fusion inside the stars. Following the stellar life cycle, these chemical elements are expelled into the interstellar medium where they proceed to contribute to the chemical enrichment of their surroundings. Spectroscopic observations are currently the only way to infer the chemical make-up of the stars. Combining those with the physical modelling of the radiation in the stellar plasma allows us to detect and measure the number of chemical elements we all are made of. The approach is generally applied to individual stars constituting the larger scale populations, from clusters to galaxies including our Milky Way and beyond.

In this thesis I focus on the non-equilibrium modelling of stellar radiation and its influence on the measured chemical abundances of various elements. I provide a general overview of the methods and necessary information used to infer the stellar chemical composition. I then present developments in the non-equilibrium modelling and apply it to the analysis of a star cluster, our host star – the Sun, and eventually a broader Galactic population. I focus on the opportunities our modelling approach presents to observationally constrain the stellar evolution and consequential enrichment of the Galactic populations.

ZUSAMMENFASSUNG

Alle außer den leichtesten chemischen Elementen im Universum entstehen durch nukleare Fusion im Inneren von Sternen. Im Lebenszyklus der Sterne werden diese chemischen Elemente in das interstellare Medium ausgestoßen, wo sie zu chemischen Anreicherung der Umgebung beitragen. Spektroskopische Beobachtungen sind gegenwärtig die einzige Methode, um Rückschlüsse auf die chemische Zusammensetzung der Sterne zu ziehen. Die Kombination dieser Beobachtungen mit physikalischen Modellen der Strahlung im stellaren Plasma erlaubt uns die Häufigkeit der chemischen Elemente aus denen wir alle bestehen zu messen. Dieser Ansatz wird im Allgemeinen auf einzelne Sterne, die die größeren Populationen, von Sternhaufen zu Galaxien einschließlich der Milchstraße und darüber hinaus bilden, angewendet.

In dieser Arbeit liegt der Schwerpunkt auf der Nicht-Gleichgewichts-Modellierung von stellarer Strahlung und auf ihrem Einfluss auf die gemessenen chemischen Häufigkeiten verschiedener Elemente. Ich beginne mit einem allgemeinen Überblick über die Methodik und notwendige Informationen, die zur Bestimmung der stellaren Zusammensetzung benutzt werden. Im Anschluss präsentiere ich Entwicklungen in der Nicht-Gleichgewichts-Modellierung und ihrer Anwendung auf die Analyse eines Sternhaufens, unseres Sternes – der Sonne, und abschließend auf eine breitere galaktische Population. Die Möglichkeiten zur Eingrenzung stellarer Entwicklung und auch der Anreicherung unserer galaktischen Population, die unser Modellierungsansatz eröffnet, liegen hierbei im Fokus.

Contents

1

Introduction and motivation

If the weather allows, looking up the sky one sees plenty of the brightest, closest to us stars in the Universe as tiny white dots. The light they emit comes from the non-stop running nuclear fusion in the stellar core, counteracted by gravity. Understanding of light changed drastically in 1670s, when Isaac Newton observed that white light decomposes when passing through a triangular piece of glass – a prism – and produces a multicoloured image. Newton named that image a *spectrum*. A century later, the skilled glass maker Joseph von Fraunhofer combined prisms with a telescope, which allowed him to observe dark features in the other than that continuous spectrum from planets and stars other than our Sun. We now know that these dark features – known as *spectral lines* – are in fact the unique fingerprints of chemical elements present in the cosmic matter.

As energy released in the internal fusion passes through the stellar matter – hot ionised plasma – it goes through a number of processes. These processes define the shape of the stellar spectrum and leave their characteristic imprint in the stellar light in the form of, e.g., absorption lines. The ability to study these rich processes by looking at spectroscopic observations makes stellar spectroscopy one of the most powerful tools of modern astronomy. In fact, we can only 'see' the outermost, thin layer of a star – also known as a *photosphere*: $\phi\omega\tau o\zeta$/phos meaning 'light' and $\sigma\varphi\alpha\iota\rho\alpha$/sphaira meaning 'sphere'. Continuous light gets scattered, absorbed and re-emitted at particular frequencies, corresponding to the energy

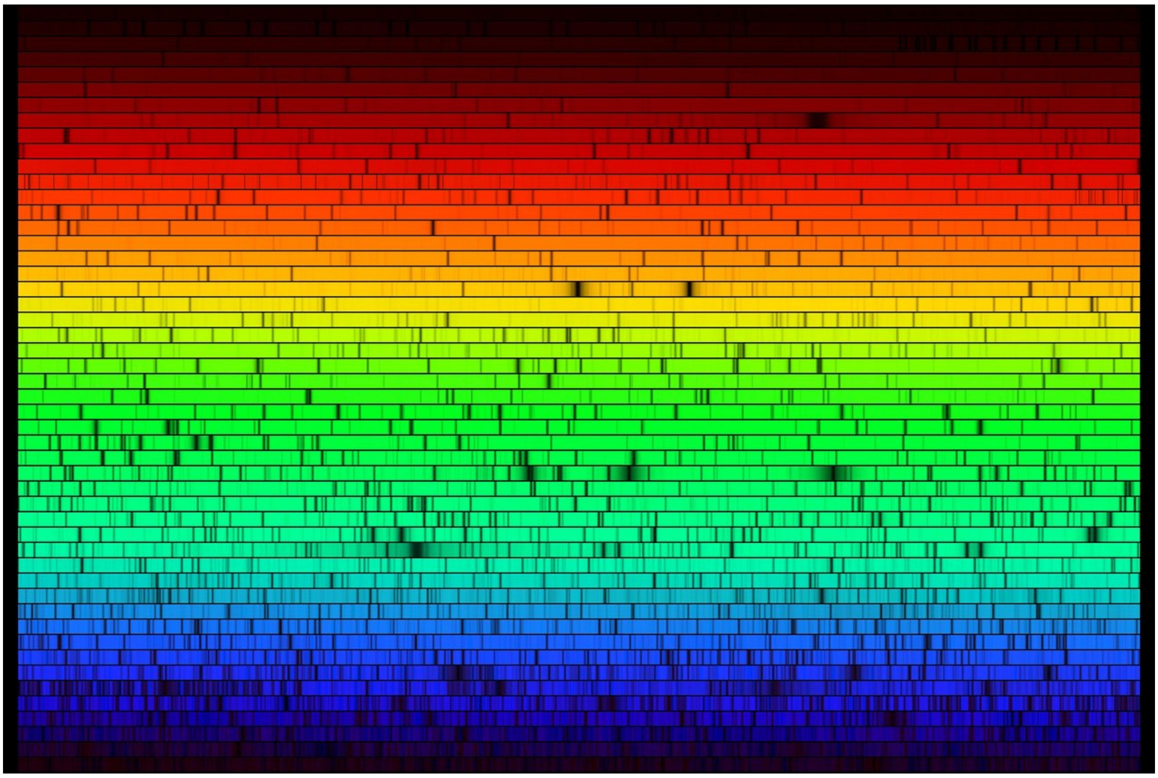

Figure 1.1: The Sun's spectrum contains dark lines, produced when gases in the atmosphere absorb specific wavelengths of light. Credit: NASA/SDO

structure of atoms and molecules in the stellar plasma, thus forming spectral lines. By comparing observed spectral lines to model predictions we can infer the stellar *composition* and the corresponding *abundances* of individual chemical elements comprising the matter.

1.1 OUTLINE

This thesis is organised as follows. In this Chapter (1), I discuss the importance of stellar abundances for the big picture in astronomy. In Chapter 2, I provide a more technical overview of the methods used to infer stellar abundances by modelling stellar radiation. I will primarily focus on not assuming local thermodynamic equilibrium (NLTE) methods for modelling and its advantages compared to the assumption of local thermodynamic equilibrium (LTE). In Chapter 3, I applied the NLTE modelling to derive the chemical composition of a uniform stellar population – a star cluster – to interpret the interplay of the secular evolution processes in the stellar interiors. In Chapter 4, I focus on the chemical composition of our most important star, an anchor to any other star in the Universe – the Sun. I present the most recent NLTE computations for Ni in Chapter 5 in context of the Galactic chemical evolution studies. Chapter 6 provides a short summary of the work in this thesis and an outlook on future developments in the field.

1.2 Cosmic nucleosynthesis

In the big bang nucleosynthesis only the light elements, namely hydrogen, helium as well as trace amounts of lithium and beryllium, are believed to have formed (Burbidge et al., 1957). All heavier elements – called *metals* in astronomical jargon – trace their origin to highly energetic processes occurring within stars, during supernova (SN) events and a small number of additional processes. A detailed picture of these processes and where each element originates can be found, e.g., in Kobayashi et al. (2020). For a graphical summary of cosmic nucleosynthesis, see Fig. 1.2.

Figure 1.2: Periodic table showing the origin of elements.

As the gradual build-up of heavy elements is one of the most ubiquitous features of our Universe, stellar chemical abundances act as lens through which we can investigate the history and the processes occurring in the Universe. In this Chapter, I will give a brief overview of the areas of astronomy that rely most heavily on the study of stellar abundances.

But before we turn to the application of abundance measurements, allow me to briefly review the origin of chemical elements and the commonly accepted classification based on their formation. Chemical elements are usually grouped in the following way [1]:

Light elements

Only the lightest elements, such as hydrogen, helium, and traces of lithium and beryllium, formed in the big bang nucleosynthesis (Burbidge et al., 1957). Their exact abundances are dependent on the cosmological parameters and can therefore be used to to constrain these. Due to their primordial origin and their low atomic numbers these elements are usually referred to in astronomy as light elements or non-metals.

CNO elements

Elements heavier than helium, or metals, are formed by fusion of lighter elements in stars during the many stages of their evolution. It starts with the fusion of hydrogen to helium. In stars as heavy as the Sun this process mainly (also see Borexino Collaboration et al., 2020) occurs via the so-called proton-proton chain, whereas in heavier stars the CNO-cycle dominates. As the name suggests this process cycles through various isotopes of carbon, nitrogen and oxygen while converting hydrogen to helium. Thus, these three elements, carbon, nitrogen and oxygen, are found to commonly occur together.

α elements

Once the supply of hydrogen in the stellar core is exhausted, next in line elements start to form by the fusion of helium nuclei. Since the helium nucleus, consisting of two protons and two neutron, is known as α-particle, chemical elements which form by fusion processes involving He nuclei are referred to as α-elements. The first particle forming this way is ^{8}Be, which is extremely unstable with a half lifetime of $\approx 10^{-17}$ seconds. It therefore decays almost immediately into smaller nuclei, unless the third α-particle fuses with it in time forming an excited resonance state of ^{12}C known as the Hoyle state. Most of the times excited ^{12}C will quickly decay back into the three α-particles, but approximately in 0.04% of decays it will convert into ground state of ^{12}C by emitting an electron from the atom. This process is know as the triple-α process and it forms ^{12}C – the lightest α-element. Following the formation of carbon, through repeated capture of α-particles, oxygen, neon, magnesium, silicon, sulfur, argon, calcium, titanium, chromium, and iron are formed. This gradual build-up of elements is known as α-process or α-ladder. Since nuclear statistical equilibrium

---

[1] *The following compressed description of cosmic nucleosynthesis is based on Kippenhahn et al. (2012).*

processes becomes dominant for the heavier nuclei, among these only the elements up to calcium or titanium are usually referred to as α elements. This chain effectively stops at iron, as conditions in stellar interiors lead to photo-disintegration of elements heavier than iron.

Iron peak

Iron and nickel possess the most tightly bound nuclei and effectively stop the build-up of elements by capturing α-particles. Elements with tightly bound nuclei, e.g. Cr, Mn, Fe, Co and Ni, are produced in highly energetic events like SNe, where hot dense material allows nucleosynthesis to occur freely and matter finds nuclear statistical equilibrium. High nuclear stability leads to this group of elements being relatively common and to form a peak in abundances around iron, as shown in Fig. 1.3, resulting in them known as iron-peak elements.

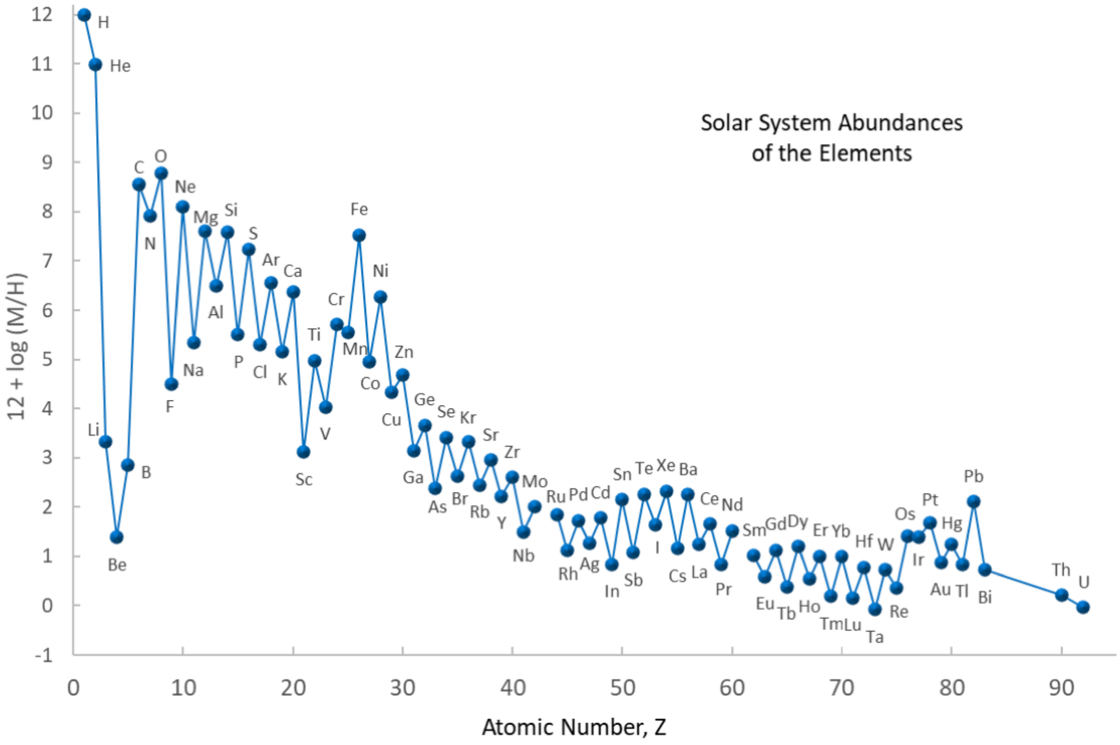

Figure 1.3: Solar system abundances of the elements as a function of atomic number. Adopted from Lodders (2019).

Neutron capture

Heavier elements, and those in between the α elements, form via repeated capture of neutrons and follow-up β decays. This process occurs for example in SNe and neutron star mergers. The neutron capture process is further grouped into the rapid (r-) and the slow (s-) neutron capture process. During the slow neutron capture a nucleus captures a single neutron at a time and, if the formed nucleus is unstable, quickly decays before encountering the next neutron. This occurs at low density of the neutron flux. In contrast, at high neutron flux density, nuclei capture multiple neutrons with no time to decay in between. Once the supply of neutron runs out, highly unstable nuclei decay into stable isotopes via multiple β-decays.

1.3 The Role of Stellar Abundances in Astronomy

1.3.1 First stars in the Universe

The most metal-poor stars have often been found to show peculiar abundance patterns (e.g. Frebel et al., 2005, Keller et al., 2014). These abundance patterns are thought to be the imprint of their birth environment. While these environments are long gone, they can still be studied by analysing abundance patterns of the most metal-poor stars in a field commonly referred to as stellar archaeology. Abundances of individual elements measured from some of the oldest stars are used to constrain which type of SNe could be occurring in the early Universe, both by looking at individual stars (Nordlander et al., 2017) and by reviewing samples in a systematic fashion (Fraser et al., 2017, Ishigaki et al., 2018). While the results of these studies remain inconclusive, the determination of accurate stellar abundances of present-day stars is a corner-stone for the study of the earliest stars.

1.3.2 Supernovae and heavy element production

The majority of the chemical elements in the present day Universe are either synthesized by stars during their hydrostatic evolution and ejected into their environment at the end of their lifetime, or form directly within the SN events.

In particular, SNe type Ia are extremely crucial for cosmology and chemical evolution. They are accepted as *standard candles* and used to measure distances to their host galaxies. However, despite their important role, it seems there is still no robust consensus on their progenitor and explosion physics. For example, the fraction of SN Ia events as a result of the star exploding before reaching the Chandrasekhar mass limit – due to the dynamically driven detonation – is still debated. At the same time, the evolutionary path that leads to the explosion of the white dwarf is an outstanding question as well. Deriving the composition of the SN Ia themselves is not straight-forward, as the post-explosion material is optically thick and inhomogeneous. Another way to tell apart possible explosion scenarios is by focusing on the consequences of these long-gone events. All SNe leave a chemical imprint on the surrounding material. By looking at the abundances of the stars formed from that contaminated material and comparing them to the theoretical predictions it is possible to put limitations on the physics of the SN events. Thus, according to Kirby et al. (2019), who studied distributions of stellar abundances in ancient dwarf galaxies, the dominant type of SN Ia is the explosion of a sub-Chandrasekhar mass white dwarf. Eitner et al. (2020) arrive at the same conclusions by looking at the Mn abundances in the Milky Way stars.

Recently, and for the first time, neutron star mergers have been confirmed as a site of heavy element production via the r-process (Abbott et al., 2017, Watson et al., 2019). However, this does not necessarily mean that mergers of two neutron stars are the dominant source of r-process elements. Ji et al. (2019) have shown the interesting possibility to distinguish between neutron star mergers and exotic SNe as source of r-process elements by analysing subtle differences in the relative abundances of lanthanides and actinides.

On the topic of exotic SNe, Ezzeddine et al. (2019) found evidence for the presence of jet-driven SNe at high redshifts by analysing the elemental abundances of the very old star HE 1327-2326. They observed a pronounced overabundance of zinc relative to lower-mass elements. Zinc is believed to form in the inner layer of core-collapse SNe. An overabundance of zinc coming from such a SN must therefore mean that more of the outer layers fall back on the compact remnant than of the inner layers, strongly indicating the jet-driven or a-spherical SNe.

As nucleosynthetic models are advancing, both precise and accurate stellar abundances measurements are required to constrain exactly where and how the heavy elements in our Universe are formed.

1.3.3 Galactic chemical evolution

According to the Λ CMD cosmological model, galaxies form within small dark haloes and their evolution is driven by the mass accretion. In the framework of this theory, massive galaxies – like the Milky Way – are expected to have experienced a lot of mergers which should have left their footprint (Helmi et al., 1999, Bullock & Johnston, 2005). Our own Milky Way galaxy is a rather typical in many aspects (e.g. mass, size, structure) disk galaxy (see e.g. Kormendy et al., 2010, Bland-Hawthorn & Gerhard, 2016) and contains most of the components also identified in the other galaxies, such as disk, bulge, and halo. However, it is thought to have undergone an active history of merger evolution and the impact of these events is still being explored. Fortunately, living inside the Milky Way allows us to study the content of its resolved populations in great detail. The recovery of merger remnants have been done in the spatial (Belokurov et al., 2006) and kinematic (Gilmore et al., 2002) space. However, the merger debris can also be identifiable through their abundance patterns (Freeman & Bland-Hawthorn, 2002, De Silva et al., 2007). For example, Bergemann et al. (2018) found the over-density regions with a chemical composition matching that of the Milky Way disk and concluded that tidal interactions due to the passing by or merging with the dwarf galaxies could affect the dynamics of the Milky Way disk stars. Helmi et al. (2014) were able to distinguish two populations associated as an over-density in the Milky Way disk based on their chemical composition and possibly attribute one of the sub-populations to the merger with the metal-rich cluster. In the era of large scale spectroscopic and kinematic data sets, as e.g. provided by Gaia mission (Gaia Collaboration et al., 2016), a combination of stellar abundances and velocity-coordinates distributions of stars seems to be a prominent tool to study the dynamical and chemical history of the Milky Way and constrain theories of the Galactic formation and evolution.

1.3.4 PRIMORDIAL LITHIUM PROBLEM

Lithium is one of the light elements that is believed to have form in the big bang nucleosynthesis. A small amount of lithium produced in the first minutes of the Universe's lifetime can be predicted with the Big Bang nucleosynthesis theory combined with extremely precise measurements of cosmic microwave background. However, estimates on the amount of primordial lithium are by a factor of 3 to 5 different than the lithium abundances measured in the oldest stars Asplund et al. (2006) or meteorites from the time our Sun was forming. Additionally, the abundances of lithium in old stars were found to be nearly independent of iron abundance (Spite & Spite, 1982, Gao et al., 2020), while most of the heavy elements are transformed in the stellar nucleosynthesis and become more abundant with time. An extensive overview of the problem and possible solutions – whether related to the measurements uncertainties, incomplete models, or even missing physical processes – can be found in Fields (2011). By now the most prominent solution to the mismatch is destruction of Li in stellar interiors once it is pushed into hotter regions with processes such as atomic diffusion, turbulence, and rotation (Arancibia-Silva et al., 2020). For low-mass stars the base of the convective zone is already hot enough to slowly destroy lithium. In this thesis, I also focus on these physical processes, see Chapter 3.

2

Theoretical and practical background of stellar spectroscopic abundances

Stars are sites of extreme physical conditions far from what is directly available to us in the laboratories on Earth. Observations of individual stars and stellar populations allow us to investigate their internal processes and uncover the conditions of their formation and evolution. In the previous chapter, I focused on the importance of stellar chemical composition for the various fields in astronomy. In this chapter, I provide a brief overview of the physics behind stellar radiation and the methods to model it. I introduce the terminology in Sect. 2.1 and discuss commonly used methods to derive stellar parameters in Sect. 2.2. Sect. 2.4 introduces main concepts of modelling stellar radiation. The common assumption of LTE and the framework of NLTE are discussed in Sect. 2.5 followed by an overview of the NLTE effects in Sect. 2.5.2.

Practically everything known about any astrophysical object is known from analysing its emitted radiation. Accurate and reliable theory of radiative transfer in stellar atmospheres has a wide application in the scientific analysis of various astrophysical objects. Modelled spectral energy distribution and continuum radiation can be coupled with observations of colors and magnitudes to test stellar evolution theories. Accurate modelling of spectral lines allows for qualitative and quantitative analysis of stellar chemical composition of both individual stars and stellar populations. The latter also allows to trace the evolution of chemical elements in the stellar interiors from birth to death. Recent developments in the treatment of model atmospheres and NLTE effects allow to infer both accurate and precise abundances. Finally, physical theories and mathematical methods developed for the analysis of stellar atmosphere are often extended to studies of exoplanetary atmospheres or laboratory plasma experiments.

2.1 Definition of a star

In the most simple description, a star is a hydrostatic sphere of radius R containing mass of M. In its centre, nuclear fusion produces heat that stabilizes star against gravitational collapse. The energy is transported outwards and away as stellar radiation. It is know that stars of similar mass and composition follow a similar evolutionary scenario. Thus stellar initial mass and chemical composition are two fundamental properties defining its evolution.

Stellar atmosphere – the most outer layer of a star from which observed radiation is emerging – is usually described with several parameters: effective temperature, surface gravity, luminosity, metallicity, individual abundances and velocities (exact definition depends on the modelling approach).

Effective temperature (T_{eff})

To describe stellar emission with a single parameter it is assumed that a star emits as a black-body, following Planck's law:

$$B(\nu, T_{\text{eff}}) = \frac{2h\nu^3}{c^2} \frac{1}{exp(\frac{h\nu}{k_B T_{\text{eff}}}) - 1}, \tag{2.1}$$

where k_B is the Boltzmann constant, h is the Planck constant, and c is the speed of light. Then effective temperature of a star corresponds to the temperature of the black-body emitting the same amount of energy per surface area. Effective temperature of our Sun is currently set at $5771 \pm 1\,\text{K}$ (Prša et al., 2016).

Surface gravity ($\log g$)

Assuming a simple spherical geometry, the mass and radius of a star are be connected via surface gravity as:

$$g = G\frac{M}{R^2} \tag{2.2}$$

where G is the gravitational constant. Surface gravity of a star is often tabulated relative to that of the Sun as

$$\log g = \log \frac{M}{M_\odot} - \log \frac{R^2}{R_\odot^2} + \log g_\odot \tag{2.3}$$

where $\log g_\odot$ is 4.44 dex (Prša et al., 2016).

Luminosity

An amount of radiant energy a star emits per unit of time is known as luminosity. It is related to the radiative flux at each frequency F_ν and can be connected to the black-body assumption as follows:

$$L = 4\pi R^2 \int_0^\infty F_\nu d\nu = 4\pi R^2 \sigma T_{\text{eff}}, \tag{2.4}$$

where σ is Stefan-Boltzmann constant. Since stellar radii are extremely hard to infer directly (see Sect. 2.2 for details) it is common to link luminosity to effective temperature and surface gravity as

$$\log g = \log \frac{M}{M_\odot} - \log \frac{T_{\text{eff}}^4}{T_{eff\odot}^4} - \log \frac{L}{L_\odot} + \log g_\odot. \tag{2.5}$$

Chemical composition

Stars primarily consist of hydrogen and helium and heavier elements are only present in trace amount. The total chemical makeup is defined as

$$X + Y + Z = 1, \tag{2.6}$$

where X and Y are mass fractions of hydrogen and helium, and Z contributes to the input of all elements other than these two. Although the value of Z is extremely tiny – about 2 % – it is crucial for linking our knowledge about stellar composition to other fields of astronomy like stellar evolution and cosmology.

Abundances of individual elements are usually defined as the ratio of the number of atoms of the chemical element to that of the hydrogen. The latter is accepted to be 10^{12}:

$$A(X) = \log \frac{N_X}{N_H} + 12. \tag{2.7}$$

Most often chemical abundances are provided in the bracket notation relative to the corresponding abundance of that chemical element in our Sun:

$$[X/H] = \log \frac{N_X}{N_H} - \log \frac{N_{Fe\odot}}{N_{H\odot}} \tag{2.8}$$

Metallicity

A bulk composition of all metals in the star, also known as its metallicity, is defined as

$$[M/H] = \log \frac{\sum_i N_{El_i}}{N_H} - \log \frac{\sum_i N_{El_{i,\odot}}}{N_{H,\odot}}, \tag{2.9}$$

with a sum over all chemical elements heavier than lithium. Since it is not at all trivial to derive abundance of each chemical element – or even the most abundant ones – it is commonly accepted to use iron abundance as a tracer of metallicity of a star, thus approximating $[M/H]$ to

$$[Fe/H] = \log \frac{N_{Fe}}{N_H} - \log \frac{N_{Fe\odot}}{N_{H\odot}} \tag{2.10}$$

The choice of iron was dictated by its relatively high abundance in stellar atmospheres and complex atomic structure resulting in thousands of easily observed spectral lines.

2.2 INFERRING STELLAR PARAMETERS

Each star can be described by its two fundamental parameters: mass and initial chemical composition, while the age defines an evolutionary stage of the stellar life cycle. If all three can be determined by independent methods, practically all information about an object becomes available. Some methods to derive parameters of the stars include but are not limited to:

- **Asteroseismology**
  Asteroseismology studies oscillations in stars. Small perturbations to the mechanical equilibrium of a star create waves that travel through the stellar matter. As their path is determined by the speed of sound – which is directly related to the temperature, density and chemical composition – observing these oscillations informs us about the internal structure of the star not observable otherwise. Photometric and spectroscopic observations are used to extract the frequencies, amplitudes and phases of the waves at the stellar surface. The peak oscillations frequency and the separation between the modes of the same degree in the Fourier space are found to be related to the mass and radius of the star (Ulrich, 1986). If an estimate on effective temperature and surface

gravity is available from independent sources, these so-called asteroseismic scaling relations can be used to constrain mass and radius of the star. It is still debated whether the same scaling relations can be applied in the same way to stars of different chemical compositions, initial masses and evolutionary stages (Hekker, 2018).

- **Photometry**
  Photometric techniques are indirect methods commonly used to determine effective temperature and surface gravity of a star. These techniques can provide estimates as precise as few percent. The method can be described in short as follows. Effective temperatures are derived for a sample of stars e.g. an infrared flux method (Casagrande et al., 2014, 2021). Observed magnitudes in various photometric filters are then correlated to the estimates of effective temperature (Casagrande et al., 2010). These correlations can be readily applied to any star given its parameters are not too different from the initial sample. The method depends on the same input models as e.g. spectroscopic analysis, therefore the influence of uncertainties in the opacities and effects of convection and surface inhomogeneities remain to be fully understood.

- **Stellar evolution models**
  Models of stellar evolution predict stellar parameters such as luminosity, radius, effective temperature, and surface gravity based on the initial mass and chemical composition in combination with state-of-the-art physics and model opacities (Eggenberger et al., 2005, Weiss & Schlattl, 2008, Bressan et al., 2012, Costa et al., 2019). Stellar parameters can then be derived by comparing either directly observed and measured values (magnitudes in various filters and their combinations, frequencies of oscillations, etc) or inferred values (effective temperature, surface gravity) to the model predictions. Due to the nature of the models and the precision of the observational data, more often than not the usage of the stellar models to derive, e.g., stellar ages, is limited for unevolved stars like our Sun. The common workaround is to analyse the coexisting stellar populations, e.g. star clusters.

- **Interferometry**
  Interferometric instruments like CHARA[1] and VLTI[2] allow to measure the angular diameter of the star by analysing the pattern of the interference fringes. The angular diameter is usually combined with the estimate on the bolometric flux F_{bol}, which can be obtained either by integrating the observed spectral energy distribution or by

---

[1] `www.chara.gsu.edu`

[2] `www.eso.org/sci/facilities/paranal/telescopes/vlti.html`

connecting photometric magnitudes to the predicted bolometric flux using data-based calibrations. Both values are directly connected to effective temperature T_{eff} as

$$T_{\text{eff}} = (\frac{4F_{bol}}{\sigma\theta^2})^{1/4} \tag{2.11}$$

following from Eq. 2.4. The biggest limitation of the method is its applicability to the brightest closest stars only (Gordon et al., 2019). Such stars, unfortunately, can easily get saturated in the setup of the modern spectroscopic and photometric surveys.

- **Spectroscopy**
  Large spectroscopic surveys like GALAH[3], Gaia-ESO survey[4], LAMOST[5], as well up-coming 4MOST[6] and WEAVE[7] are providing state-of-the-art spectra for millions of stars in our Galaxy and beyond. Strength and shape of different absorption lines visible in each spectrum result from a combination of many factors. Among those are individual abundances of the chemical elements corresponding to the lines, atmospheric structure of a star, presence of magnetic fields, extinction along the line-of-sight. This wealth of involved factors allows to use stellar spectra to infer many of the stellar parameters of interest, among those are effective temperature, surface gravity, metallicity, chemical composition, strength of the magnetic field, and velocities in the atmosphere. Spectra of the same star taken at different time stamps can rule out presence of the stellar companions, planets or show presence of oscillations, as described earlier.

  Spectroscopic data can be combined with various methods to infer the aforementioned stellar parameters. An extensive overview of these methods can be found in e.g. Heiter et al. (2015a). Some studies, e.g. Castelli & Kurucz (2010) even use spectroscopic observations of the brightest stars to measure atomic data, thus reinforcing the status of stars as 'cosmic laboratories'.

  It is worth noting that spectroscopy is the *only* method astronomers can use to detect presence and the relative amount of any chemical element across the periodic table in the stellar matter. Other possibilities include usage of asteroseismic data and stellar models to infer a bulk stellar composition or observations of interstellar medium that is thought to have been enriched by material from exploding stars as described in

---

[3] `https://www.galah-survey.org`

[4] `www.gaia-eso.eu`

[5] `www.lamost.org`

[6] `www.4most.eu/cms/`

[7] `https://ingconfluence.ing.iac.es/confluence/display/WEAV`

Sect. 1.3.2.

Spectroscopic estimates depend strongly on the input line formation data and preferred physical model. Hence, one of the questions this thesis aimed to explore is how commonly accepted modelling assumptions affect the outcome of the spectroscopic analysis.

To take full advantage of the vast amount of observational data, approaches that combine multiple data source, through e.g. the Bayesian formalism (Serenelli et al., 2013, Schönrich & Bergemann, 2014, Gent et al., 2022), are these days becoming a standard choice in stellar astrophysics.

2.2.1 Abundances from stellar spectra

Abundances of individual chemical elements in the stellar matter can only be inferred from the analysis of the spectral lines. There are several methods to perform the model-data comparison in the stellar spectroscopic analysis.

The first method combines measured equivalent widths[8] of the spectral lines, that are proportional to the number of absorbing particles. This approach requires precise integration and adopting special procedures to account for blending as a result of overlapping absorption features from multiple chemical elements. The behaviour of the equivalent widths as a function of the chemical abundance – known as a curve of growth (CoG) – can then be used to infer the abundance of the element. Here the weak spectral lines are most suitable for such analysis due to the linear dependence of the line strength on the number of absorbing particles. Transition from the levels with the different excitation energies form a single CoG. Given that the higher the excitation energy is, the less particles are excited to that state, the CoGs will be shifted. These shift can then be translated to the temperature. Similarly, $\log g$ can be inferred from comparing the CoGs of several ionisation stages. The downside of this method is that lines can show ionisation and excitation imbalance as a results of poor modelling assumptions (Mashonkina et al., 2005, Bergemann, 2011).

The second method is based on the spectrum synthesis and comparing the full observed line profiles with the model predictions. Given the richness of the spectral information, it is common to use a set of additional methods (as described in Sect. 2.2) to first get an independent estimate on T_{eff}, $\log g$, etc. The model line profile is usually either computed on-the-fly during the fitting procedure or interpolated from a pre-computed grid. A spectrum synthesis code is used to create a model spectrum, either full or a small part covering the

---

[8] Width of a rectangular with the surface equal to the integral of the pseudo-normalised absorption feature

line of interest only. The necessary input and the physics of the line synthesis are discussed in Sect. 2.4 and Sect. 2.5.3.

Comparison to the observed spectrum[9] can then be done using various statistical methods, e.g., iterative χ^2-minimisation or Monte Carlo algorithms. The end goal is to find a combination of parameters, including abundances, that provide the best description of the observed spectrum within the selected metric. This method provides an unmatched flexibility and allows to disentangle a variety of absorption-shaping processes, including blending of strong lines as a result of simultaneous contribution from multiple elements, or asymmetric line shapes due to e.g. convection in the stellar material. In this thesis I will only use the line synthesis method and apply it to various observational data.

It is worth noting that here on Earth we do have a way to measure stellar composition – but only that of our own Sun – as well. The most abundant meteorites in the solar system – chondrites – are thought to be the pristine footprints of the time when the solar system was formed. By measuring their chemical make-up in the laboratories on Earth one is able to connect the stellar and terrestrial composition.

2.3 ATOMIC ENERGY STRUCTURE

The most common way to describe how a discrete particle – like an atom – interacts with radiation is through representing its electron energy structure. Any quantum particle – here an electron – can take on discrete amounts of energy corresponding to its *energy state* or *energy levels*. This quality is different from the classical particles which can change their energy by any continuous amount. In this thesis I will use the term energy level – also known as an electron shell or orbit in chemistry – to describe the state of the electrons in atoms, which are bound with the nucleus through the electric field. Similar concept can also be used to describe the rotational or vibrational states of a molecule. Fig. 2.1 illustrates this description applied to a one-electron hydrogen atom. The so-called *ground state* is the zero-point energy state of an atom. It is a stationary state with the lowest energy of the system. Any state corresponding to higher energy is than referred to as an *excited state*. We will label each possible energy state with a principal quantum number $n = 1, 2, 3...$, where the closest to the nucleus state – the ground state – has the principal quantum number $n = 1$ and each further level towards increasing energy gets a sequentially higher n. Each level consists of the subset of states defined by a common quantum number l that determines the

---

[9] Here, I focus on the analysis of the reduced, pseudo-continuum normalised, and wavelength calibrated observed spectra, reflective of most of the data products from the large spectroscopic surveys these days. In individual cases, pre-processing of the observational data might be required for which multiple tools are available (`www.blancocuaresma.com/s/iSpec`, `https://iraf-community.github.io`, `www.astropy.org`).

orbital angular momentum. The value of l ranges from 0 to $n-1$ for that level. It is common to denote the values $l = 0, 1, 2, 3$ with the letters s, p, d, and f. Following this notation, the first excited energy state of the hydrogen atom has a principal quantum number $n = 2$ and consist of two sub-states corresponding to the orbital momentum number $l = 0, 1$ and can be notated as $2s$ and $2p$, respectively. In the central field approximation – where each electron independently exists in a spherically-symmetric field created by the nucleus and other electrons – a many-electron atom is described as a combination of one-electron states.

Electrons with the same principal quantum number n belong to the energy state of that number. Electrons having both the same n and l quantum numbers belong to a sub-state and all electrons in a particular sub-state are called *equivalent.* A *configuration* of N equivalent electrons is written as nl^N, the superscript usually being omitted for $N = 1$. According to the Pauli exclusion principle, two electrons with all four quantum numbers[10] being the same can not existed at the same state. Therefore, the maximum possible number of equivalent electrons is $2(2l + 1)$. A configuration of several sub-states is written as $nl^N n_1 l_1^M$.... Since such abbreviations can get lengthy for multi-electronic atoms, it is common to only denote the configuration of the last few sub-shells that differ from those in the previous element in the periodic table only.

2.4 Radiative transfer in stellar atmospheres

This chapter providing a condensed description of the radiative transfer[11] *in stellar atmospheres is partially based on Rutten (2003), Bergemann & Nordlander (2014), and Hubeny & Mihalas (2014).*

Even the radiation we observe from an unresolved star contains a wealth of information about the structure and composition of its atmosphere. By comparing the physical model of the stellar atmosphere and the radiation penetrating it to the observed spectrum we are able to recover that information.

The specific intensity $I(x, t, n, \nu)$ of the radiation at position x, time t, travelling in direction n, into a solid angle $d\Omega$ having a frequency in the range $(\nu, \nu + d\nu)$ is defined such that the amount of energy passing through a perpendicularly surface element dS in a time interval dt is

$$dE = I(x, t, n, \nu) n\dot{d}Sd\Omega d\nu dt. \tag{2.12}$$

---

[10] n, l, m_j and m_s as the projections of $j = l \pm s$ and $s = \pm\frac{1}{2}$ along a selected direction respectively

[11] The term *radiative transfer* is used to describe a change of radiation travelling through a static material. In case of the time-dependent moving material the term *radiation transport* is used.

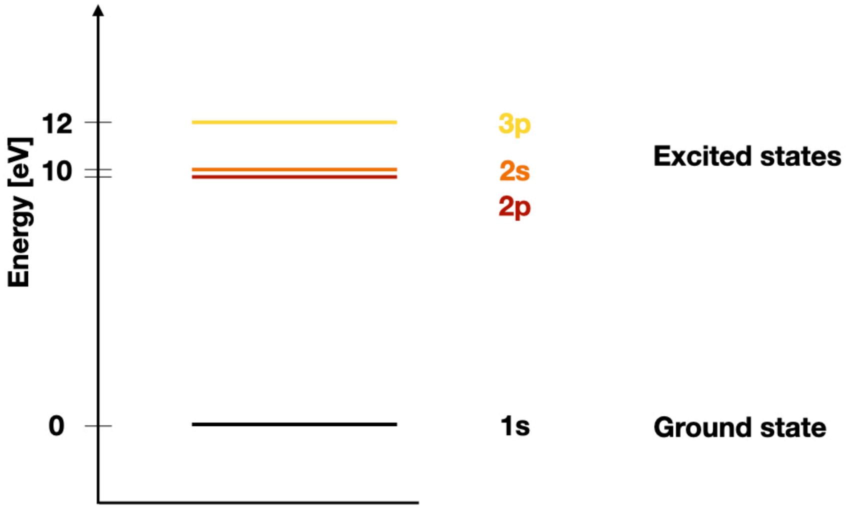

Figure 2.1: Schematic representation of the first four hydrogen atom energy levels. Data was extracted from NIST database (`physics.nist.gov`).

Thus specific intensity is a seven-dimensional distribution function defined on a four-dimensional space-time (x, t) and an independent set of three-dimensional frequencies (n, ν) attached to each space-time (x, t) point. In the most general case spatial- and time-dependent interactions are incredibly hard to model, therefore it is common to adopt some – or all – of the following assumptions:

- one-dimensionality of stellar atmospheres composed either of homogeneous plane-parallel layers or spherical shells where all physical variables are functions of depth only. Thus, the specific intensity is only dependent on one rather than three spatial dimensions
- stationarity resulting in time-independence (assuming mass conservation and no pulsations)
- hydrostatic equilibrium, where radiative pressure is balanced by the gravitational force
- simplified convection descriptions, e.g. mixing length theory
- LTE

Allow me to focus on a one-dimensional (1D) problem here for simplicity. This way, stellar atmosphere is represented by a combination of gas with temperature T, density ρ and some prescription of a velocity field V. The radiation travels outwards towards the surface. As it travels through the stellar atmosphere, the change in the local specific intensity dI_ν is determined by the processes of emission and absorption in the medium. The monochromatic emissivity per volume unit is defined as

$$dE_\nu \equiv j_\nu dV dt d\nu d\Omega, \tag{2.13}$$

where dE_ν is the energy locally added to the radiation in the volume dV per frequency interval $d\nu$ during time interval dt in directions $d\Omega$. The intensity contribution of the emission is

$$dI_\nu(s) = j_\nu(s) ds \tag{2.14}$$

The absorption – also known as extinction – coefficient specifies the amount of energy taken from the beam per path length thus describing the efficiency of the material to absorb or scatter light:

$$dI_\nu = -\alpha_\nu I_\nu ds \tag{2.15}$$

The ratio of the emission and absorption coefficients is known as the source function:

$$S_\nu = j_\nu / \alpha_\nu \tag{2.16}$$

and when multiple processes contribute to the local radiation the total source function is

$$S_\nu^{tot} = \frac{\sum j_\nu}{\sum \alpha_\nu} \tag{2.17}$$

The change of intensity due to emission and absorption as the light travels through matter is then

$$\begin{aligned} dI_\nu(s) &= dI_\nu(s+ds) - dI_\nu(s) = j_\nu(s)ds - \alpha_\nu(s)I_\nu(s)ds \\ \frac{dI_\nu}{ds} &= j_\nu - \alpha_\nu I_\nu \end{aligned} \tag{2.18}$$

The change in the intensity is often described as a function of optical depth τ_ν instead of the geometric path ds. Optical depth is defined as

$$\tau_\nu \equiv \alpha_\nu ds \tag{2.19}$$

Optical depth corresponds to how far we can see into the emitting matter – which is approximately one mean free path. Here, I will use the notation of τ_ν for radial optical depth to describe how the light travels radially outwards perpendicular to the surface of the spherical star. The viewing angle θ between the line of sight and the radial axis of symmetry is defined by $\mu \equiv \cos\theta$. The transfer equation in the plane-parallel geometry then has the following form:

$$\mu \frac{dI_\nu(\tau_\nu, \mu)}{d\tau_\nu} = I_\nu(\tau_\nu, \mu) - S_\nu(\tau_\nu) \tag{2.20}$$

In order to solve the radiative transfer equation (see Eq. 2.20) one has to know the source function S_ν that includes all emission and absorption processes at a given frequency at each point of the stellar atmosphere. The *bound-bound* transitions – those between the lower i and upper j[12] energy levels of a discrete system such as an atom – occur as:

- **spontaneous radiative deexcitation**
  that depends on the transition probability – commonly known as an Einstein coefficient – and corresponds to the so-called "natural" broadening of the energy levels due to the mean lifetimes of the particles
- **radiative excitation and induced radiative deexcitation**
  which, in contrast to spontaneous deexcitation, depend on the transition probabilities as well as the local radiation field
- **collisional excitation and deexcitation**
  which efficiency is proportional to the number density of the colliding particles (e.g. electron or hydrogen atoms) and the velocity distribution

The continuum transitions may occur as a results of either the inelastic *bound-free* or *free-free* processes or the elastic scattering processes. In this work I focus on the NLTE effects in the spectral lines – formed by the bound-bound transitions – only, as NLTE effects on the continuum radiation have so far been shown to be negligible at the optical and infrared wavelength predominantly used in stellar spectroscopy (e.g. Haberreiter et al., 2008).

The line absorption coefficient for a narrow line profiles is then proportional to the *number density* (also known as *energy level population*) n of the upper and lower level of the transition and the statistical weights g of the energy levels:

$$\alpha_\nu \propto n_i(1 - \frac{n_j g_i}{n_i g_j}) \tag{2.21}$$

---

[12] Note that j used as a subscript corresponds to the numbering of the energy levels in the system, while j_ν stands for the emissivity.

and the emissivity (without induced emission) is simply

$$j_\nu \propto n_j \tag{2.22}$$

Assuming that the source function does not vary strongly along the line profiles, the line source function is simply

$$S^l = \frac{2h\nu_0^3}{c}\frac{1}{\frac{g_j n_i}{g_i n_j} - 1} \tag{2.23}$$

As seen from Eq. 2.20 and 2.23, one has to know the number density for each state of the system to solve for the radiative transfer. The assumption of LTE allows to estimate the number densities analytically. LTE is a common assumption for the radiative transfer in stellar atmospheres and beyond, e.g. in the modelling of SN explosions and exoplanetary atmospheres. LTE states that the change of the physical conditions in a small volume of a stellar material is negligible and the thermodynamical equilibrium formulae can be used. The particles in stellar matter (ions, atoms, electrons, molecules, etc) are then considered to be in the equilibrium with each other established through multiple collisions. If a stellar volume is seen as a classical system of distinguishable particles one can deduce the following equilibrium distribution functions:

- **Maxwell distribution** for particle velocities (one dimensional)

  $$f(v) = \sqrt{(\frac{m}{2\pi k_B T})}e^{(\frac{-mv^2}{2k_B T})} \tag{2.24}$$

  where k_B is Boltzmann constant. Thus distribution of particles based on their velocities depends on the mass of the particle and the temperature.

- **Boltzmann distribution** estimates the probability of the particle to be in the state of energy E_i.

  $$\frac{n_i}{n} = \frac{g_i e^{-\frac{E_i}{k_B T}}}{\sum_{j=1}^{M} e^{-\frac{E_j}{k_B T}}} \tag{2.25}$$

  g_i in the Boltzmann distribution is statistical weight of the energy level with energy E_i. n corresponds to the total number density across all M energy states. The denominator is also often referred to as the *partition function.*

- **Saha distribution** describes the degree of ionisation as

  $$\frac{n_{i+1}}{n_i} = \frac{2}{n_e \lambda^3}\frac{g_{i+1}}{g_i}e^{(\frac{-(E_{i+1} - E_i)}{k_B T})} \tag{2.26}$$

where λ is de Broglie wavelength of an electron; n_i and n_{i+1} are number densities of the two successive ionisation stages.

The distributions above simplify the radiative transfer solution significantly. Knowing temperature and electron density at each point of the model atmosphere is enough to estimate the line source function as presented in Eq. 2.23. Under the assumption of LTE the line source function simplifies to the Planck function:

$$S_\nu = B_\nu = \frac{2h\nu^3}{c}\left(\frac{1}{e^{\frac{h\nu}{k_B T}} - 1}\right) \tag{2.27}$$

However, generally LTE **does not hold** in stars. Stellar atmospheres are gaseous low-density environments that do not host enough collisional interactions to thermalise the system. Instead, matter and radiation interact in a number of ways, through processes like photo-ionisation and excitation, recombination, dissociation, etc. Understanding of the importance of these processes for the radiative transfer motivated a development of a new approach called simply NLTE, which stands for Not assuming LTE. In NLTE radiative transfer one has to take into account all possible interactions of the particles and radiation, which inevitably increases the computational complexity.

To account for a number of processing in the interaction between matter and radiation in the framework of the NLTE, equilibrium distribution presented above are replace by the *statistical equilibrium* (SE) that can be written as:

$$n_i \sum_{j\neq i}(C_{ij} + R_{ij}) = n_j \sum_{i\neq j}(C_{ji} + R_{ji}) \tag{2.28}$$

where C_{ij} and R_{ij} are collision and radiation rate per particle for the transitions between the energy state i and the energy state j. By solving the radiative transfer equation simultaneously with the equation for all the processes one ends up with the SE that defined the state of the system in NLTE. The state of the system is described by the atomic number densities n_i. It relates to the LTE number density through what is know as a *departure coefficient*, defined as

$$b_i = \frac{n_{i,NLTE}}{n_{i,LTE}} \tag{2.29}$$

In the assumption of LTE, $b_i = 1$ for each energy level and the levels are said to be 'thermalised'. In the framework of NLTE modelling, departure coefficient $b_i < 1$ refers to that state being underpopulated – hosting less particles than expected in LTE – and $b_i > 1$ refers to the energy level being overpopulated. An example of departure coefficients for a single system is shown on Fig. 2.2.

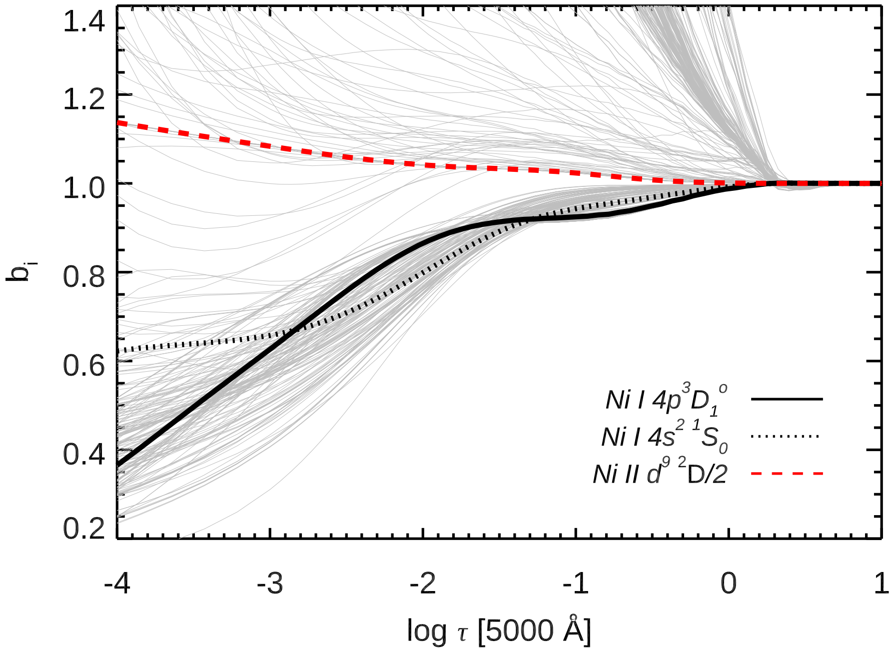

Figure 2.2: Departure coefficients for the energy states of Ni I and the ground state of Ni II as a function of optical depth. Adopted from Bergemann et al. (2021).

In order to produce a model spectrum – which can then be compared to the observed one to infer stellar parameters and abundances – the following ingredients are required:

Model atmosphere

represents the physical structure of the stellar atmosphere in terms of temperature, electron pressure and velocity field. Most often, 1D model atmospheres are used due to their low computational cost. 1D geometry implies that temperature, density and velocities are changing as a function of geometrical (or optical, see Eq. 2.19) depth and horizontal structure (e.g. as a results of convective motions) is omitted. Many computations of 1D atmosphere models are currently available, including Phoenix (Hauschildt et al., 1999), ATLAS (Kurucz, 1979, 2005), MARCS (Gustafsson et al., 2008), and MAFAGS-OS (Grupp, 2004a,b). 1D atmospheric models offer only an approximate description of the stellar atmospheres. Convective and turbulent motions in such models are approximated by some parametrisations (e.g Nordlund et al., 2009, Freytag et al., 2012). Convection is often treated within the so-called mixing-length theory (Böhm-Vitense, 1958) and turbulence is represented using the “macro-”

and "microturbulence" parameters. Here "macroturbulence" refers to the additional broadening of the line profiles applied during the post-processing in order to account for the large-scale movements of the stellar matter. And "microturbulence" is a parameter that is added to the line opacity in a form of the Doppler profile. Despite their simplicity, 1D atmospheric models are still a very popular choice for spectrum synthesis.

Not assuming 1D stratification requires to solve the equations for the conservation of mass, momentum, and energy together with the radiative transfer equation. Such modelling is referred to as three-dimensional (3D) magnetohydrodynamical (MHD) approach and usually simulates a small 3D box representative of the full volume of the star (e.g. Collet et al., 2007, Freytag et al., 2012, Magic et al., 2013a).

Unsurprisingly, 3D MHD simulations provide the most realistic description of the stellar emitting matter. For example, they are shown to explain the excitation and damping of stellar oscillations (e.g. Sonoi et al., 2015, Zhou et al., 2019, 2021), and the dynamo-mechanism of generating stellar magnetic fields (Vögler & Schüssler, 2007). Obviously, such 3D simulations can also be used as a model atmosphere in order to computed predicted stellar radiation (Caffau et al., 2008, 2011, Nordlander et al., 2017, Amarsi et al., 2021). These models do not require any tuning of the parameters, but rather represent convective motions, granulation, center-to-limb variation, etc in a way that agrees extremely well with the observations.

A compromise between the two approaches mentioned above – 1D and 3D – is the usage of the so-called average 3D ($\langle 3D \rangle$) model atmospheres. $\langle 3D \rangle$ model atmospheres are computed by horizontal and temporal averaging of the 3D MHD simulations. That way, convection motions are propagated in form of e.g. microturbulence (Uitenbroek & Criscuoli, 2011), while temperature and density reflect the structure of the original full 3D simulation. The biggest advantage of such models is the computational cost of the spectrum synthesis equivalent to that of a 1D model, therefore $\langle 3D \rangle$ models are commonly used as a proxy of 3D modelling in abundance analysis (e.g. Bergemann et al., 2012b, 2017). The STAGGER collaboration provides $\langle 3D \rangle$ model atmospheres[13] under open access.

Atomic data

is the base for computing a theoretical stellar spectrum. Some of the values required for the line synthesis are: transition probabilities, spectral line broadening data, par-

---

[13] `https://staggergrid.wordpress.com`

tition functions, energy structure (including excitation, ionisation, and dissociation energies), hyper-fine splitting data (if more than one stable isotope of an element is present), etc. These days atomic data is either measured in laboratories on Earth or computed with sophisticated simulations. Multiple databases, e.g. NIST (Kramida, 2008), VALD (Piskunov et al., 1995), provide not only the data, but the quantitative assessment of the corresponding uncertainties as well.

Modelling

Following Eq. 2.32 allows to perform spectrum synthesis at the same cost as within the LTE approach, if departure coefficients – or NLTE populations numbers – are known. This advantage has been used in several spectrum synthesis codes, e.g. SIU (Reetz, 1991, 1999), SME[14] (Piskunov & Valenti, 2017), SYNSPEC (Hubeny et al., 2021), and data products of e.g. GALAH survey (Amarsi et al., 2020b). For discussion of the recent NLTE updates to TurboSpectrum (Gerber et al., 2022), see Sect.2.5.3. The most profound modelling approach these days is solving simultaneously for NLTE and 3D effects. However, due to its high computational cost, it is still not applicable to studies of large stellar populations, in contrast to the analysis of individual stars (e.g. Gallagher et al., 2020, Bergemann et al., 2021, Asplund et al., 2021).

2.5 NLTE THEORY

2.5.1 NLTE RADIATIVE TRANSFER AND LINE SYNTHESIS

Solving the problem of radiative transfer is a much complex task once the assumption of LTE is discarded. As seen from the combination of Eq. 2.20 and Eq. 2.28, radiative transfer must be solved taking into account rates of all radiative and collisional processes, thus coupling non-local radiation field and local properties of the gas. In the framework of NLTE modelling, radiative transfer is solved numerically, for example using a *complete linearisation scheme*, more commonly known as the Newton's method. The following input is required:

Model atmosphere

describing physical properties of the visible radiation forming layer, as already discussed in Sect. 2.4.

Model atom

providing the information about the energy structure of the atom and probabilities

---

[14] `https://pysme-astro.readthedocs.io/en/latest/usage/nlte.html`

of radiative transition and collisions with various particles (electrons, hydrogen and metal atoms, etc), charge transfer processes, photo-ionisation processes, and so on. Compilations of radiative transitions are presented in NIST[15] and VALD databases[16], or by R. Kurucz[17]. Dedicated calculations of the collisional processes are presented in (e.g. Seaton, 1962, Badnell et al., 2005, Barklem, 2018, Belyaev et al., 2016). The combination of the energy structure, radiative and collisional transitions is often referred to as a *model atom*. A common way to schematically demonstrate a wealth of transitions between the energy levels of an atom is with a Grotrian diagram. An example of such diagram is shown on Fig. 2.3.

Background opacities

accounting for the absorption and emission by all other atoms in the photosphere. The data can be provided in terms of transition probabilities which are then used to compute the source function (see Sect. 2.4), or – since such computations are extremely extensive – in form of the precomputed opacity tables that can be interpolated to a given temperature - density profile.

The MULTI 2.3 (Carlsson, 1986) NLTE radiative transfer code was used for all NLTE computations presented in this thesis. Some recent updates to the code – and its sister 3D version of MULTI – were presented in Gallagher et al. (2020). MULTI 2.3 solves the equations of radiative transfer and statistical equilibrium in 1D geometry. It is also worth noting that MULTI 2.3 – as well as many other NLTE codes – works under the assumption of a trace element, meaning that modelled chemical element is thought to have no influence on the stellar structure. Such influence is negligible for most of the chemical elements, with possible exceptions for electron donors or elements contributing strongly to the overall opacity.

Since MULTI 2.3 is able to not only solve for the radiative transfer, but also perform the line synthesis, one is able to compute the so-called NLTE *abundance corrections*. NLTE abundance correction describes the difference in abundance required to match a spectral line of a fixed equivalent width with LTE and NLTE modelling. It thus allows to account for the NLTE effects even if direct NLTE line synthesis is not feasible. NLTE correction (Δ_{NLTE}) depends on the atomic properties of the line, elemental abundance, and physical parameters of a stellar atmosphere and generally can not be analytically predicted. If Δ_{NLTE} is known, the corresponding NLTE abundance of an element $A(X)_{\mathrm{NLTE}}$ is computed according to

---

[15] `https://physics.nist.gov`

[16] `http://vald.astro.uu.se`

[17] `http://kurucz.harvard.edu/linelists.html`

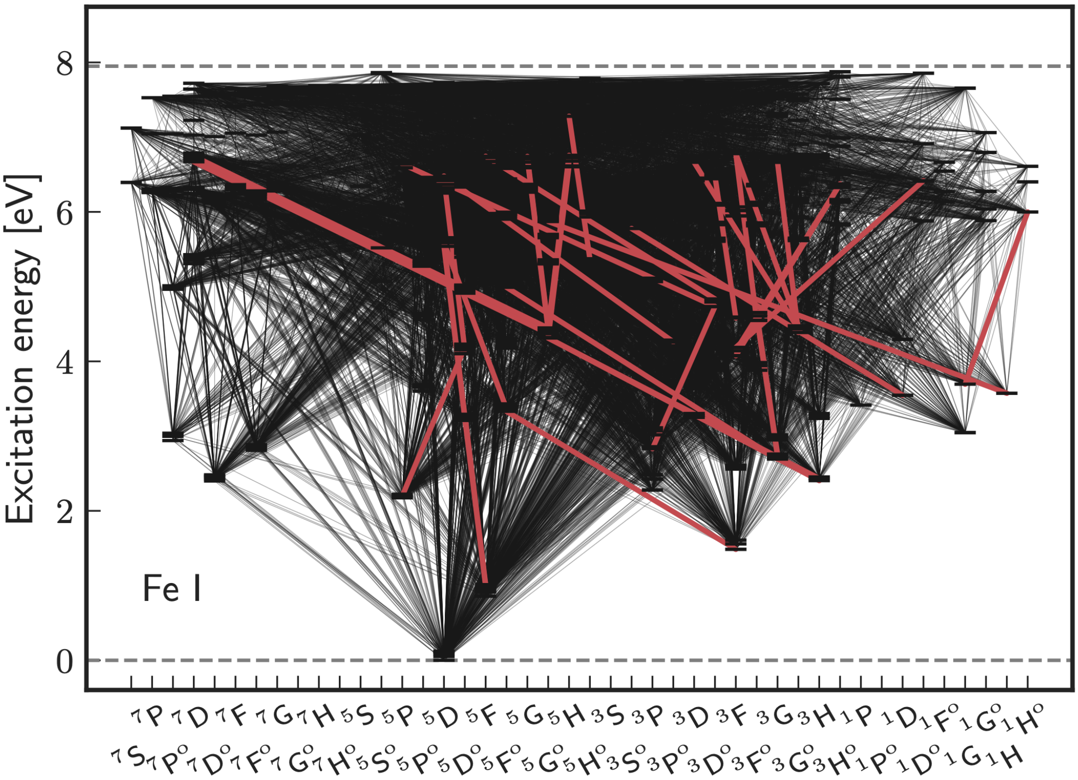

Figure 2.3: Grotrian diagram showcasing the structure of the neutral Fe atom. Horizontal dashes mark predicted energy levels and black lines correspond to the radiative transition. Red lines mark some of the radiative transitions corresponding to the spectral lines used to derived Fe abundance in this work. No bound-free transitions are shown.

Eq. 2.30.

$$A(X)_{\mathrm{NLTE}} = A(X)_{\mathrm{LTE}} + \Delta_{\mathrm{NLTE}}, \tag{2.30}$$

For this work NLTE corrections were computed via the interpolation in the LTE and NLTE CoGs as described in (Eitner et al., 2019).

Alternatively, one can perform NLTE line synthesis using the departure coefficients for each state of the system. Using the definition of the departure coefficient (see Eq. 2.29) and line source function (Eq. 2.23), in the assumption that frequencies of the transition and direction of the emitted light are independent, the NLTE line source function can be expressed as:

$$S^l = \frac{2h\nu^3}{c^2} \frac{1}{\frac{b_i}{b_j}(e^{\frac{h\nu}{k_B T}} - 1)} \tag{2.31}$$

and for the ultra-violet and visual regime, where $h\nu >> k_B T$ it simplifies to

$$S^l \approx \frac{b_j}{b_i} B^l \tag{2.32}$$

thus being connected to the Planck source function (LTE by definition). Intensity within a spectral line, according to Eq. 2.20, can then be computed as

$$I_\nu(\tau_\nu = 0, \mu) = \frac{1}{\mu} \int_0^\infty S_\nu e^{-\tau_\nu \mu} d\tau_\nu \tag{2.33}$$

2.5.2 Influence of NLTE on stellar abundance determination

As shown previously, accepting NLTE modelling affects the strength of the spectral line through its formation depth – lower line opacity corresponds to the deeper formation layers where the temperature is higher, thus resulting in a shallower line – and a counter play of the NLTE populations of the upper and lower energy states. An example of a varying line strength, and therefore derived abundance, is shown on Fig. 2.4.

NLTE modelling is know to resolved *ionisation-imbalance* problem, e.g. as shown in Bergemann (2011). Ionisation-imbalance is a phenomenon where abundances derived from transitions within various ionisation stages – most often neutral and singly ionised species – do not match within the uncertainties. This is seen as a direct results of assuming equilibrium distributions over ionisation stages. For the most recent overview of the NLTE effects on the determination of the abundances the read is directed to Bergemann & Nordlander (2014). Recent overview of the NLTE effects for the chemical elements across the periodic table were presented in e.g. Amarsi et al. (2020b) as well as Asplund et al. (2021) for the

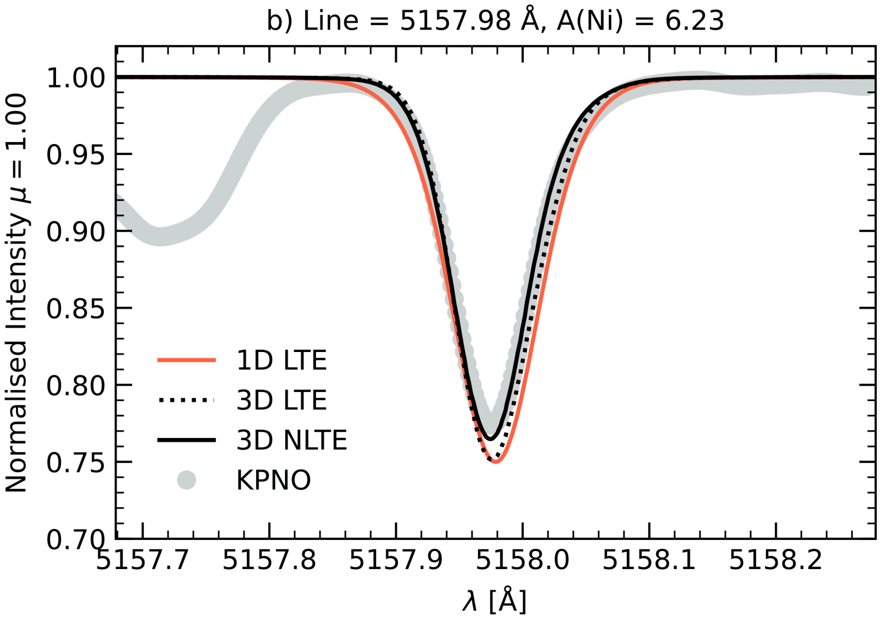

Figure 2.4: Comparison of the model spectral line profiles computing in the assumption of LTE and NLTE. The strongest model line – here 1D NLTE – will correspond to the lowest inferred abundance and vice verse. Adopted from Bergemann et al. (2021).

solar case.

2.5.3 NLTE version of TurboSpectrum

As part of this thesis, I worked on implementing NLTE radiative transfer into one of the most commonly used spectrum synthesis codes: TurboSpectrum (Alvarez & Plez, 1998, Plez, 2012). This work was done primarily in collaboration with Maria Bergemann, Bertrand Plez, Jeffrey Gerber and many other colleagues who helped to test and improve the code. In this Section, I will only focus on my input in terms of NLTE computations, developing high-performance code for computing large-scale model spectra grids and corresponding tests. Presented NLTE version of TurboSpectrum was used to derive the chemical composition of the Sun (see Chapter 4).

As shown in Sect. 2.5, it is possible to compute a model spectrum in a way equivalent to NLTE radiative transfer solution, if NLTE departure coefficients (Eq. 2.29) are known in advance. We thus decided to upgrade line synthesis code TurboSpectrum to include departure coefficients precomputed for each node in the STAGGER⟨3D⟩ and MARCS model atmosphere grid. NLTE computations were done with radiative transfer solver MULTI (Carlsson, 1986). Gerber et al. (2022) contains the comparison of the lines computed with

MULTI and TurboSpectrum and estimates the effects of transferring between the two codes. Futher on, I will refer to a set of the departure coefficients computed for a collection of model atmospheres as a *departure coefficient grid.* I computed such grids for 13 chemical elements: H, O, Na, Mg, Si, Ca, Ti, Mn, Fe, Co, Ni, Sr, and Ba. The list is by no means complete, and will continue expanding. The NLTE model atoms as presented in the following studies were used:

- H: Mashonkina et al. (2008)
- O: Bergemann et al. (2021)
- Na: Larsen et al. (2022)
- Mg: Bergemann et al. (2017)
- Si: Bergemann et al. (2013) with Si+H collisional data from Belyaev et al. (2014) and updates to the radiative data as described in Magg et al. (2022)
- Ca: Mashonkina et al. (2007), updates described in Semenova et al. (2020)
- Ti: Bergemann (2011)
- Mn: Bergemann et al. (2019)
- Fe: Bergemann et al. (2012b), updates described in Semenova et al. (2020)
- Co: Bergemann et al. (2010) adopted with Co+H collisional data from Yakovleva et al. (2020)
- Ni: Bergemann et al. (2021) with Ni+H collisional data from Voronov et al. (2022)
- Sr: Bergemann et al. (2012a) with Sr+H collisional data from Gallagher et al. in prep
- Ba: Gallagher et al. (2020)

NLTE radiative transfer was solved for each point in the MARCS and STAGGER model grids, varying the elemental abundance within $[-2, +1]$ dex in abundance steps of 0.1 dex relative to the corresponding solar abundance (for all elements, except Fe. Fe abundance follows the metallicity of the model atmosphere). Thus, each grid of departure coefficients consists of up-to half a million sets of departure coefficients covering wide range of stellar parameters and abundances. The grids are provided in a format suitable for use with the updated version of the TurboSpectrum. Both the code and all the input data – including the NLTE solutions and model atoms – are made public, see Gerber et al. (2022) for details.

To ease the use of the new version of the TurboSpectrum, I supplemented the release of the NLTE version of TurboSpectrum with a Python wrapper[18], which has the following functionalities:

- linking the original TurboSpectrum workflow with an interactive Python interface
- reading, manipulating and formatting NLTE data
- interpolating in the grid of both model atmospheres and corresponding departure coefficients to allow spectrum synthesis at any point in the (T_{eff}, $log(g)$, [Fe/H], V_{turb}, abundance) space
- multi-core parallelism

Implemented interpolation scheme is drastically different from what was provided with the TurboSpectrum. Interpolation method provided with the TurboSpectrum distribution by default was developed by Thomas Masseron, see Gustafsson et al. (2008), and performs a linear interpolation within a cube of n^2 closest models, where n is a number of coordinates. The latter is also the biggest limitation of the method, as it is not always possible to construct a cube of n^2 models, especially if requested point is located close to the grid boundary, or the grid itself is rather sparse, which is the case for the STAGGER model atmospheres. I therefore introduced an alternative interpolation scheme that finds the closest models based on the Delaunay triangulation and then interpolates linearly between the nodes. Interpolation on the abundance scale is done separately, as it is linearly sampled around the central value and therefore does not require sophisticated methods for finding the neighbours. Comparison of the original and interpolated models is shown on Fig. 2.5. Across a wide range of parameters, internal structure is recovered with 0.3% for temperature and 4% for the electron pressure. It is worth noting that higher sampling of the original models allows to reproduce the structure around $\tau_{500nm} = 0$ with even higher accuracy, however it will inevitable increase computational time.

2.6 SUMMARY

In this Chapter, I focused on the radiative transfer in stellar atmospheres and commonly accepted assumptions to solve for it. It is known that one of such simplifications– the assumption of LTE – biases inferred abundances. As a result, abundances of individual chemical elements can be under- or overestimated and the exact effect depends on the interplay of sophisticated physical processes in the stellar atmospheres. As a result, predicting

---

[18] `github.com/EkaterinaSe/TurboSpectrum-Wrapper`

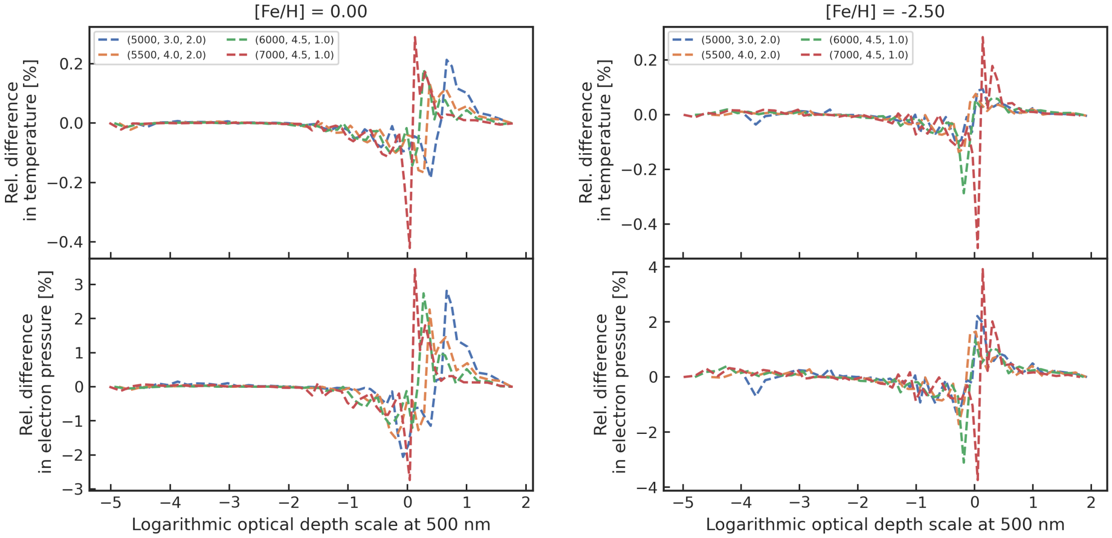

Figure 2.5: Relative difference between the original model atmospheres at (T_{eff}, $log(g)$, V_{mic}) and interpolated temperature and electron pressure values, following the interpolation scheme described in Sect. 2.5.3. Interpolation was performed at the original sampling of the MARCS model atmosphere grid (56 depth points).

such effects analytically – or even just qualitatively – is not always possible. I presented an update to line synthesis code TurboSpectrum in terms of precomputed NLTE solutions for 13 chemical elements across the periodic table. Further in this thesis, I will focus on the applications of NLTE spectroscopic analysis to individual stars and stellar populations.

3

Secular evolution in stellar interiors with NLTE abundances

Disclaimer

This chapter was published as Semenova et al. (2020). The work behind this study was performed in close collaboration with all listed co-authors. The text was written with feedback of collaborators. Section 3.4 and figures therein are work of Morgan Deal.

Models of stellar evolution and their predictions in terms of nucleosynthesis in stars form the basis of many studies in modern astrophysics. Measurements of chemical abundances from stellar spectra provide the most detailed and accurate observational diagnostic of chemical composition of stellar atmospheres, and are, therefore, routinely used in studies of chemical evolution of stellar populations in the Milky Way and other galaxies.

Until recently, it was common to assume that the abundances measured in the atmospheres of late-type (FGK) stars reflected the composition of the material from which the stars were born. Selective modulations of surface abundances of Li, C, and N were known for red giant branch (RGB) stars and were canonically attributed to convective mixing and dredge-up episodes on the RGB (Salaris et al., 2015). Yet for most other evolutionary stages – the main-sequence (MS), turn-off (TO), and sub-giant branch (SGB) – strong evidence for distinct chemical signatures of self-processing in unevolved stars was lacking. This suggested that star clusters are simple mono-metallic stellar populations (e.g. Gratton et al., 2001, Thévenin et al., 2001, Ramírez & Cohen, 2003). These observations could not be reconciled with uncomfortably large effects of atomic diffusion – a term that is nowadays used to refer to a combined action of gravitational settling and radiative acceleration – theoretically predicted in early stellar structure calculations (e.g. Michaud et al., 1984, Turcotte et al., 1998, Richard et al., 2002). As a consequence, it has become common to associate the measured abundance patterns with the variations in the chemical properties of the interstellar matter, disregarding the subtle yet important influence of secular effects in stellar evolution on the surface chemical composition of stars.

However, we are now witnessing a paradigm shift in the field, which is driven both by new observational studies and theoretical results. Empirical evidence of the impact of atomic diffusion on the surface chemical composition of stars is continuously emerging from careful observational studies of Galactic clusters with modern space- and ground-based astronomical facilities (e.g. Korn et al., 2007, Gruyters et al., 2014, Blanco-Cuaresma et al., 2015, Gruyters et al., 2016, Husser et al., 2016, Gao et al., 2018, Bertelli Motta et al., 2018, Souto et al., 2018, Liu et al., 2019, Souto et al., 2019). For example, it is known that the abundances of light elements (Li, Be and B) can be depleted in MS, TO and SGB stars (Smiljanic et al., 2010, Deliyannis et al., 2019, Boesgaard et al., 2020), and these signatures have been linked to the effects of rotation-induced mixing, internal gravity waves, atomic diffusion, and thermohaline mixing. Large statistically significant samples of stars with high-resolution spectra and high-quality astrometry (e.g. the Gaia-ESO survey: Gilmore et al. (2012), Randich et al. (2013); Gaia DR2: Gaia Collaboration et al. (2016, 2018) probing the full evolutionary sequence from the lower MS to upper RGB are now available for many open clusters in the Milky Way. This allows unambiguous membership classification, accurate analysis of evolutionary stages of stars, and in turn, robust identification of systematic abundance variations along the evolutionary sequence of a cluster. One of the major results of the recent detailed investigations is a systematic depletion, of the order ~ 0.15 dex, of the abundances of light (Mg, Ca) and Fe-group elements at the TO of several Galactic open clusters when compared with their lower MS and RGB stars, which is qualitatively consistent with theoretical predictions (Gao et al., 2018, Souto et al., 2018).

Major progress with the implementation of non-standard chemical mixing processes in stellar structure models was made over the past decade. These include micro- and macroscopic mixing processes. Microscopic mixing has a different impact on different chemical elements and it includes gravitational settling, thermal diffusion, and radiative acceleration among other effects. In contrast, macroscopic processes, such as rotational and thermohaline mixing, act on all chemical species in the same way. Earlier theoretical studies of atomic diffusion and mixing in stellar structure calculations (Richard et al., 2002, Deliyannis & Pinsonneault, 1990, Proffitt & Michaud, 1991, Richer et al., 1992, Vauclair, 1999, Chaboyer et al., 2001, Richard, 2005) are now being superseded by the new generation of stellar evolution models (e.g. Théado et al., 2009, Vick et al., 2013, Zhang et al., 2019, Deal et al., 2020) that include both atomic diffusion and transport processes as thermohaline convection, mass loss, rotation or accretion. A comprehensive review of the subject can be found in Salaris & Cassisi (2017).

Despite all the advances, major uncertainties in understanding of the physical mechanisms underlying the transport of elements in stellar interior remain. It has become clear that additional mixing processes, such as parametrised turbulent mixing, are necessary to reconcile observations with stellar evolution models (e.g. Richer et al., 2000, Richard et al., 2001, Michaud et al., 2011). Also observational studies are still limited and provide only a fragmented picture of secular stellar evolution and its relation to abundances in stellar atmospheres. Most studies, to date, focus on the analysis of small stellar samples, comprising not more than a dozen of stars in each evolutionary stage, and do not probe the critical regime of age and metallicity, where the combined effects of secular stellar evolution are expected to be at the maximum. M67 is the best-studied system in this respect, however this cluster is too old, and its turn-off is too cool, to reveal the fine difference in the abundance patterns caused by diffusion processes in the interior (e.g. Deal et al., 2018).

3.1 Introduction

We perform a detailed chemical abundance analysis of 70 stars in the open cluster NGC 2420 (also known as Collinder 154, Melotte 69). This relatively young, $\tau \sim 2$ Gyr (Bossini et al., 2019), cluster was recently observed within the Gaia-ESO large spectroscopic stellar survey (Gilmore et al., 2012, Randich et al., 2013). Accurate proper motions and parallaxes have also become available from the 2nd data release (Gaia DR2) of Gaia space mission (Gaia Collaboration et al., 2016, 2018). The observed sample of stars includes the full evolutionary sequence, from the lower MS to the RGB tip. NGC 2420 is an ideal ensemble to study the effects of atomic diffusion, as it is relatively metal-poor - which maximises the effect of radiative acceleration - and it hosts early F-type stars with $T_{\rm eff} \approx 6500$ K at the TO region. These stars are luminous and have very thin convective envelopes and, as a consequence, the changes in surface composition caused by the combined effects of mixing, gravitational settling, and radiative acceleration, should remain easily detectable, in contrast to cooler G-type solar-like stars, which harbour more massive convective envelopes that efficiently mix the material and act as buffers that wash out the fine signatures of individual transport processes.

3.2 Observations

The Gaia-ESO large spectroscopic survey was designed to obtain high quality spectroscopic observations of 100 000 field stars, as well as members of clusters down to the limiting magnitude $\mathrm{V} = 19^{\mathrm{m}}$. For further overview the reader is referred to Gilmore et al. (2012), Randich et al. (2013). In this work we make use of spectroscopic data obtained in high resolution (HR) mode with the GIRAFFE multi target spectrograph mounted at the Very Large Telescope (VLT)[1]. Although some targets in the cluster were also observed with the higher resolution UVES spectrograph, the spectra are only available for a few stars on the red giant branch. The pre-selection of targets in this cluster was based on the colour-magnitude diagram (CMD) from earlier photometric studies (Anthony-Twarog et al., 2006, Sharma et al., 2006). Post-processing of raw observed spectra was done by the Gaia-ESO dedicated work groups. We use the spectra released within the 5th internal Data Release (iDR5), which contains 545 objects labelled as cluster candidates. The signal-to-noise ratio (SNR) ratio of the spectra ranges from 10 to 150, and for our final sample the median SNR is 70.

3.3 Methods

3.3.1 Target selection

The recent Gaia DR2 estimate of the cluster parallax, $\pi = 0.363 \pm 0.064$ milli-arcsec (mas), yields the distance of 2.55 kpc with an uncertainty of about 0.5 kpc (Cantat-Gaudin et al., 2018). Owing to the large distance, we refrain from membership analysis based on the proper motions of the stars and instead select cluster members by their apparent positions and radial velocities. We require the radial velocity to be within the range of $73 - 77\,\mathrm{km/s}$ and angular distance from the cluster center to be less then 10 arcmin, according to the observable size of the cluster as reported in Sharma et al. (2006). This procedure effectively eliminates 214 foreground and background stars and yields 331 cluster candidate members. We note that adding the proper motions in the analysis does not change our classification,

---

[1] `www.eso.org/sci/facilities/paranal/instruments/flames/inst/Giraffe`

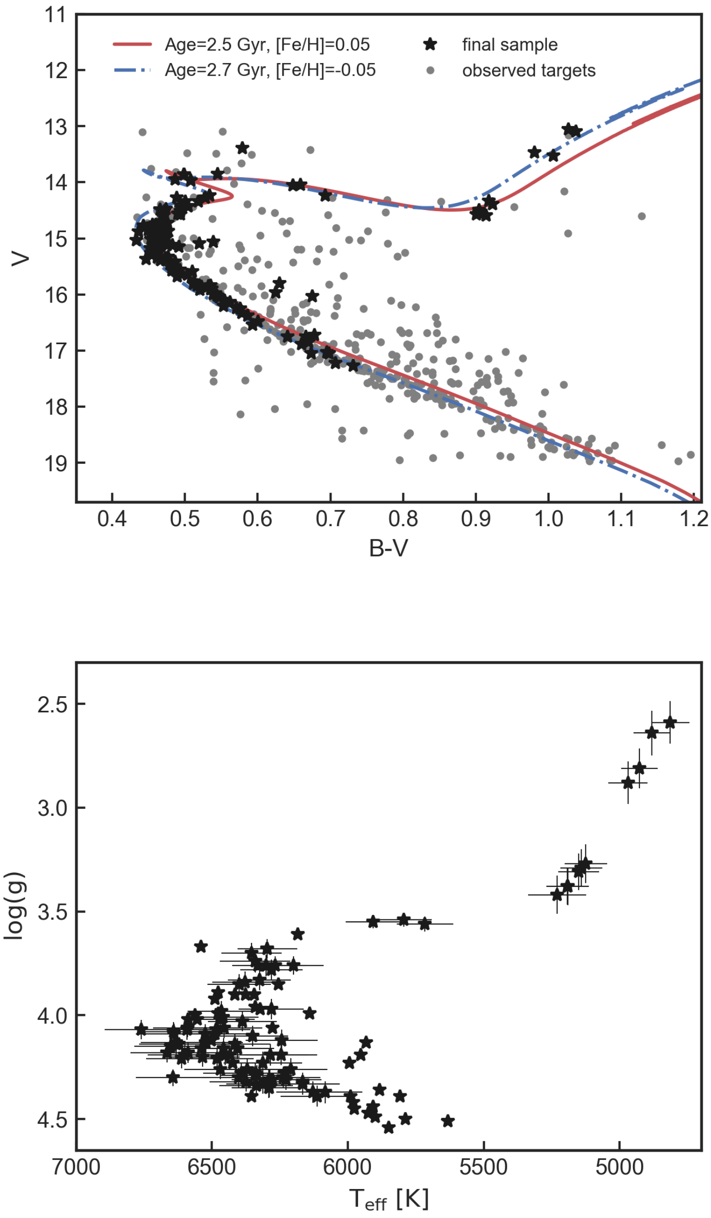

Figure 3.1: Top: B-V colours of the observed stars in the open cluster NGC 2420 plotted as a function of their V magnitude. The best-fit GARSTEC isochrones are over-plotted (see text). Stars comprising the final sample are depicted with black asterisks. For selection criteria see main text. Some of the stars in the kinematically selected sample could be binaries. Bottom: Hertzsprung–Russell diagram of stars for which we perform detailed spectroscopic analysis.

as the uncertainties of proper motions are large. We explicitly avoid pre-selection on metallicity, as stellar structure models computed with atomic diffusion and mixing predict a dispersion in the chemical composition of the cluster, hence any pre-selection on the chemical composition carries a major danger to erase these astrophysically important signatures that are in the focus of our work.

Gaia photometry of the cluster reveals a characteristic broadening of the cluster MS. One of the viable explanations for this feature is the presence of unresolved binaries in our sample. It is a well-established fact (e.g. Maeder, 1974, Bragaglia & Tosi, 2006, Cordoni et al., 2018, El-Badry et al., 2018, Price-Whelan et al., 2020) that the unresolved binaries composed of two MS stars are redder and brighter than single MS stars of a similar mass. These unresolved binary systems may appear up to ~ 0.75 mag brighter than the canonical main sequence that characterises evolution of single stars. However, it is not only the visual brightness, but also the color as a proxy for $T_{\rm eff}$ that is affected (El-Badry et al., 2018). The effects become significant for binaries in which both components have similar masses (El-Badry et al., 2018). According to the statistical method by Cordoni et al. (2018), NGC 2420 has a significant, 33 %, fraction of unresolved MS-MS binaries. Binaries with mass ratio $q > 0.7$ constitute 10 % of NGC 2420 members. We, therefore, exclude those stars that have a high likelihood, based on the CMD position, of being binaries from the subsequent analysis.

3.3.2 Age of the cluster

We estimate the age of the cluster by fitting the observed Johnsons-Cousin photometry (Sharma et al., 2006) and Gaia parallaxes[2] to a grid of stellar isochrones, as described below. The cluster is almost unaffected by reddening. According to the NASA/IPAC Infrared Science Archive service[3], E(B-V) = 0.035 mag, in agreement with earlier studies (Anthony-Twarog et al., 2006). NGC 2420 has been considered to be a moderately metal-deficient open cluster, being a ”transition” object between the solar metallicity open clusters and more metal-poor globular clusters. Some of the recent studies targeting members of NGC 2420 report the average metallicity of the cluster to be at $[\mathrm{Fe/H}] = -0.05 \pm 0.10$ (Pancino et al., 2010, , based on a few stars observed at high-resolution) or $[\mathrm{Fe/H}] = -0.2 \pm 0.06$ (Jacobson et al., 2011, based on stars observed with a medium-resolution spectrograph). (Siegel et al., 2019) suggest that isochrones with lower than previously found metallicity, by -0.1 dex, are needed to describe the photometry of the cluster turn-off stars.

---

[2] We access the parallaxes available in the Gaia DR2 using the ASTROPY community Python library

[3] `irsa.ipac.caltech.edu/applications/DUST/`

We use the grid of GARSTEC stellar isochrones (Weiss & Schlattl, 2008) which are based on the same stellar models as used in BeSPP (Serenelli et al., 2017). Synthetic photometry is computed using bolometric corrections based on ATLAS12/SYNTHE (Kurucz, 1970, 1993) as implemented by Conroy et al.[4]. Zero point corrections were applied to reproduce the solar colors from Casagrande & VandenBerg (2018).

To break the age-metallicity degeneracy we assume the metallicity of the cluster to be the one of the most evolved stars in our sample, which are located on the RGB. Metallicity of those stars was computed with spectrum synthesis, see Sect. 3.3.3 for more details. Figure 3.1 shows two GARSTEC isochrones, which correspond to the age of 2.5 and 2.7 Gyr, respectively. We caution that the standard procedure of fitting the grid of isochrones to the CMD, although wide-spread in astronomy see i.e. Pont & Eyer (2004), assumes that the cluster is a mono-metallic coeval system. In fact, this contradicts our findings (Sect. 3.5) of a systematic depletion of elemental abundances at the cluster TO point, which we interpret as a signature of atomic diffusion and mixing. However, employing a different, more strict, approach is not feasible at this stage. Indeed, a systematic depletion of metallicity in principle requires an iterative procedure involving the full analysis of the observed spectra and Bayesian stellar evolution fitting. Developing such a model is beyond the scope of our study. However, in the next section we show that fundamental stellar parameters are not affected at any significant level by the assumed «average» metallicity of the cluster.

3.3.3 Stellar parameters and chemical abundances

We use several methods to constrain stellar parameters: analysis of photometry and parallaxes, fitting of the Balmer lines, and the full Bayesian approach employing stellar evolution models and parallaxes. All these methods are broadly used in the literature and have been verified in our previous studies with different families of synthetic spectral models (Bergemann et al., 2012b, Ruchti et al., 2013, Serenelli et al., 2013). We follow this approach, rather than using the recommended Gaia-ESO parameters and abundances, because this allows an objective analysis of systematic and statistical uncertainties, which are associated with every step in stellar parameter determinations.

Photometric $T_{\rm eff}$ are derived from the $(V-K)$ colour using the Alonso et al. (1996) and Casagrande et al. (2010) calibration relations. We assume the same metallicity, [Fe/H] $= -0.2$, for all cluster members, but check that the variation of metallicity has no significant impact on the $T_{\rm eff}$ estimates. These estimates of $T_{\rm eff}$ are then employed as initial guesses

---

[4] `http://waps.cfa.harvard.edu/MIST/model_grids.html#bolometric`

for the spectroscopic analysis of H_α line wings (see Ruchti et al. (2013) for the details of this method).

We use the SME 1D LTE code (Piskunov & Valenti, 2017) and MARCS model atmospheres (Gustafsson et al., 2008) to generate synthetic model spectra and fit them to the observed spectra. Finally, we resort to the Bayesian code BeSPP (Serenelli et al., 2013) to refine our photometric and spectroscopic estimates of $T_{\rm eff}$, and to derive estimates of $\log g$ for our targets. Assuming the Gaussian uncertainty of ±150 K on the spectroscopic values, we combine them with the 2MASS JHK magnitudes, Gaia parallaxes, and adopt a uniform metallicity prior ($[\mathrm{Fe/H}] = -0.20 \pm 0.30$). The final estimates of $T_{\rm eff}$ and $\log g$ are determined from the analysis of the full posterior probability distribution functions (PDFs) as described in Serenelli et al. (2013). We note that the final estimates are not affected in any significant way by assuming a uniform metallicity for the cluster, see Fig. 3.2

The analysis of metallicities and chemical abundances for individual stars is strictly spectroscopic, and we rely on the method of detailed spectrum synthesis. Although the GIRAFFE HR10 and HR15N spectra cover only a limited wavelength range, we have 15 Fe I and 2 Fe II relatively unblended spectrum features, as well as a few clean features of other chemical elements that are suitable for a high-quality abundance analysis. The parameters of these lines are provided in Table 3.1.

All atomic data are adopted from the official Gaia-ESO line list (see Heiter et al., 2015b, for details). We note that some species (Mg and Li) are represented by one spectral feature in our observed spectral data. We have, therefore, taken a special care to assess all sources of error in the abundance analysis of the diagnostic features, including statistical and systematic uncertainties. The assumption of 1D LTE is arguably the most severe source of systematic error in abundance estimates(e.g. Asplund, 2005, Bergemann & Nordlander, 2014). More than that, 3D and NLTE effects are function of the evolutionary stage. We therefore perform detailed calculations of NLTE abundances using canonical 1D hydrostatic model atmospheres and 3D hydrodynamic model atmospheres. The detailed approach to NLTE computations is described in the following sections.

1D NLTE ABUNDANCES

We used the 1D statistical equilibrium code MULTI2.3 (Carlsson, 1986) to compute grids of NLTE abundance corrections, $\Delta_{\rm NLTE}$, via interpolation in the LTE and NLTE curves-of-growth as described in Sect. 2.5.1. The NLTE correction $\Delta_{\rm NLTE}$ is positive when the NLTE line profile is weaker than its LTE equivalent. Vice versa, $\Delta_{\rm NLTE} < 0$ implies that the NLTE line profile is stronger than its LTE counterpart, given all other parameters in

Table 3.1: Main properties of spectral features used to compute stellar abundances with SME.

Element	Ion	λ, Å	log (gf)	E_{low}, eV	E_{up}, eV
Fe	1	5339.929	−0.667	3.266	5.587
Fe	1	5364.871	0.228	4.446	6.756
Fe	1	5373.709	−0.760	4.473	6.780
Fe	1	5379.574	−1.514	3.695	5.999
Fe	1	5389.479	−0.410	4.415	6.715
Fe	1	5393.167	−0.715	3.241	5.539
Fe	1	5398.279	−0.630	4.446	6.742
Fe	1	5434.524	−2.121	1.011	3.292
Fe	1	5445.042	−0.020	4.387	6.663
Fe	1	5506.779	−2.795	0.990	3.241
Fe	1	5560.212	−1.090	4.435	6.664
Fe	1	5587.574	−1.750	4.143	6.361
Fe	1	6494.980	−1.268	2.404	4.313
Fe	1	6593.870	−2.420	2.433	4.313
Fe	1	6710.318	−4.764	1.485	3.332
Fe	2	5425.249	−3.220	3.199	5.484
Fe	2	6516.077	−3.310	2.891	4.793
Ca	1	5349.465	−0.310	2.709	5.026
Ca	1	5512.980	−0.464	2.933	5.181
Ca	1	5581.965	−0.555	2.523	4.744
Ca	1	5588.749	0.358	2.526	4.744
Ca	1	5590.114	−0.571	2.521	4.739
Ca	1	5594.462	0.097	2.523	4.739
Ca	1	5601.277	−0.523	2.526	4.739
Ca	1	5602.842	−0.564	2.523	0.000
Ca	1	6471.662	−0.686	2.526	4.441
Ca	1	6499.650	−0.818	2.523	4.430
Mg	1	5528.405	−0.498	4.346	6.588
Li	1	6707.764	−0.002	0.000	1.848
Li	1	6707.915	−0.303	0.000	1.848
Li	1	6707.922	−1.122	0.000	0.000
Li	1	6708.073	−1.423	0.000	0.000

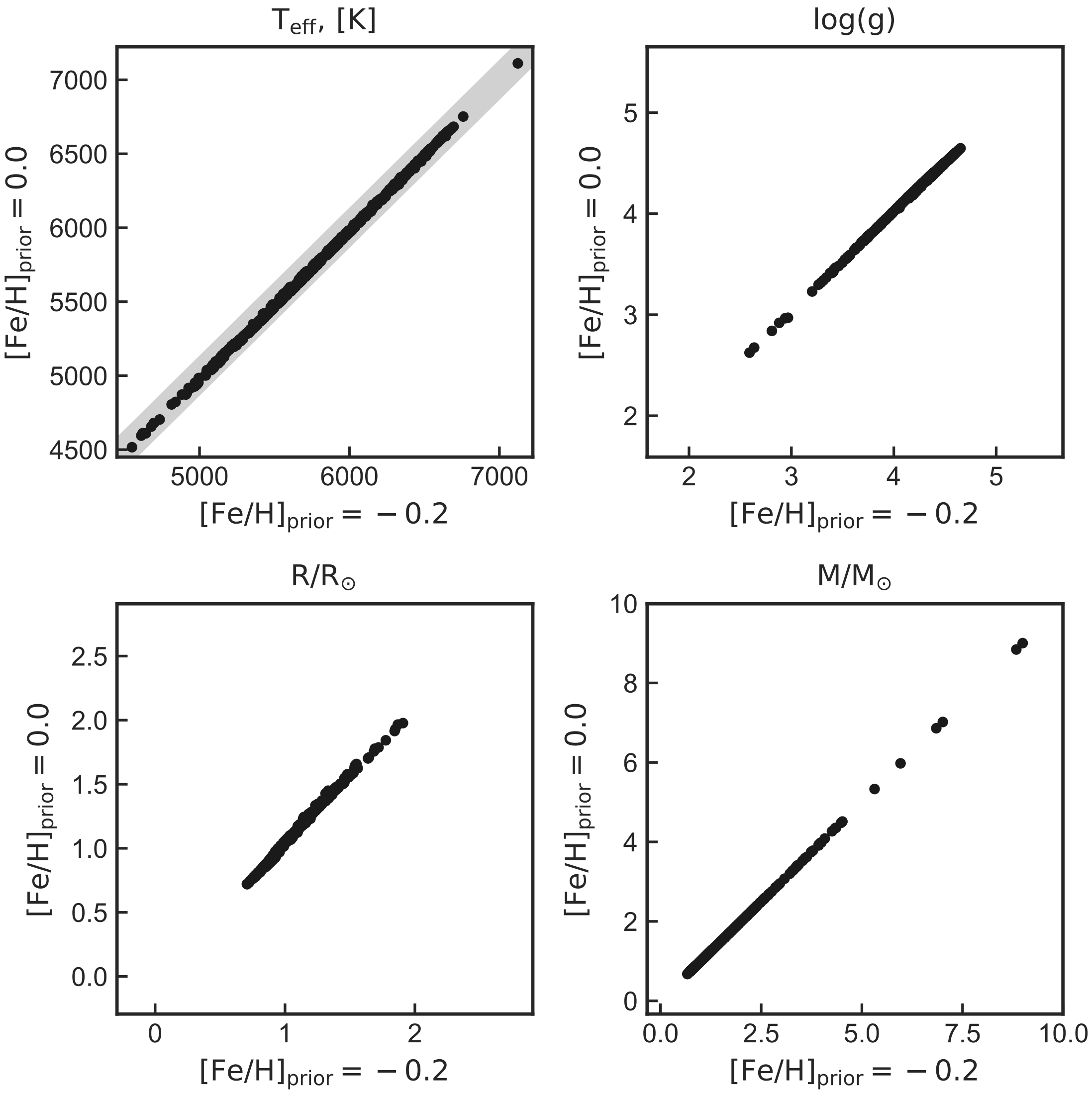

Figure 3.2: Comparison of $T_{\rm eff}$, $\log{\rm (g)}$, masses and radii derived from the Bayesian analysis as described in Serenelli et al. (2013) assuming a uniform metallicity of a cluster [Fe/H] = 0 or [Fe/H] = -0.2. Shaded ares depict the range of mean errors on derived parameters, $\sigma(T_{\rm eff}) = 120\,{\rm K}$, $\sigma(\log g) = 0.05\,{\rm dex}$, $\sigma({\rm R/R_\odot}) = 0.1$, $\sigma({\rm M/M_\odot}) = 0.05$ respectively. Thus we show that the derived fundamental parameters are not biased by the initial guess of the metallicity.

calculations (abundance, model atmosphere parameters) are identical. In the latter case, the LTE abundance is higher compared to NLTE abundance. It should be stressed, however, that Fe is the only element for which $\Delta_{\rm NLTE}$ is strictly differential: the input parameters of the model atmosphere in LTE and NLTE calculations are the same. The NLTE abundance corrections for the other chemical elements - Mg, Ca, and Li - are computed using NLTE-corrected metallicities, which implies, for a given T_{eff}, $\log g$, and ξ_{t}, so this implies that we correctly take into account the second-order dependence of their NLTE correction on that of Fe. The NLTE corrections on iron lines typically amount to +0.03 to +0.07 dex, which implies the sensitivity of the NLTE corrections for Mg and Ca is of the order 0.01 dex.

Background opacity tables for each of these elements were computed using the Turbospectrum radiative transfer code (Plez, 2012). In 1D calculations we use MARCS model atmospheres. Statistical equilibrium computations are performed under the trace element assumption for 135 model atmospheres within a broad range of stellar parameters: $T_{\mathrm{eff}} = [4500, 7000]\,\mathrm{K}$, $\log g = [2.5, 4.5]$, $[\mathrm{Fe/H}] = [-0.75, 0.25]$. Microturbulence parameter is ranging within $1 - 1.2\,\mathrm{km/s}$. The atomic models for Mg and Ca, and are based on the models presented in the earlier studies by (Bergemann et al., 2017, 2012b, Mashonkina et al., 2017). Table 3.2 summarises the main properties of the atomic models, such as the number of energy levels and ionisation stages, the number of bound-bound, and the size of the frequency grid for radiative bound-free transitions. In this work, we update the reaction rates and cross-sections to more recent estimates available in the literature. In particular, we include the new photo-ionisation cross-sections for Fe I from Bautista et al. (2017), replace the semi-classical recipes for the rates of bound-bound and bound-free transitions cased by inelastic collisions between Fe+H (Barklem, 2018) and Fe+e (Bautista et al., 2017). In the Ca model atom we update rates for transitions caused by inelastic Ca+H collisions (Belyaev et al., 2017) and update the list of energy levels to include fine structure resolved levels and therefore, update radiative bound-bound transitions. The estimates of line broadening caused by elastic collisions with H atoms are taken from Barklem et al. (2000). We also reduce the complexity of the atomic models, in order to use them in the 3D NLTE calculations (Sect. 3.3.3). We cut the Mg photo-ionisation cross-sections at 1100 Å as radiative fluxes at bluer wavelengths is negligibly small. For Fe, we re-sample the photo-ionisation cross-sections, so that they consist of a factor of ~ 10 less frequency points, but still contain all the important resonances. Numerous tests have been carried out to ensure that the atomic models with reduced complexity do not introduce any biases in 1D and 3D NLTE abundance corrections with respect to the original models. For Li we make use of 1D NLTE corrections published by Lind et al. (2009).

Our 1D NLTE abundance corrections are shown in Fig. 3.3. The NLTE corrections for the optical Fe I lines are moderate and do not exceed 0.15 dex, supporting previous estimates in the literature (Bergemann et al., 2012b, Ezzeddine et al., 2018). For the Mg I 5528 Å line, the NLTE correction is small: it varies from 0.03 dex for the TO model to < 0.01 for the main-sequence and sub-giant models. Ca I lines are typically weaker in NLTE

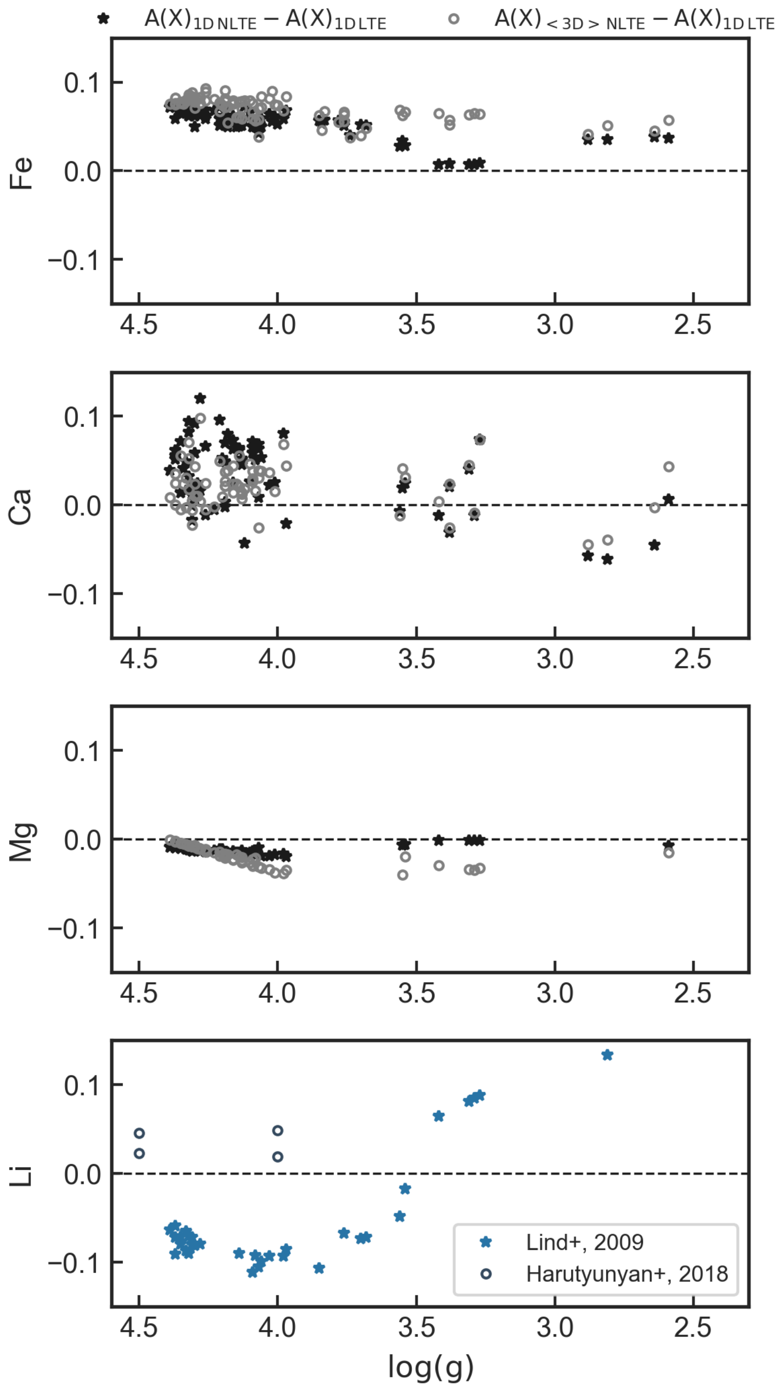

Figure 3.3: Difference in abundances of investigated elements if derived in 1D NLTE and 3D NLTE vs 1D LTE approach for the final sample of stars. Depicted difference is defined as $\Delta_M = A(X)_M - A(X)_{1D\,LTE}$, where M is 3D NLTE or 1D NLTE case.

Table 3.2: Main properties of atomic models used in statistical equilibrium and NLTE abundance calculations.

Element	# Energy levels			# Radiative transitions		# Frequency points	
Fe	548 Fe I	58 Fe II	1 Fe III	12 635 b-b	606 b-f	89 537 b-b	64 455 b-f
Ca	67 Ca I	37 Ca II	1 Ca III	624 b-b	104 b-f	7 520 b-b	10 433 b-f
Mg	85 Mg I	1 Mg II	X Mg III	246 b-b	85 b-f	2 940 b-b	20 242 b-f

compared to LTE, therefore, the NLTE corrections are moderately positive and range from 0.05 dex on the main-sequence to -0.1 dex on the subgiant branch. NLTE corrections to Li I 6707 line is negative for main-sequence models, but it becomes positive on the RGB. We emphasize that in virtue of the metallicity-dependence of the NLTE abundance corrections for every element other than iron, our estimates of NLTE effects for the NGC 2420 stars may not be directly comparable with other studies.

3D NLTE ABUNDANCES

As a proxy of 3D structure of stellar atmospheres, we use averaged 3D atmospheric models taken from the STAGGER grid of stellar convection simulations (Magic et al., 2013b). The procedure to compute the 3D NLTE corrections is identical to that used for 1D NLTE calculations (3.3.3) and it follows our approach in Bergemann et al. (2012b). To account for 3D convective motions we include turbulent velocity in otherwise 1D model atmosphere according to Eq.3.1 as proposed by Uitenbroek & Criscuoli (2011).

$$V_{\mathrm{turb}} = \frac{1}{3}\sqrt{< v^2 > -(< v_x >^2 + < v_y >^2 + < v_z >^2)} \tag{3.1}$$

We emphasize that the 3D models do not include any parametrisations of convection, and so there are no ad-hoc parameters, such as the mixing length or micro- and macro-turbulence, which allows us to perform radiation transfer from the first principles.

The estimates of Δ_{3DNLTE} for Fe, Ca, and Mg are shown in Fig. 3.3. Our results for 3D NLTE corrections compare favourably well with the earlier estimates in the literature. For Ca this is the first study of 3D NLTE effects for the stars other than the Sun. For Fe and Mg, the 3D NLTE corrections are within 0.05 dex, which is consistent with the calculations by Bergemann et al. (2012b) and Bergemann et al. (2017), respectively.

Our results for Ca in 1D NLTE are consistent with (Mashonkina et al., 2017), who predict modest and positive NLTE abundance corrections. The 3D effects, however, are insignificant. For Li we estimate 3D NLTE corrections based on the precomputed grid by (Harutyunyan et al., 2018). At [Fe/H] = -0.5 they predict 3D NLTE correction to be between 0.019 – 0.049 for MS and TO stars. We note that this value is much smaller than our observational errors (~ 0.1 dex) and 1D NLTE effects (~ -0.15 to 0.15 dex).

The 3D NLTE corrections are applied to abundances measured in 1D LTE to derive the final chemical abundance pattern of NGC 2420.

Uncertainty estimates

For all measured chemical elements we propagate corresponding abundance uncertainties using a Monte-Carlo approach. We construct a set of randomly sampled input parameters with respect to their errors and perform the spectrum fitting procedure with these input parameters fixed. The resulting error on derived abundances is defined as the standard deviation of the set of solution assuming a Gaussian distribution. Therefore, the errors presented account for fluctuations of the solutions due to noise component (signal-to-noise ratio of observed spectra) and systematic component (i.e. normalization procedure, errors of fundamental parameters).

3.4 Stellar evolution models with atomic diffusion and mixing

3.4.1 Stellar structure code

The primary goal of this paper is to study radial transport of chemical elements in stellar interiors. This physical phenomenon is caused by the competition and coupling between atomic diffusion and macroscopic transport processes. Atomic diffusion represents a balance between gravitational settling and radiative levitation forces (Meynet et al., 2004). The underlying mechanism is well-understood and the accuracy, with which it can be modelled in stellar structure, is roughly 20%, being limited by approximations in the atomic diffusion formalism and cross-sections (see Michaud et al., 2015, for a detailed overview). Other macroscopic transport processes of diffusive (e.g. rotation, thermohaline convection) or advective (e.g. mass loss) nature, are not yet well-constrained and, therefore, their effects are usually modelled using simple parametric recipes (e.g. Richer et al., 2000, Richard et al., 2001, Michaud et al., 2011). These processes can mitigate the effects of atomic diffusion on surface abundances.

We use the CESTAM code (Code d'Evolution Stellaire Adaptatif et Modulaire, the ”T” stands for transport) (Morel & Lebreton, 2008, Marques et al., 2013, Deal et al., 2018) to compute stellar evolutionary tracks including atomic diffusion and additional parametrised mixing to provide quantitative predictions for the behaviour of the surface chemical composition for different evolutionary phases of a star. The code adopts the OPAL2005 equation of state (Rogers & Nayfonov, 2002) and the OP opacity tables (Seaton, 2005). These are complemented by the Wichita opacity data at low temperatures (Ferguson et al., 2005). We use opacity tables for a fixed solar mixture. We have verified that the error related to this assumption (not recomputing the Rosseland mean opacity taking into account mixture variations due to atomic diffusion) is never larger than 0.01 dex. This is due to the variations of chemical element abundances being relatively small, as they are inhibited by an additional transport process in our models.

Nuclear reaction rates are adopted from the NACRE compilation (Angulo, 1999), except for the $^{14}\mathrm{N}(p,\gamma)^{15}\mathrm{O}$ reaction, which is taken from the Laboratory for Underground Nuclear Astrophysics (LUNA) compilation (Imbriani et al., 2004). We use the Canuto-Goldman-Mazzitelli formalism for convection (Canuto et al., 1996) with the mixing-length parameter $\alpha_{CGM} = 0.68$ calibrated on the Sun. The models also include the core overshoot of 0.15 H_P. The stellar atmosphere, which represents the outer boundary condition in stellar structure models, is computed in the grey approximation. Following the recommendation of Serenelli (2010) we adopt the AGSS09 (Asplund et al., 2009) mixture for the refractory elements. The initial hydrogen, helium, and metal mass fractions - X_0, Y_0 and Z_0 respectively - are determined from the solar calibration, following the $\Delta\mathrm{Y}/\Delta\mathrm{Z}$ slope of 0.9 as determined in Deal et al. (2018). We do not take mass loss or magnetic fields into account. The evolution is computed from the pre-main-sequence up to the age of 2.5 Gyr.

3.4.2 MODELLING TRANSPORT PROCESSES

The diffusion equation of a trace element i at a given depth is expressed as following:

$$\rho\frac{\partial X_i}{\partial t} = \frac{1}{r^2}\frac{\partial}{\partial r}\left[r^2\rho D_\mathrm{turb}\frac{\partial X_i}{\partial r}\right] - \frac{1}{r^2}\frac{\partial}{\partial r}[r^2\rho v_i] + A_i m_p\left[\sum_j (r_{ji} - r_{ij})\right], \tag{3.2}$$

where X_i is the mass fraction of element i; A_i its atomic mass; m_p the mass of a proton; ρ the density in the considered layer; D_turb the turbulent diffusion coefficient; and r_{ij} the rate of the reaction that transforms the element i into j. The competition between macroscopic transport processes and atomic diffusion is given by the first two terms in the right-hand side of Eq. 3.2. The atomic diffusion velocity v_i can be expressed as

$$v_i = D_{ip}\left[-\frac{\partial \ln X_i}{\partial r} + \frac{A_i m_p}{kT}(g_{rad,i} - g) + \frac{(\bar{Z}_i + 1)m_p g}{2kT} + \kappa_T\frac{\partial \ln T}{\partial r}\right], \tag{3.3}$$

where D_{ip} is the diffusion coefficient of element i relative to protons; $g_{rad,i}$ the radiative acceleration on element i; g the local gravity; $\bar{Z}_i$ the average charge (in proton charge units)

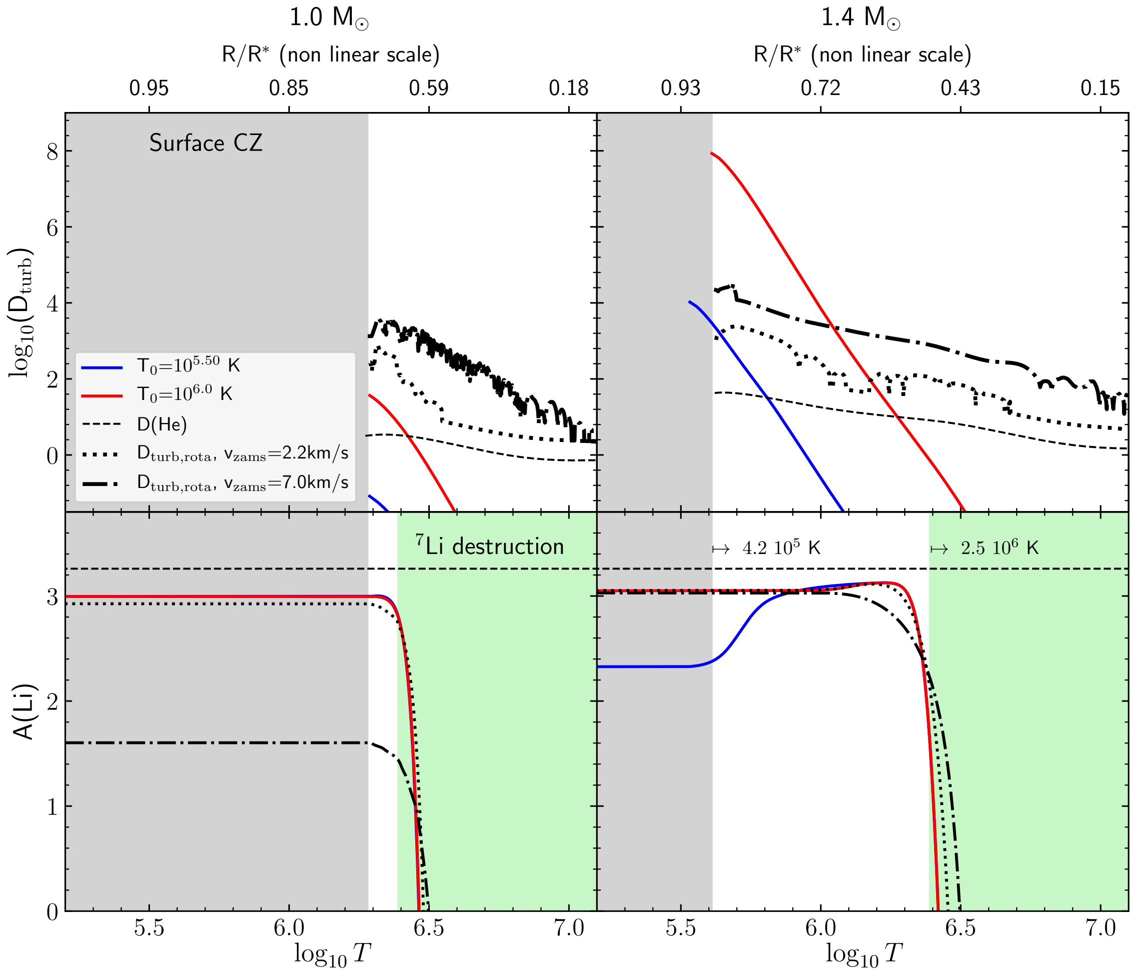

Figure 3.4: The depth-dependent profiles of the atomic diffusion coefficient according to Eq. 3.4 (upper panels) and lithium abundance (lower panels) as a function of local kinetic temperature for two stellar models with the mass of 1.0 $\mathrm{M}_\odot$ (left panels) and 1.4 $\mathrm{M}_\odot$ (right panel). Both models have an initial metallicity of [Fe/H] $= -0.05$ dex and an age of 2.5 Gyr. The profile of the atomic diffusion coefficient of He, commonly used as a reference value, is depicted with a dashed line. The blue and red lines correspond to different choices of the reference temperature T$_0$ (see also Eq. 5) resulting in different turbulent diffusion coefficient, and therefore in more (red line) or less (blue line) efficient turbulent mixing. The profiles of rotational mixing, computed using the zero-age main-sequence velocity of $\upsilon = 2.2$ and 7.0 km/s, are indicated with the dotted and dashed-dotted lines. On the lower panels the same profiles are shown in the units of predicted lithium abundance, depicting how lithium abundance would change if affected by the prescribed mixing. The grey shaded areas represent the sub-surface convective zone and the green shaded areas mark the inner regions, at $R/R* \lessapprox 0.6$ (1 $\mathrm{M}_\odot$) and $R/R* \lessapprox 0.5$ (1.4 $\mathrm{M}_\odot$), where lithium is destroyed by nuclear reactions. For more details we refer the reader to Sect. 3.4.3 and Sect. 3.4.2.

of element i (roughly equal to the charge of the 'dominant ion'); k the Boltzmann constant; T the local temperature; and κ_T the thermal diffusivity.

CESTAM computes atomic diffusion, including radiative acceleration, taking into account partial ionization for H, ^{3}He, ^{4}He, ^{6}Li, ^{7}Li, ^{9}Be, ^{11}B, ^{12}C, ^{13}C, ^{14}N, ^{15}N, ^{15}O, ^{16}O, ^{17}O, ^{22}Ne, ^{23}Na, ^{24}Mg, ^{27}Al, ^{28}Si, ^{31}P (without radiative acceleration), ^{32}S, ^{40}Ca, and ^{56}Fe. Radiative accelerations for light elements (below carbon) are not computed because they are negligible. Radiative accelerations are computed using the Single Valued Parameters (SVP) approximation (Alecian & LeBlanc, 2002, LeBlanc & Alecian, 2004). The uncertainty of $g_{rad,i}$ provided by this method is about 30% (Georges Alecian, private communication).

When rotation is included in the models, the turbulent diffusion coefficient is added to D_{turb}. A description of the treatment of rotation in the CESTAM code can be found in Marques et al. (2013). We considered the magnetized wind braking of Matt et al. (2015, 2019) and an additional vertical viscosity of $\nu_v = 10^8$ cm^{2}s^{-1} as calibrated by Ouazzani et al. (2019) to take into account the fact that the current rotation theory underestimates the transport of angular momentum. The other aspects of these models are the same than the ones presented in Deal et al. (2020). These models are only used to show that rotation may explain lithium depletion on the main-sequence.

The implementation of turbulent mixing D_{turb} follows the standard phenomenological recipe (Richer et al., 2000, Richard et al., 2001, 2002, Michaud et al., 2011). The prescription for D_{turb} is not grounded in any ab-initio model, but is chosen to not affect the transport of the chemical elements close to the center, as the efficiency of mixing drops with ρ^{-n}:

$$D_{\mathrm{turb}} = \omega D_{He}(T_0) \left(\frac{\rho(T_0)}{\rho}\right)^n, \tag{3.4}$$

where ω and n are constants, ρ is the density, and $D_{\mathrm{He}}(T_0)$ the atomic diffusion coefficient of helium at the reference temperature T_0. We assume $\omega = 400$ and $n = 3$. The atomic diffusion coefficient of helium was obtained using an analytical approximation as described by Eq. 3.5.

$$D_{\mathrm{He}} = 3.3 \times 10^{-15} T^{2.5} / [4\rho \ln(1 + 1.125 \times 10^{-16} T^3/\rho)] \tag{3.5}$$

(Michaud et al., 2011) and depends therefore on local conditions. As Richard (2005) and Gruyters et al. (2016) showed, these values provide a good fit to the observed data of metal-poor clusters. The parameter $\rho(T_0)$ represents the density at the reference temperature. In this discussion we use T_0 (see Eq.3.4) as a proxy of the turbulent mixing efficiency. By choosing different values of T_0, we effectively change the spatial extension of the zone, in which the turbulent mixing takes place. In other words, larger T_0 corresponds to a deeper base of the zone subject to the additional mixing and a larger turbulent diffusion coefficient. Therefore, the additional mixing is more efficient at competing with the atomic diffusion at higher T_0 values.

3.4.3 The impact of atomic diffusion and mixing on chemical abundances

Figure 3.4 shows the behaviour of the turbulent mixing coefficient $D_{\rm turb}$ in the models of a 1.0 $M_\odot$ star (left panels) and 1.4 $M_\odot$ star (right panels) with the age of 2.5 Gyr and $[Fe/H]_{\rm ini} = -0.05$ dex. The convective core is located at $\log T > 7.145$ for the 1.4 $M_\odot$ model and is not shown in the plot. In the top panels, we have colour-coded the profiles of $D_{\rm turb}$ by their corresponding T_0 values. The $T_0 = 10^{6.0}$ K model (solid red line) corresponds to the maximum penetration of the deep mixing zone, down to $R/R^* \sim 0.4$ in both models. On the other hand, the $\log T_0 = 10^{5.50}$ K model (blue line) has a very shallow mixing zone, which only reaches down to $R/R^* \sim 0.7$. The atomic diffusion coefficient of He is marked with the dashed line; this quantity represents a mean efficiency of atomic diffusion. Also the profile of rotational mixing, $D_{\rm rot}$, with zero-age MS velocities of $\upsilon = 2.2$ and 7.0 km/s are indicated.

The lower panel of Figure 3.4 shows the profiles of Li abundances corresponding to all aforementioned models. To aid the interpretation of this figure, we also show the surface convective zone of the model with $T_0 = 10^6$ K (grey area) and the Li destruction zone ($T > 2.5 \times 10^6$ K, green area). The radial extent of the surface convective zone is slightly different for the models with other T_0 values. This figure helps to understand why the surface abundance of Li is so sensitive to the exact prescription adopted for turbulent and rotational mixing. In particular, the surface abundance of Li decreases faster with either (a) decreasing the size of the turbulent mixing zone (decreasing T_0) or (b) increasing the depth of the convective envelope (or decreasing the mass of a star). In the former case, the larger the T_0, the stronger is the mixing below the convective envelope, that counterbalances the effects of atomic diffusion (driven by gravitational settling) on lithium. In the latter case, the model with a lower mass (1.0 $M_\odot$) has a deeper convective envelope that acts as a source of efficient mixing and, therefore, quenches atomic diffusion. Turbulent mixing helps to avoid strong surface abundance variations of all chemical elements, but it is not efficient enough to bring Li down to its nuclear destruction region. On the contrary, rotation is able to induce a lithium destruction but not to reduce strong surface abundance variations of chemical elements (Deal et al., 2020). Indeed, the 1.0 $M_\odot$ model, which includes rotational mixing, reduces the surface Li abundance by more than one order of magnitude. This effect is much less important for more massive stars, owing to their shallower convective envelopes.

Figure 3.5 shows the profiles of radiative acceleration for Fe, Ca, and Mg, in comparison with the profile of gravitational acceleration for the same 1.0 $M_\odot$ (upper panel) and 1.4 $M_\odot$ (lower panel) models. By comparing the profiles of $g_{\rm rad}$ and $g_{\rm grav}$, we can see how the balance of two forces modifies the behaviour of the elemental abundances with depth. In general, owing to $g_{\rm rad} > g_{\rm grav}$ at the bottom of the surface convective zone, heavy elements tend to accumulate at the surface of a star (or inside if the accumulation occurs deeper, Richard et al. 2001, Théado et al. 2009, Deal et al. 2016), more so in the more massive model with 1.4 $M_\odot$. And even if $g_{\rm rad} < g_{\rm grav}$, radiative acceleration will moderate the efficiency of gravitational settling. The behavior at larger depths is very non-linear, which is caused by the complex dependence of the opacity on the ionization state of the elements, and, consequently on the density and temperature profiles in the interior (Richer et al., 1998). If we consider no additional transport processes in the 1.4 $M_\odot$ model, iron and magnesium should be accumulated at the surface and calcium would be depleted.

Figure 3.6 shows $D_{\rm turb}$ at the bottom of the surface convective zone for different T_0 (colored solid lines) and, $D_{\rm He}(T_0)$ the helium diffusion coefficient at the temperature $T_0 = 10^{5.7}$ K (dashed line), according to the mass of stellar models. $D_{\rm turb}$ increases at the bottom of surface convective zone with increasing stellar mass for two reasons. The first one is due to the shallower convective zone in the more massive stars, which implies that the reference temperature T_0 is far deeper from the bottom of the surface convective zone, which induces a large turbulent diffusion coefficient according to Eq. 3.4. The second reason is the $D_{\rm He}(T_0)$ increasing with the stellar mass as the internal structure in varying with mass at a given internal temperature, among other things ρ, which induces a $D_{\rm He}(T_0)$ value varying of two order of magnitude between 0.8 and 1.4 $M_\odot$.

The model predictions for the surface abundances of Fe, Mg, Ca, and Li are shown in Fig. 3.7. All models correspond to the age of 2.5 Gyr, consistent with our observational constraints. Considering an age uncertainty of 0.2 Gyr leads to the difference in the predicted surface abundances of maximum 0.005 dex in the models for which atomic diffusion is the most efficient. The models differ in the value of T_0. Not surprisingly, the surface element abundances do not remain constant with the evolutionary phase of a star, unless extreme values of turbulent mixing, T_0 superior to 10^6 K (equivalent to $D_{\rm turb} > 10^8$ cm^2.s^{-1} at the bottom of the surface convective zone for the 1.4 $M_\odot$ model as shown in Fig. 3.6), are adopted. Similarly, the effect of radiative levitation is to prevent for some chemical elements the 'metal sink' effect of gravitational settling, allowing the model to avoid critical surface under-abundances of metals.

The evolution of Mg and Fe along the isochrone is very similar. The abundances of

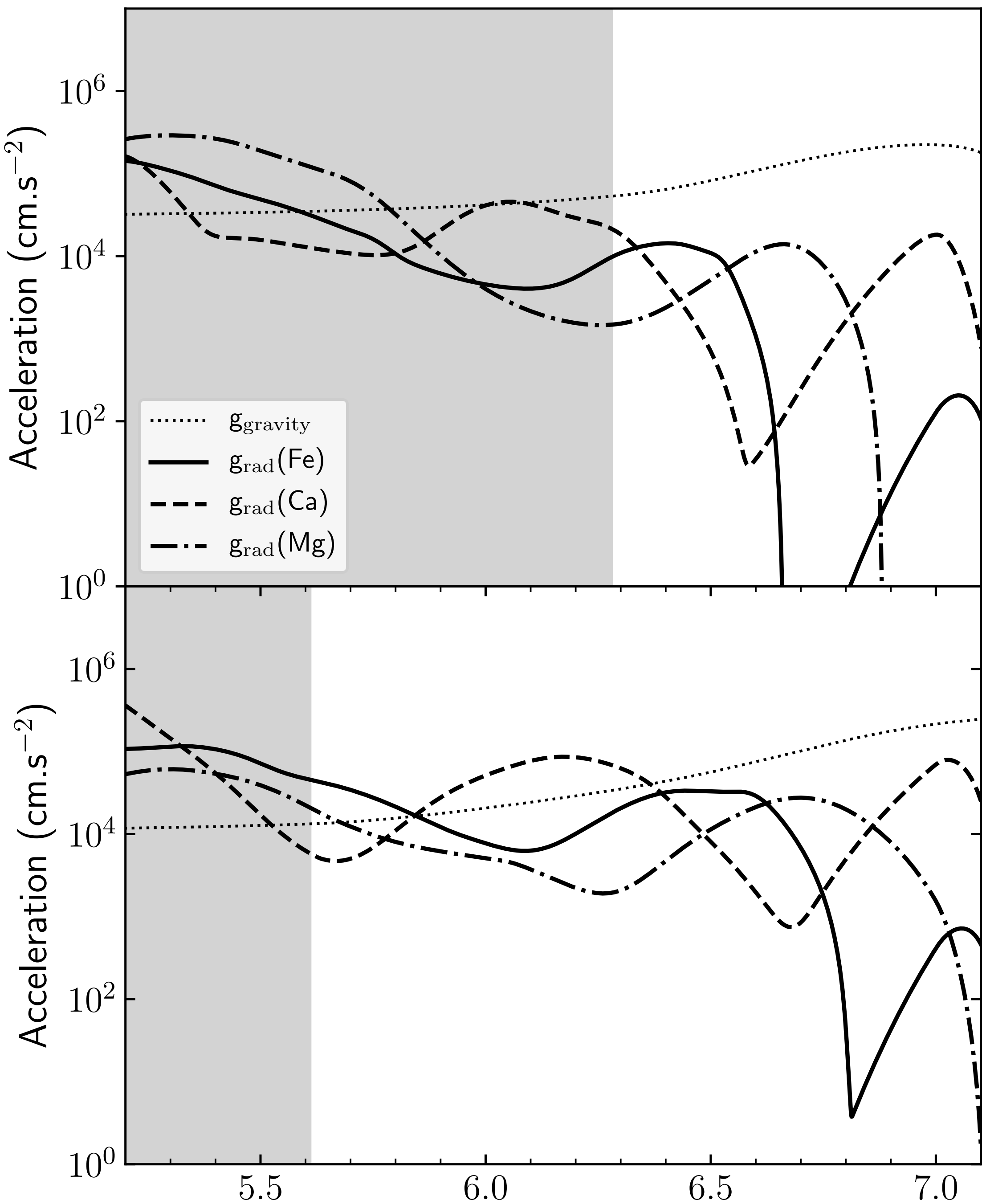

Figure 3.5: Acceleration of the gravity and radiative accelerations for iron, calcium and magnesium according the temperature of a 1.0 $\mathrm{M}_\odot$ (upper panel) and 1.4 $\mathrm{M}_\odot$ (lower panel) at 2.5 Gyr with an initial [Fe/H] of -0.05. The grey areas show the extension of the surface convective zones.

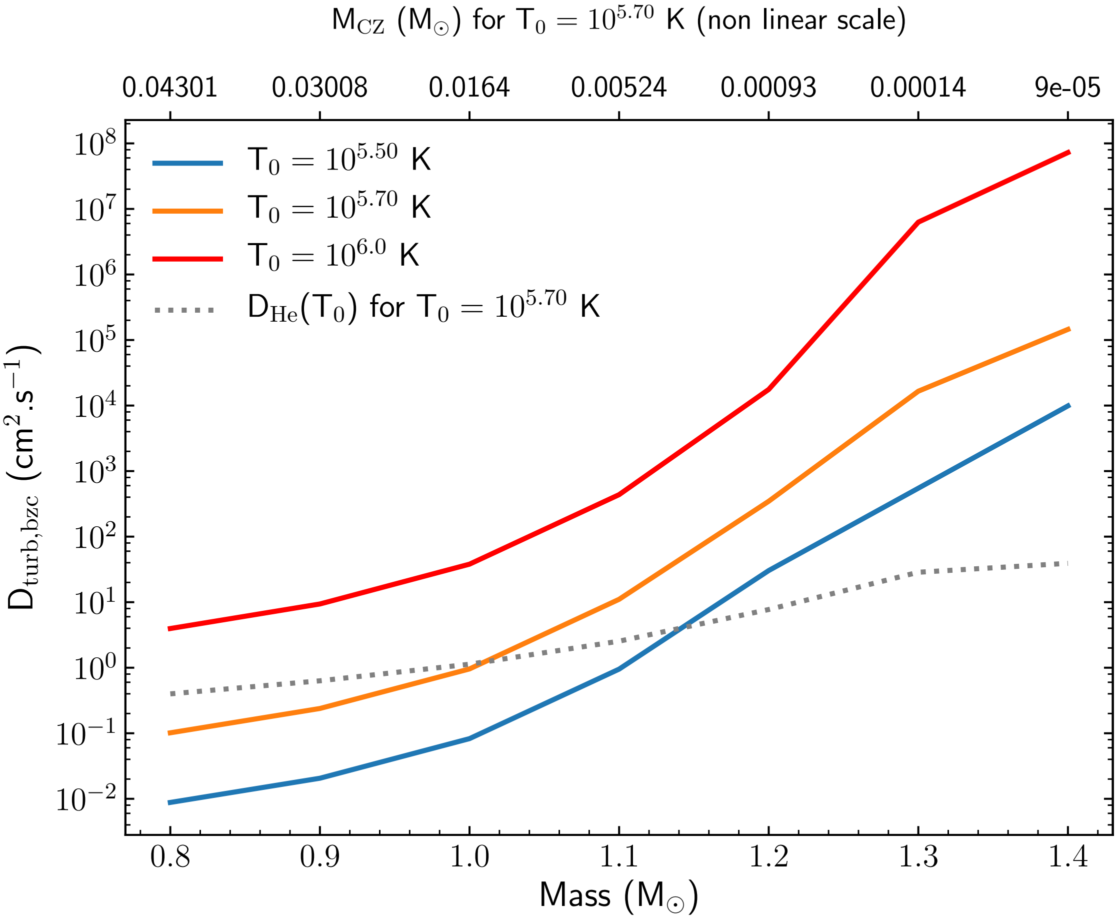

Figure 3.6: $D_{\rm turb}$ for different values of T_0 at the bottom of the surface convective zone according to the mass of the models. The masses of surface convective zone is shown in the upper x-axis.

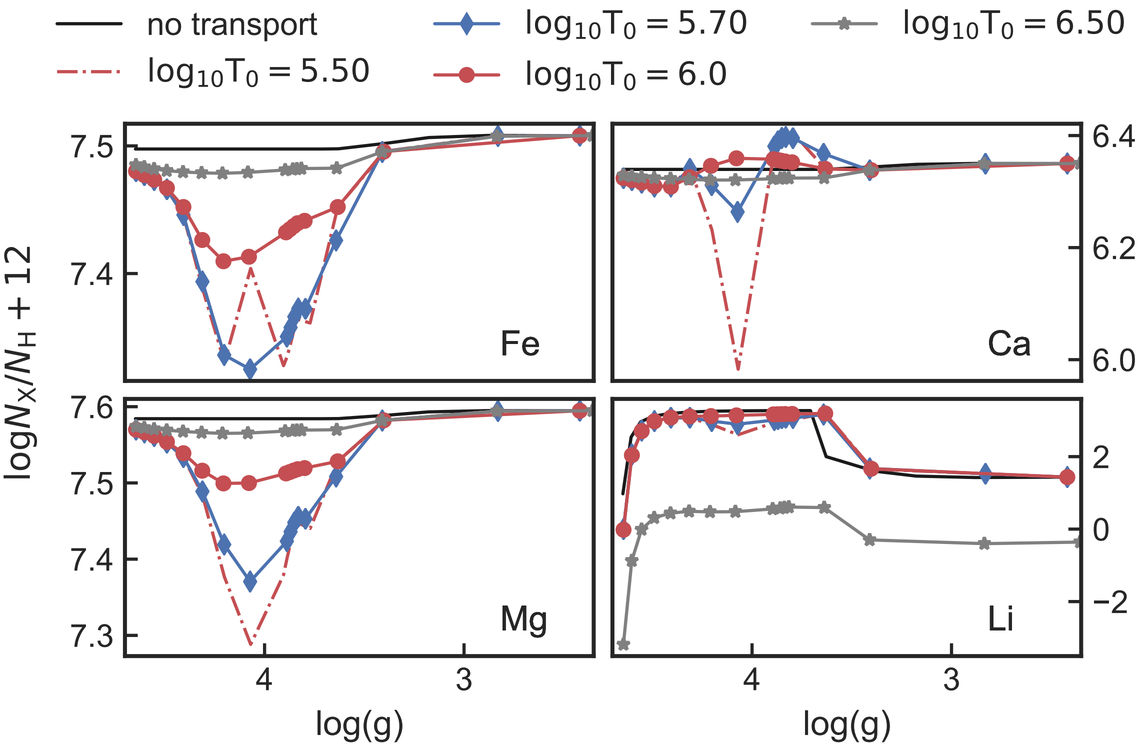

Figure 3.7: Surface abundances against the $\log g$ as predicted by the models at $[\mathrm{Fe/H}]_{initial} = -0.05$. Different colors represent different transport prescriptions adopted in the models.

both elements are significantly depleted at the TO point of the cluster, which corresponds to $\log g \approx 4.3$ dex for the most metal-poor model and to $\log g \approx 4.1$ dex for the solar metallicity model. Ca, in contrast, displays a modest overabundance at the TO point, although this behaviour can be inverted for certain combinations of $\log T_0$ and initial abundances. Increasing $\log T_0$ generally flattens the tracks of [A/H] towards the initial abundances as the value of D_{turb} is increasing at the bottom of the surface convective zone (Fig. 3.6). The transition from the main sequence to the sub-giant phase is associated with a large depletion of Li, as the surface convective envelope deepens and Li-poor material is advected to the surface.

Of note is the non-linear behaviour of the models in the domain of inefficient turbulent mixing, $\log T_0 \leq 5.50$. In this regime, turbulent mixing, is no longer sufficient to balance the outward radiation force. This imbalance induces a relative accumulation of an element at the surface, which may even result in an over-abundance of the element relative to its initial unperturbed value. This process is responsible for the characteristic bump in the behavior of Ca abundances in the transition region between the TO point and the subgiant branch and globally reduces the Fe and Mg depletion. This kind of effect can also be seen on iron in Fig. 3.7.

3.5 Results

Over the past decade, several observational studies reported clear and systematic evolutionary trends in the chemical abundances in open and globular clusters. These trends are commonly attributed to the effect of atomic diffusion. However, it was also shown that atomic diffusion alone is not sufficient to explain the observations of different chemical elements. Therefore, additional mixing processes of macroscopic nature were put forward (e.g. Mucciarelli et al., 2011, Korn et al., 2007, Nordlander et al., 2012, Gruyters et al., 2016).

In this section, we compare our new observational data with different models described in Sect. 3.4 and discuss the results in the context of other empirical and theoretical studies.

3.5.1 Intra-cluster abundance variations

Our 3D NLTE distributions of chemical abundances in NGC 2420 stars are shown in Fig. 3.8. The measured abundances of Fe, Ca, and Mg are significantly lower at the cluster TO point, with a maximum depletion of -0.2 dex relative to the lower MS or RGB stars. This prominent under-abundance gradually disappears along the SGB and the abundances attain their original (birth composition) values at the base of the RGB, around $\log g \approx 3.3$ dex. The depletion at the cluster TO is also predicted by stellar models computed with atomic

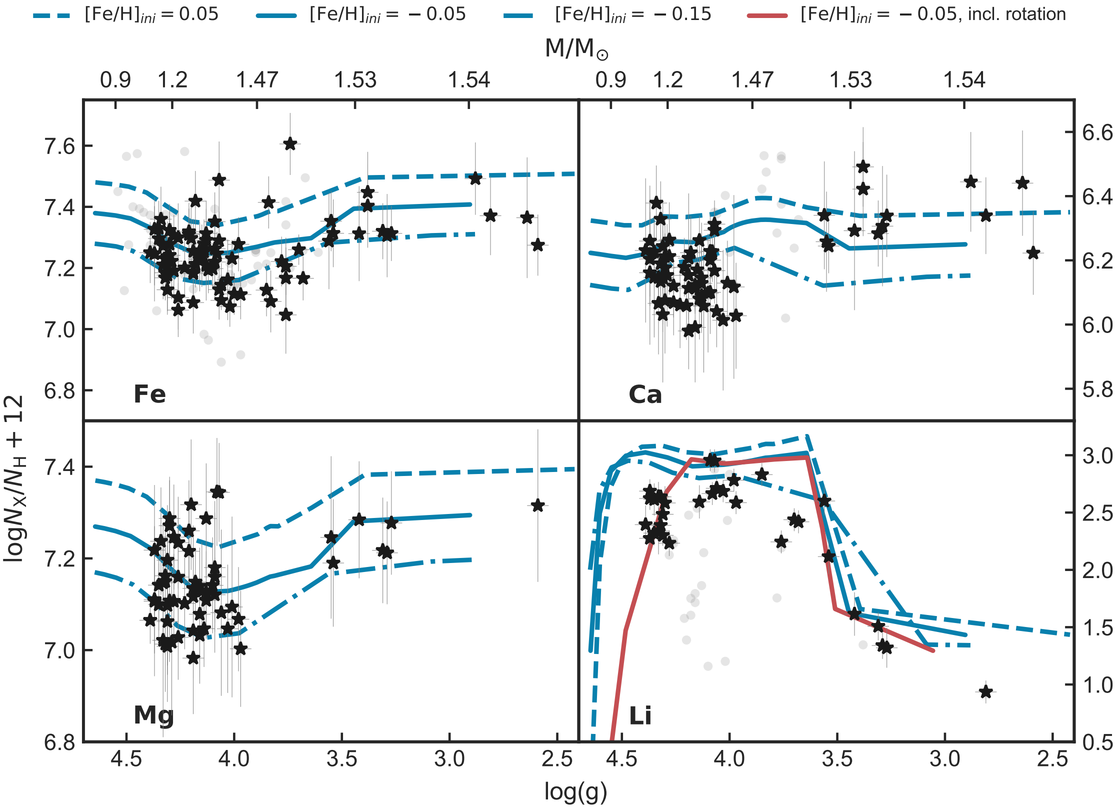

Figure 3.8: 3D NLTE photospheric abundances of Fe, Mg, Ca, and Li in stars of the NGC 2420 cluster (in black). Grey background symbols depict non-detections or abundances derived from spectra with low S/N and/or high rotational broadening. Lines correspond to the model predicted abundance variations due to atomic diffusion, incl. radiative acceleration, and turbulent mixing (T5.80 prescription) at various *initial* metallicities. The models are computed with solar chemical mixture for all elements except Mg, which has abundance on the RGB stage 0.2 dex lower than the Sun. Red line corresponds to the model with included rotation in addition to the T5.80 turbulent mixing that successfully explains observed Li abundance on the low main-sequence. For more details on comparison of observations and models see Sect. 3.5.3.

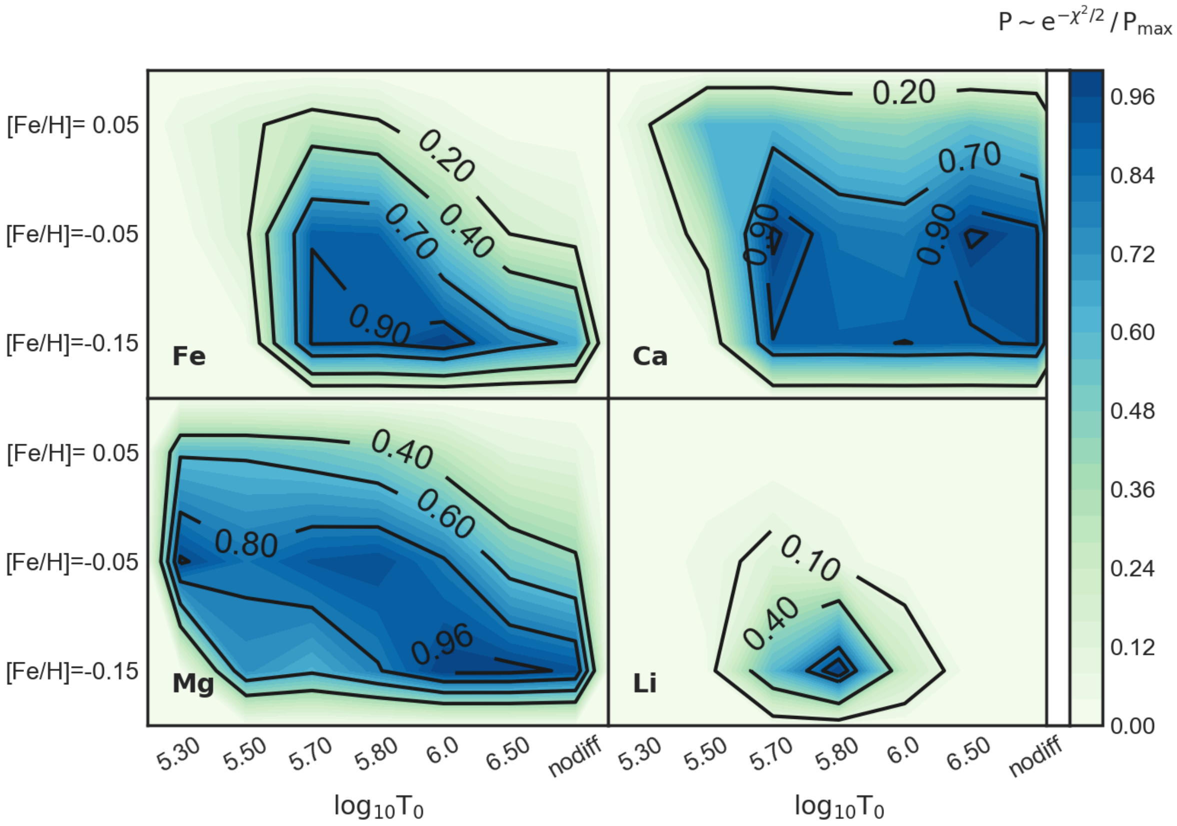

Figure 3.9: Probability distributions for all stars in NGC 2420. Note that each panel represents one chemical element only (see inset).

diffusion and turbulent mixing. One of such models, computed using the T_0 of $10^{5.8}$ K and several values of initial metallicity, is overplotted onto the observed data. The undulations of theoretical profiles for stars in the mass range from 1.1 to 1.3 $M_\odot$ ($\log g$ range from 4.5 to 3.5) are caused by the interplay of gravitational settling, radiative pressure, and turbulent mixing, as described in Sect. 3.4.3. However our data are not accurate enough to resolve these tiny signatures, which would require the abundance accuracy of better than 0.05 dex. Nonetheless, the global systematic trends in the data agree very closely with the models. On the RGB, the deepening of the surface convective zone after the MS stage quickly restores the surface abundances of elements, which are not affected by nuclear reactions (Fe, Ca, Mg), to their initial value.

3.5.2 Distribution of Li abundances

The behaviour of Li in the cluster is qualitatively different from the behaviour of other elements. In contrast to other elements, the profile of Li with $\log g$ cannot be fully described by our standard models that include atomic diffusion and turbulent mixing only. As seen in the bottom right panel of Fig. 3.8, the observed abundances of Li on the MS (at $\log g \sim 4.3$ dex) are lower, compared to standard models. However, this problem can be solved by including, in addition, internal rotation, because this physical mechanism acts throughout the entire star and, therefore, allows for mixing in the deeper regions, which are hot enough to destroy Li. In the model computed with $\upsilon \approx 7.0$ km/s, transport induced by internal rotation leads to earlier destruction of Li and results in the characteristic depletion of Li abundance on the MS, in agreement with the observations.

In addition, at $\log g \sim 4.3$ dex, there are a few data points that suggest the presence of the Li dip (Deliyannis et al., 2019), that is the depletion of Li abundances compared to stars with higher and lower $\log g$ values. This dip was also seen in other light elements, like Be (Smiljanic et al., 2010), but its origin is still debated.

The abrupt depletion of the Li abundance on the subgiant branch, predicted by the model, is also seen in our observational data. The first dredge-up brings highly-processed Li-poor material from the interior to the surface of a star. Consequently, the Li abundance drops by two orders of magnitude at the base of the RGB. CESTAM models with rotation predict a lower abundance of lithium on the SGB phase due to the deeper mixing induced by rotation.

The effect on the other elements is much smaller as rotation only impacts the size of the region where the chemical composition is homogenized. In the case of the $T_0 = 10^{5.8}$ K the region is extended by only a few % in mass, which leads to the change of observed abundance of ∼0.07 dex. In contrast to that, atomic diffusion and the parametrise mixing lead to depletion of Fe by 0.2 dex. The impact of adding rotation on the other element will be investigated in a forthcoming paper.

3.5.3 Combined statistical analysis of data and models

Figure 3.9 depicts the probability maps, which we employ to constrain the models consistent with our data. The maps were constructed by using a grids of CESTAM tracks for a cluster of a given age and different initial metallicities as described in Sect. 3.4. We perform the comparison between the observed abundance trends in NGC 2420 and a grid of CESTAM models by computing a likelihood for each of these models as described by Eq. 3.6, where χ^2_k is a chi-square per degree of freedom showing the goodness of fit by a certain model and

$[\mathrm{X/H}]_{\mathrm{i}}^{\mathrm{Obs/Mod}}$ are observed and theoretically predicted abundances respectively. Statistical and systematic observational uncertainties described in Sect. 3.3.3 were taken into account. To ease the comparison between different elements we present normalised values of the likelihoods on the maps. This representation doesn't affect our conclusions.

$$P = e^{-\chi_k^2/2}, \;\; \chi_k^2 = \left(\sum_{i}^{N_{obs}} \frac{([\mathrm{X/H}]_{\mathrm{i}}^{\mathrm{Obs}} - [\mathrm{X/H}]_{\mathrm{i}}^{\mathrm{Mod}})^2}{\sigma^2_{[\mathrm{X/H}]_{\mathrm{i}}^{\mathrm{Obs}}}} \right) / k \tag{3.6}$$

Clearly each chemical element shows a different sensitivity to the input parameter space of the models. For some elements, i.e. Ca, it is barely possible to distinguish stellar models with different levels of physical complexity. One should also take into account that the response to transport processes is different for every element. In Sect. 3.4.3 we show that the Li abundance on the MS is very sensitive to rotation, while for other elements the effect of rotation is negligibly small. Thus the abundance of Li alone would not be sufficient to identify the most likely model. The degeneracy can be broken by combining the constraints from all four chemical elements simultaneously.

The combined analysis of all elements in our data set suggests that the model that is favoured by our data the most has a modest mixing efficiency of $\log T_0 = 5.8$ (Fig. 3.10). This model reproduces the intra-cluster distributions of the abundances of all measured chemical elements against fundamental parameters of stars. Other models computed assuming significantly higher ($\log T_0 = 6.0$) or significantly lower ($\log T_0 = 5.5$) efficiency of turbulent mixing or assuming no atomic diffusion at all, are not supported by our data.

In summary, our observational data for NGC 2420 yields strong constraints on the physical processes in stellar interiors. Combining four chemical elements - Fe, Ca, Mg, and Li - we are able to confine the parameter space of the stellar models and to identify the most probable range of values that characterise the efficiency of turbulent mixing at the bottom of the stellar convective envelope. The CESTAM model, which includes atomic diffusion, turbulent mixing with $\log T_0 = 5.8$, and rotational mixing is best supported by our data. Other stellar models, in particular including those computed without atomic diffusion, are ruled out at a high level of confidence.

3.6 Discussion

Similar attempts to constrain the transport of chemical elements in the stellar interior using observations were carried out in several other studies (e.g. Korn et al., 2006, 2007, Mucciarelli et al., 2011, Nordlander et al., 2012, Gruyters et al., 2014, 2016). However, most

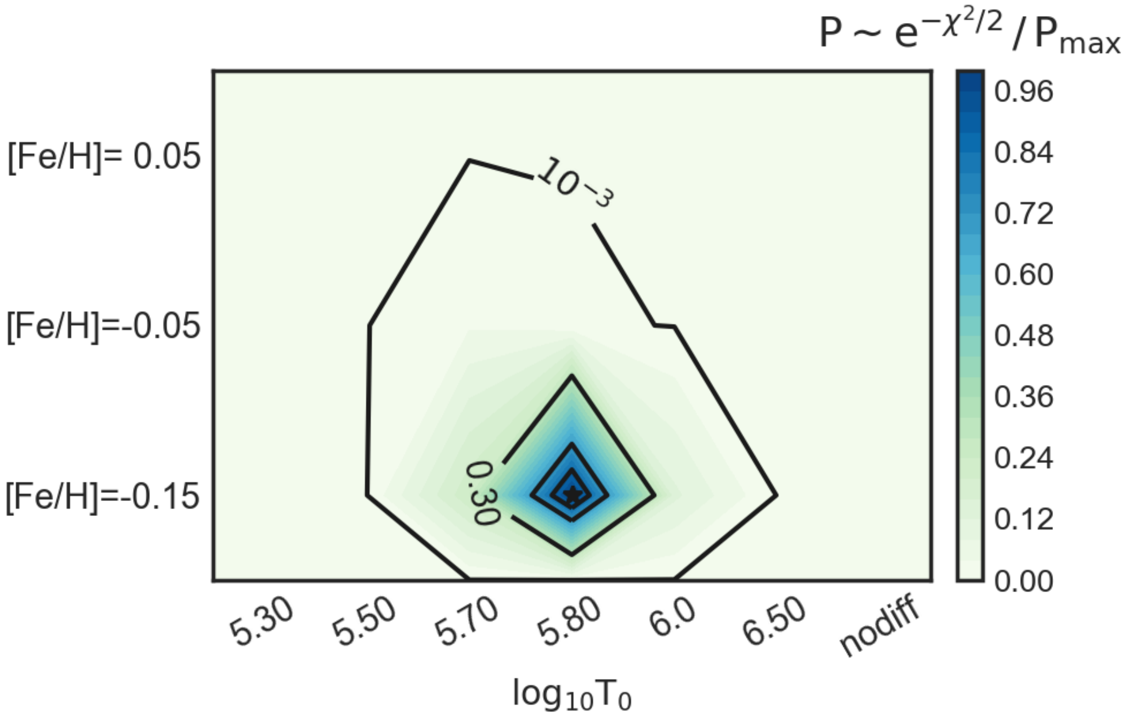

Figure 3.10: Combined probability distributions for all stars in NGC 2420, computed using all four elements simultaneously. The most-probable solution corresponds to the CESTAM model with atomic diffusion and a modest efficiency of turbulent mixing ($\log T_0 = 5.70$).

of these studies are limited to the analysis of old (over 10 Gyr) and metal-poor ([Fe/H] $\lesssim -1$ dex) Galactic clusters. Using the globular clusters NGC 6397 ([Fe/H] $= -2$ dex) and M 30 ([Fe/H] $= -2.3$ dex) they constrained $\log T_0 = 6$. This value is at the upper boundary of our estimated range of $\log \mathrm{T}_0$ from 5.70 to 6.00. The difference with our results, which are based on the young cluster with a slightly sub-solar metallicity NGC 2420, may indicate a metallicity dependence of the efficiency of mixing processes, such as rotational and turbulent mixing, competing with atomic diffusion. This metallicity dependence is clearly present in the stellar evolution models (Fig. 8, compare models computed with [Fe/H] = -0.15 and 0.05 dex) and combining the results from the afore-mentioned studies, we can conclude that there is a significant evidence for a different efficiency of T_0 at lower metallicities.

Comparing our results with previous studies of open clusters, we find a good agreement in the slopes of abundance trends and behaviour of individual chemical elements. M67 - a 4 Gyr old solar-metallicity cluster - is arguably the best-studied system in this respect (Yong et al., 2005, Randich et al., 2006, Önehag et al., 2014, Bertelli Motta et al., 2018, Souto et al., 2018, Gao et al., 2018). The last study is similar to our work in that it is based on the NLTE analysis of abundances of several chemical elements. They use the MESA stellar models from Dotter et al. (2017) computed with account for atomic diffusion, radiative acceleration, overshoot, and turbulent mixing calibrated on the observed data for NGC 6397 from Korn et al. (2007). However, although their findings are generally consistent with the MESA models, they stress non-negligible differences on the RGB and red clump, especially for the key elements, such as Mg, Na, and Fe. This conclusion is corroborated by Souto et al. (2019), who also include odd-Z species, such as N, K, V, Mn, in the analysis. They confirm systematic depletion of metals at the cluster TO, as seen in previous studies. They also find a non-negligible abundance spread at all evolutionary phases. The most recent study of M67 by Liu et al. (2019) based on 3D NLTE and 1D NLTE for selected chemical elements confirms chemical inhomogeneity in M67, reinforcing evidence for signatures of atomic diffusion in the cluster. Whereas they make no attempt to quantitatively constrain the mixing processes, they emphasise the need to include such models in studies of stellar populations and chemical evolution.

Verma & Silva Aguirre (2019) showed that the analysis of acoustic glitches in asteroseismic data can be used to constrain turbulent mixing. Their results for three Kepler targets yield $\log \mathrm{T}_0$ in the range from 5.9 to 6.0, when comparing the effect on surface abundances, which is also slightly higher compared to our results. We note, however, that their parametrisation of turbulent mixing (and hence, their definition of T_0) is not exactly the same as ours. Nevertheless, overall the conclusions of our and their study are similar taking into account both models and observations uncertainties. This fact is re-assuring, because the two methods to constrain the efficiency of mixing processes in stellar interiors are entirely independent.

3.7 PERSPECTIVES

Our findings of the relevance of atomic diffusion and mixing in stellar evolution are important in the context of other areas of astrophysics.

The most obvious consequence of our study is that accurate identification of membership in stellar associations, open and globular clusters, *cannot* rely on metallicity. This is still a common procedure in studies of stellar clusters (e.g. Blanco-Cuaresma & Fraix-Burnet, 2018, Donor et al., 2020). However, it obviously leads to biases in the population statistics and determination of the age of cluster and its metallicity.

The next interesting consequence arises in the context of chemo-dynamical structure and evolution of the Galaxy. It is common to associate the present-day position of a star and its observed abundance pattern to its initial chemical composition, corresponding to that of the interstellar matter or star-forming region in which the star formed (Casagrande et al., 2011, Bensby et al., 2014, Bergemann & Nordlander, 2014, Recio-Blanco et al., 2014, Hansen et al., 2019, Hayden et al., 2020), modulo the effects of kinematic mixing and radial migration (e.g. Schönrich & Binney, 2009). This information is used to infer quantities describing the present-day Galactic structure, ignoring the significant systematic effects that secular stellar evolution has on the photospheric abundances of stars. In turn, this causes a systematic bias in radial gradients, metallicity distribution functions, and even age-metallicity relationships, because the determinations of stellar ages by means of isochrone fitting are also affected by the problem of selective enhancement or depletion of abundances in different evolutionary phases (e.g. Jofré & Weiss, 2011, Salaris, 2016, Dotter et al., 2017).

Our results suggest that stellar abundances can be used to constrain the history of the Galaxy under the condition that stellar evolution models, and therefore, the stellar yields, implemented in Galactic Chemical Evolution (GCE) models, take atomic diffusion and mixing into account. An alternative solution is to restrict the analysis to the samples of stars, for which observed abundances patterns are not significantly affected by diffusion and mixing. The available evidence suggests that RGB stars, young (< 1 Gyr) and slowly rotating (< 5 km/s) stars, as well as low mass ($< 0.9\mathrm{M}_{\odot}$) unevolved main sequence stars, are relatively robust tracers of the initial composition of the interstellar matter, whereas solar-like main-sequence stars, turn-off stars, subgiants - which dominate local Galactic neighbourhood and are very populous in samples like the GALAH (Buder et al., 2019) - are to be treated with caution. Moreover, this selective approach requires accurate determination of stellar masses and robust statistical modelling of selection functions in order to quantify the bias in the population statistics arising from target selection.

3.8 Conclusions

We presented a homogeneous analysis of Gaia-ESO spectra of stars in the open cluster NGC 2420 - a relatively young (2.5 ±0.5 Gyr) and metal-rich massive cluster at a distance of $\sim$ 2.5 kpc (Cantat-Gaudin et al., 2018). About 30% of stars in the cluster could be unresolved main-sequence binaries according to method described in Cordoni et al. (2018).

The spectra were taken with the Giraffe medium-resolution ($19\,200 \leq R \leq 21\,500$) spectrograph at the VLT. We combined our spectroscopic analysis with photometry and astrometry from Gaia DR2. Our sample includes $\sim$ 84 stars and covers the full evolutionary sequence in the cluster, from G-type stars on the main-sequence to K-type red giants. We used NLTE atomic models, as well as 1D hydrostatic (MARCS) and averaged 3D hydrodynamical (STAGGER) model atmospheres, to determine the abundances of Fe, Ca, and Mg in the cluster stars. The abundances of Li were measured using 1D LTE models and corrected for 3D NLTE effects using literature values.

We find that the chemical abundance distributions in the cluster display significant trends with the evolutionary stages of the stars. Fe, Mg, and Ca show a $\sim$ 0.1 to 0.2 dex depletion at the cluster turn-off point, but the abundances gradually increase and flatten near the base of the RGB. The abundances of Li are low for stars with $M \lesssim 1\mathrm{M}_{\odot}$, but increase for higher-mass stars and remain relatively constant at the level of A(Li) = 2.8 dex at the cluster turn-off. This value is close to the value predicted by the standard models of big bang nucleosynthesis (SBBN). Li abundances drop by two orders of magnitude on the subgiant branch, attaining A(Li) = 1.3 dex on the RGB.

We attribute the systematic difference in abundances in the cluster to atomic diffusion and mixing. Comparing our findings with CESTAM stellar evolution models (Deal et al., 2018), we find that only RGB stars with masses $\gtrapprox 1.5\mathrm{M}_{\odot}$ ($\log g \lesssim 3.5$ dex) can be viewed as robust tracers of the initial composition of the cluster. Also low-mass stars, $M \lessapprox 0.9\mathrm{M}_{\odot}$ are not expected to display self-processed photospheric abundances. Therefore, the initial chemical composition of NGC 2420 is A(Fe) = 7.35±0.1 dex, A(Mg) = 7.3±0.1 dex, A(Ca) = 6.4 ± 0.1 dex, A(Li) = 2.8 ± 0.1 dex. The present-day composition at the cluster turn-off is significantly different: A(Fe) = 7.15±0.1 dex, A(Mg) = 7.15±0.1 dex, A(Ca) = 6.14±0.1 dex. We emphasize that these chemical offsets between the low-mass and higher-mass stars are caused by physical processes during stellar evolution, and are, consequently, essential to take into account in any study that uses stellar abundances for detailed diagnostics of stellar structure, exoplanet characterisation, or Galaxy history and formation.

The results obtained in 1D LTE, 1D NLTE, and in 3D NLTE show systematic differences. RGB stars are more sensitive to NLTE effects, compared to main-sequence and turn-off stars. Our estimates of the differences between 3D NLTE and 1D LTE abundances for RGB stars amount to $\delta(\mathrm{Fe}) = 0.06$ dex, $\delta(\mathrm{Mg}) = 0.01$ dex, $\delta(\mathrm{Ca}) = 0.04$ dex. For the turn-off stars, the 3D NLTE effects are within 0.1 dex for all elements.

We carry out a systematic, statistical analysis of the observed abundance distributions using the grid of CESTAM models, computed with atomic diffusion and different prescriptions for turbulent mixing, with and without mixing induced by rotation, as well as different initial metallicities. The combined probabilistic analysis allows us to confine the parameter space of the models and to constrain the depth of the zone in which turbulent mixing takes place, providing in the sense a quantitative assessment of the combined efficiency of microscopic and macroscopic mixing. We find that the most likely model, which is consistent with the observed trends of all elements, has $\log T_0$ of 5.7 to 6.0. This value is slightly lower than the previous literature estimates, which are based on the analysis of abundances in old globular clusters and acoustic glitches in asteroseismic data, although we warn that detailed comparisons in the latter case are hampered by different formulation of the turbulent coefficient.

4

Standard composition of the Sun

Disclaimer

This chapter was published as Magg et al. (2022). The work behind this study was performed in close collaboration with all listed co-authors. The text was written with feedback of collaborators. Section 4.2.5 is a joint contribution by Manuel Bautista, Helena Carvajal Gallego, Sébastien Gamrath, Patrick Palmeri, and Pascal Quinet. Sect. 4.3.3 is work of Aldo Serenelli. Sect. 4.4.1 is based on computations performed by Aldo Serenelli, Sarbani Basu, and Jason W. Ferguson.

Research in modern astrophysics shows an increasingly growing interest in high-precision stellar abundance diagnostics, as a source of accurate knowledge of the chemical composition of stars is relevant in studies of exoplanets (e.g. Bedell et al., 2018, Adibekyan, 2019), asteroseismology and stellar structure (Nissen et al., 2017, Deal et al., 2020), and Galaxy evolution (Bensby et al., 2014, Bergemann et al., 2018, Schuler et al., 2021). Chemical abundances can only be determined from stellar spectra, and therefore, with the Sun being the reference for any chemical diagnostics study, this effort requires self-consistent unbiased analyses of stellar and solar data. However, so far, accurate studies of solar abundances

(Caffau et al., 2011, Asplund et al., 2021) adopted methods and data, which are conceptually different from those applied to large stellar samples. In particular, solar abundances are usually determined using full three-dimensional (3D) radiation transfer NLTE methods employing spatially-resolved solar spectra taken at different pointings across the solar disc (e.g. Amarsi et al., 2018, Bergemann et al., 2021). Also, typically very weak atomic and molecular features across the entire range from the optical to mid-IR at ~ 1.5 μm are used for the solar analysis (such as the lines of OH, CN, CH, and NH, Amarsi et al. 2021), which is usually inapplicable for large samples of stars. In addition, full 3D NLTE calculations are computationally prohibitive and are currently not feasible for large stellar samples. Most large spectroscopic surveys, such as Gaia-ESO (Smiljanic et al., 2014), APOGEE (Majewski et al., 2017), and RAVE (Steinmetz et al., 2020) still have to rely on spectroscopic models computed under simplifying assumptions of LTE, one-dimensional (1D) geometry, and hydrostastic equilibrium, adopting parameterizations for convective energy transport and turbulence. GALAH (Buder et al., 2021) is the only survey that has adopted NLTE grids so far. Also, spatially-resolved spectra are not available for any other star than the Sun. Next-generation astronomical facilities, such as 4MOST and WEAVE, have stringent requirements on the quality of chemical abundance characterisation, but they will rely on medium resolution spectral data.

In this work, we provide a new analysis of the solar chemical composition. The methodology is chosen such that it is suitable for the analysis of any star, not only the Sun with its very high quality observations. We use the most up-to-date atomic and molecular data (Heiter et al., 2021, and updates described in Sect. 4.2.6), new NLTE model atoms (e.g. Semenova et al., 2020, Bergemann et al., 2021), and different solar model atmospheres (CO5BOLD and STAGGER) obtained by averaging 3D radiation-hydrodynamics (RHD) simulations of stellar convection. The latter is important in the view of the debate over the solar abundances between the two groups who use the STAGGER and CO5BOLD models. As the full 3D RHD computations are not applicable for the up-coming large spectroscopic surveys, given the complexity of the wide wavelength range abundance analysis, for this study we choose to work with 1D and average 3D model atmospheres. We focus primarily on those chemical elements that are relevant in the calculation of the standard solar models (SSMs), that is C, N, O, Mg, Si, Ca Fe, and Ni. We also carefully revisit various observational constraints on the abundance of Ne, which cannot be determined from the solar photospheric spectra. However, independent measurements based on the solar wind and corona are available (Bochsler, 2007). We select atomic spectral lines that can also be used to derive abundances from medium resolution spectral data. We also discuss the photospheric measurements of O (e.g. Bochsler, 2007, Laming et al., 2017) in the context of Ne/O ratio. We compare our results with previous estimates in the literature, also with those based on the analysis of the B-type stars in the solar neighbourhood (Nieva & Simón-Díaz, 2011, Nieva & Przybilla, 2012).

4.1 Introducing the data

We use a high-quality, high-resolution ($R = \lambda/\Delta\lambda \approx 700\,000$) solar flux spectrum obtained with the FTS instrument at the Institut für Astrophysik, Göttingen (Reiners et al., 2016, hereafter, IAG data). In Bergemann et al. (2021), we investigated the differences between solar abundance estimates obtained using the IAG data, the KPNO FTS solar flux atlas, the data acquired with the *Hinode* space based facility, and several other datasets. We found that in some cases, non-negligible differences arise due to the use of different solar atlases (see also Caffau et al., 2008). However, the differences are primarily associated with instrumental artefacts and effects of the data reduction. As a consequence, part of the discrepancies between the solar abundance estimates (e.g. Asplund et al. 2021 and Caffau et al. 2011) arguably arise because of the latter aspect, since they focus on weak features that are particularly sensitive to the details of the continuum placement.

In this work, we do not restrict the analysis to the weakest lines, but also include other spectral lines that will be accessible with next generation facilities such as 4MOST and WEAVE. As we will show in Sect. 4.3, we do not detect any significant systematic biases in abundances, caused by using lines across a broad range of equivalent widths, as long as the atomic data employed in the analysis are of a sufficiently high quality.

4.2 Measurements and some details on methods

4.2.1 Model atmospheres

We make use of three different sources of solar atmospheric models: the MARCS model (Gustafsson et al., 2008), the STAGGER model (Magic et al., 2013a,b), and the CO5BOLD model (Freytag et al., 2012).

The physical properties of the MARCS model atmosphere code were extensively described in Gustafsson et al. (2008). This is a 1D LTE model atmosphere computed under the assumption of hydrostatic equilibrium and with convective energy transfer treated according to the mixing length theory formalism of Henyey et al. (1965). The mixing length was set to 1.5 and microturbulence to 1 $\mathrm{km\,s^{-1}}$. The code relies on opacities computed using the Uppsala opacity package, which was updated to include comprehensive bound-bound and bound-free transitions in all relevant absorbers in FGK atmospheres, as well as lines

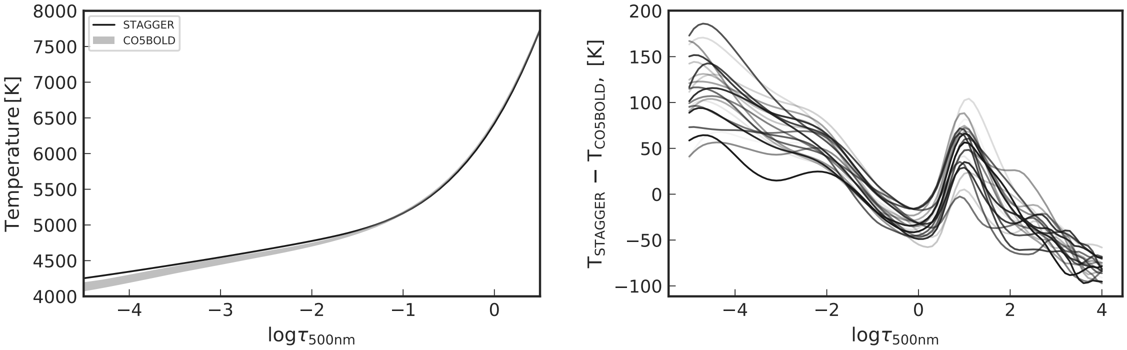

Figure 4.1: *Left panel:* temperature structure of STAGGER and CO5BOLD model atmospheres. Gray area depicts variations among temporarily resolved snapshots in CO5BOLD simulations. *Right panel:* absolute difference in temperature structure of STAGGER and CO5BOLD model atmospheres. Each line corresponds to a temporarily resolved snapshot of CO5BOLD simulations. See Sect. 4.2.2 for details.

for about 20 important molecular species. In total over 500 molecules are included in the equation of state calculations.

Here, we use the averages of these simulations[1], constructed by spatial (over surfaces of equal optical depth) and temporal averaging of the simulation cubes, as described in Bergemann et al. (2012b). These averages are known as ⟨3D⟩ model atmospheres. To represent the original 3D velocity field in the simulation cubes we include a depth-dependent velocity profile in the form of a microturbulence with a value of one standard deviation of the 3D velocity components as suggested in Uitenbroek & Criscuoli (2011). The opacities and the equation of state used in the RHD calculations are described in Magic et al. (2013a,b).

The mean CO5BOLD model (see Freytag et al., 2012, for a description of the code) was obtained by horizontal (on $\tau_{\mathrm{Rosseland}}$ iso-surfaces, first temperature moment) averaging of data blocks from a solar model simulation (internal identifier `d3gt57g44msc600`). The model is part of the ongoing extensive efforts for the development of the `CIFIST` 3D model atmosphere grid (Ludwig et al., 2009, Tremblay et al., 2013). The 3D model uses $250 \times 250 \times 207$ grid points, with an equidistant grid spacing of 32 km in the two horizontal directions, and a non-equidistant grid spacing in the vertical direction between 10 and 15 km, giving a total extension of $8.0 \times 8.0 \times 2.3\,\mathrm{Mm}^3$. The wavelength dependence of the radiative transfer was represented with 12 opacity bins. A comparison of the temperature structures of the STAGGER and CO5BOLD model atmospheres used in this study is presented in Fig. 4.1.

---

[1] `https://staggergrid.wordpress.com/mean-3d/`

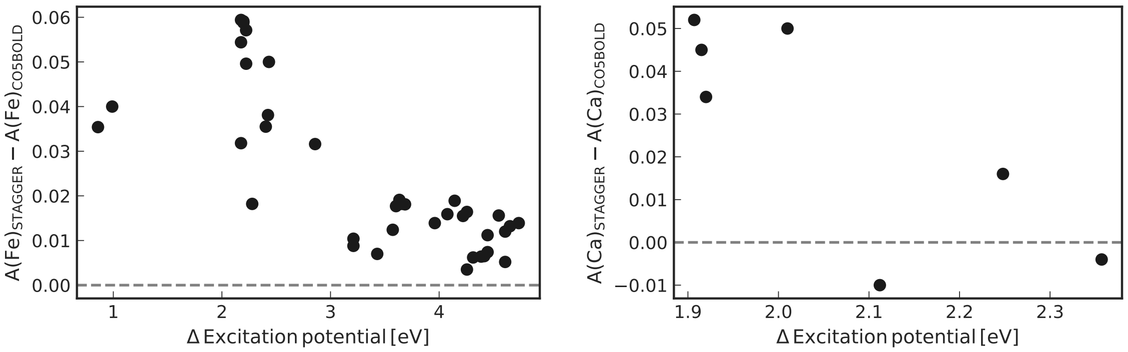

Figure 4.2: *Left panel:* predicted difference in Fe abundance computed with STAGGER and CO5BOLD model atmospheres as a function of lower level excitation potential for Fe I lines. *Right panel:* predicted difference in Ca abundance computed with STAGGER and CO5BOLD model atmospheres as a function of difference in lower level excitation potential for Ca I lines. See Sect. 4.2.2 for details.

4.2.2 Comparative analysis of CO5BOLD and STAGGER results

To test how the choice of model atmosphere affects the derived abundances, we computed the CoG for each diagnostic line of each chemical element using the CO5BOLD and STAGGER solar atmospheric models. Since there is no consensus yet on how to average the 3D velocity field, we chose to include velocity in a form of micro-turbulence and we set it to 1 $\mathrm{km\,s^{-1}}$ in both model atmospheres. By comparing the CoGs, we estimated the difference in abundance for each chemical element. It is known that NLTE radiative transfer is much less sensitive to the temperature structure of the model atmosphere Bergemann et al. (2012b), because the populations are significantly affected by the non-local radiation field. Thus, we perform the comparison in NLTE whenever possible. This predicted difference is provided in Table 4.4 and we refer to it later in the discussion when comparing abundances derived using the CO5BOLD and STAGGER models.

Overall, the STAGGER model atmosphere is hotter than CO5BOLD (Fig. 4.1), with a negligible difference around the optical depth $\log \tau_{500\mathrm{nm}} = 0$, but up to 150 K at larger optical depths. Fig. 4.2 shows that Fe I lines with lower level excitation potential $E_{\mathrm{low}} \lesssim$ 2.5 eV are very sensitive to the temperature structure of the atmosphere, and the abundances inferred from these features may differ by up to +0.06 dex depending on the detailed structure of the ⟨3D⟩ model. In contrast, the Fe abundances derived from Fe I lines with higher E_{low} values change by less than 0.02 dex. This is as expected, and confirms previous NLTE results (e.g. Bergemann et al., 2012b). Therefore, in this work, we have chosen to include only Fe I lines with high excitation potential, $E_{\mathrm{low}} \geq 2.5$ eV in the abundance analysis.

Also, the lines of Ca I show a significant sensitivity to the structure of the models. The majority of diagnostic Ca I lines in our linelist arise from levels with intermediate excitation potential, $E_{\mathrm{low}} \approx 2.5$ eV. As Fig. 4.2 demonstrates, the strong Ca I lines at 6471 and 6499 Å (with the smallest energy level differences) have the largest difference in abundance when modelled with the CO5BOLD and STAGGER model, up to 0.05 dex. Since we do not currently have a robust evidence in favour of either of these 3D RHD simulations, we opt to include all Ca lines in the analysis, given the much smaller number of diagnostic features of Ca I available for the abundance analysis compared to Fe I. The lines of all other elements, see Table 4.4, appear to be almost unaffected by the differences between CO5BOLD and STAGGER models. Therefore we use all available diagnostic lines in the calculations, not imposing any cuts on their atomic parameters.

4.2.3 Abundance analysis

The analysis of spectral lines is a two-step procedure. First, we compute NLTE atomic level populations for each of the NLTE elements described in Sec. 4.2.4 using a code that simultaneously solves the radiative transfer and statistical equilibrium equations. Second, the NLTE populations are used in a spectrum synthesis code to compute model spectra for all diagnostic lines of the selected chemical elements, taking all atomic and molecular blends self-consistently into account. The abundances are then derived by comparing the grid of model spectra with the data, employing standard χ^2 minimisation. We have verified on mock lower-resolution observed data that the abundances are not affected by reducing the resolving power and signal-to-noise ratio of the spectra by more than 0.03 dex.

For the NLTE calculations, we use the MULTI2.3 code (Carlsson, 1986), which is based on the method of accelerated lambda iteration (or ALI) and solves the radiative transfer equation using the long characteristics solver. The code was updated, as described in Bergemann et al. (2019) and Gallagher et al. (2020). The atomic populations calculated by MULTI2.3 are then used with the spectrum synthesis code Turbospectrum (Plez, 2012), that can self-consistently treat blends and compute a full spectrum including all species simultaneously.

4.2.4 NLTE model atoms

New atomic models are available for five chemical elements in our list. We describe them briefly below. The Grotrian diagrams are illustrated in Fig. 4.3.

The model atoms of O and Ni are both taken from Bergemann et al. (2021). In short, the O model includes 122 energy states of O I and O II, coupled by radiative and collision-

Table 4.1: Atomic parameters of lines of C I, N I, O I, Mg I, Si I, Si II, Ca I, Ni I, and Ni II.

Atom	λ [Å]	E_{low} [eV]	E_{up} [eV]	$\log gf$	vdW[a]	Ref.[b] f-val.	Ref.[c] vdW
C I	5052.145	7.685	10.138	-1.36 ± 0.04	−7.310	1	4
C I	6587.610	8.537	10.419	-1.05 ± 0.04	1953.319	1	1
C I	7113.171	8.647	10.390	-0.94 ± 0.04	1858.314	1	1
N I	8629.235	10.690	12.126	0.006 ± 0.07	575.234	2	1
N I	8683.403	10.330	11.757	0.162 ± 0.04	480.231	2	1
O I	6300.304	0.000	1.967	-9.72 ± 0.08	–	3	2
O I	7771.940	9.146	10.741	0.350 ± 0.02	453.234	2	1
O I	7774.170	9.146	10.741	0.204 ± 0.02	453.234	2	1
O I	7775.390	9.146	10.740	-0.019 ± 0.02	453.234	2	1
Mg I	5528.405	4.346	6.588	-0.547 ± 0.02	1461.312	4	1
Mg I	5711.088	4.346	6.516	-1.742 ± 0.05	1860.100	4	3
Si I	5645.611	4.930	7.125	-2.067 ± 0.03	−7.29	5	4
Si I	5684.484	4.954	7.134	-1.607 ± 0.05	−7.30	5	4
Si I	5690.425	4.930	7.108	-1.802 ± 0.05	1770.220	5	1
Si I	5701.105	4.930	7.104	-1.981 ± 0.05	1770.220	5	1
Si I	5772.146	5.082	7.223	-1.643 ± 0.03	−7.350	5	4
Si I	5793.073	4.930	7.069	-1.894 ± 0.1	1700.230	5	1
Si I	7034.900	5.871	7.633	-0.78	−7.13	6	4
Si I	7226.208	5.614	7.329	-1.41	−7.32	6	4
Ca I	5260.387	2.521	4.878	-1.719 ± 0.02	421.260	7	1
Ca I	5512.980	2.933	5.181	-0.464 ± 0.02	−7.316	8	4
Ca I	5867.562	2.933	5.045	-1.570 ± 0.04	−7.460	8	4
Ca I	6166.439	2.521	4.531	-1.142 ± 0.02	976.257	7	1
Ca I	6455.598	2.523	4.443	-1.340 ± 0.04	365.241	8	1
Ca I	6471.662	2.526	4.441	-0.686 ± 0.02	365.241	7	1
Ca I	6499.650	2.523	4.430	-0.818 ± 0.02	364.239	7	1
Ni I	4740.165	3.480	6.095	-1.72	844.281	9	1
Ni I	4811.983	3.658	6.234	-1.45	−7.75	10	4
Ni I	4814.598	3.597	6.172	-1.63	743.236	9	1
Ni I	4976.135	3.606	6.097	-1.26	843.282	9	1
Ni I	5157.980	3.606	6.009	-1.51	691.236	9	1
Ni I	5537.106	3.847	6.086	-2.22	695.216	9	1
Ni I	6176.812	4.088	6.095	-0.26	826.284	9	1
Ni I	6204.604	4.088	6.086	-1.08	719.247	9	1
Ni I	6223.984	4.105	6.097	-0.91	827.283	9	1
Ni I	6414.587	4.154	6.086	-1.16	721.249	9	1
Ni II	6378.250	4.154	6.097	-0.82	825.283	9	1

[a] Van der Waals broadening parameter, see text.

[b] References: (1) Li et al. (2021) (2) this work ; (3) Storey & Zeippen (2000) (4) Pehlivan Rhodin et al. (2017) (5) Henrik Hartman (in preparation, priv. comm.) (6) Garz (1973) renormalized using O'Brian & Lawler (1991) (7) Smith & Raggett (1981) (8) Smith (1988) (9) Wood et al. (2014) (10) Johansson et al. (2003)

[c] References: (1) Barklem et al. (2000) (2) Unsöld (1955) (3) P. Barklem (priv. comm.) (4) Anstee & O'Mara (1991, 1995)

Table 4.2: Atomic parameters of diagnostic Fe lines.

λ [Å]	E_{low} [eV]	E_{up} [eV]	$\log gf$	vdW[a]	Ref. [b] f-val.	Ref. [c] vdW
Fe I						
5242.491	3.634	5.999	-0.967 ± 0.046	361.248	1	1
5365.399	3.573	5.883	-1.020 ± 0.041	283.261	1	1
5379.574	3.695	5.999	-1.514 ± 0.046	363.249	1	1
5398.279	4.446	6.742	-0.630 ± 0.060	993.280	2	1
5543.936	4.218	6.453	-1.040 ± 0.050	742.238	2	1
5560.212	4.435	6.664	-1.090 ± 0.050	895.278	2	1
5638.262	4.220	6.419	-0.720 ± 0.020	730.235	3	1
5661.346	4.284	6.474	-1.765 ± 0.041	765.209	4	1
5679.023	4.652	6.835	-0.820 ± 0.050	1106.291	2	1
5731.762	4.256	6.419	-1.200 ± 0.050	727.232	2	1
5741.848	4.256	6.415	-1.672 ± 0.097	725.232	1	1
5855.077	4.608	6.725	-1.478 ± 0.041	962.279	4	1
5905.672	4.652	6.751	-0.690 ± 0.050	994.282	2	1
5930.180	4.652	6.742	-0.230	983.281	5	1
6027.051	4.076	6.132	-1.089 ± 0.051	380.250	1	1
6056.005	4.733	6.780	-0.320 ± 0.030	1029.286	3	1
6093.644	4.608	6.642	-1.400 ± 0.080	866.274	2	1
6165.360	4.143	6.153	-1.473 ± 0.051	380.250	1	1
6187.990	3.943	5.946	-1.620 ± 0.060	903.244	2	1
6270.225	2.858	4.835	-2.470 ± 0.059	350.249	8	1
Fe II						
5234.625	3.221	5.589	-2.180	180.249	10	2
5325.553	3.221	5.549	-3.160	179.252	10	2
5425.257	3.199	5.484	-3.220	178.255	10	2
6084.111	3.199	5.237	-3.881	173.223	11	2
6456.383	3.903	5.823	-2.185	185.276	11	2

[a] Van der Waals broadening parameter, see text.

[b] References: (1) O'Brian et al. (1991) (2) May et al. (1974) (3) Ruffoni et al. (2014) (4) Bard & Kock (1994) (5) Wolnik et al. (1971) renormalized to Fuhr et al. (1988) (6) average of Bard et al. (1991), Blackwell et al. (1982a), and O'Brian et al. (1991) (7) Blackwell et al. (1982a) (8) average of Bard et al. (1991) and O'Brian et al. (1991) (9) average of Blackwell et al. (1982b) and O'Brian et al. (1991) (10) Meléndez & Barbuy (2009) (11) Raassen & Uylings (1998)

[c] References: (1) Barklem et al. (2000) (2) Barklem & Aspelund-Johansson (2005)

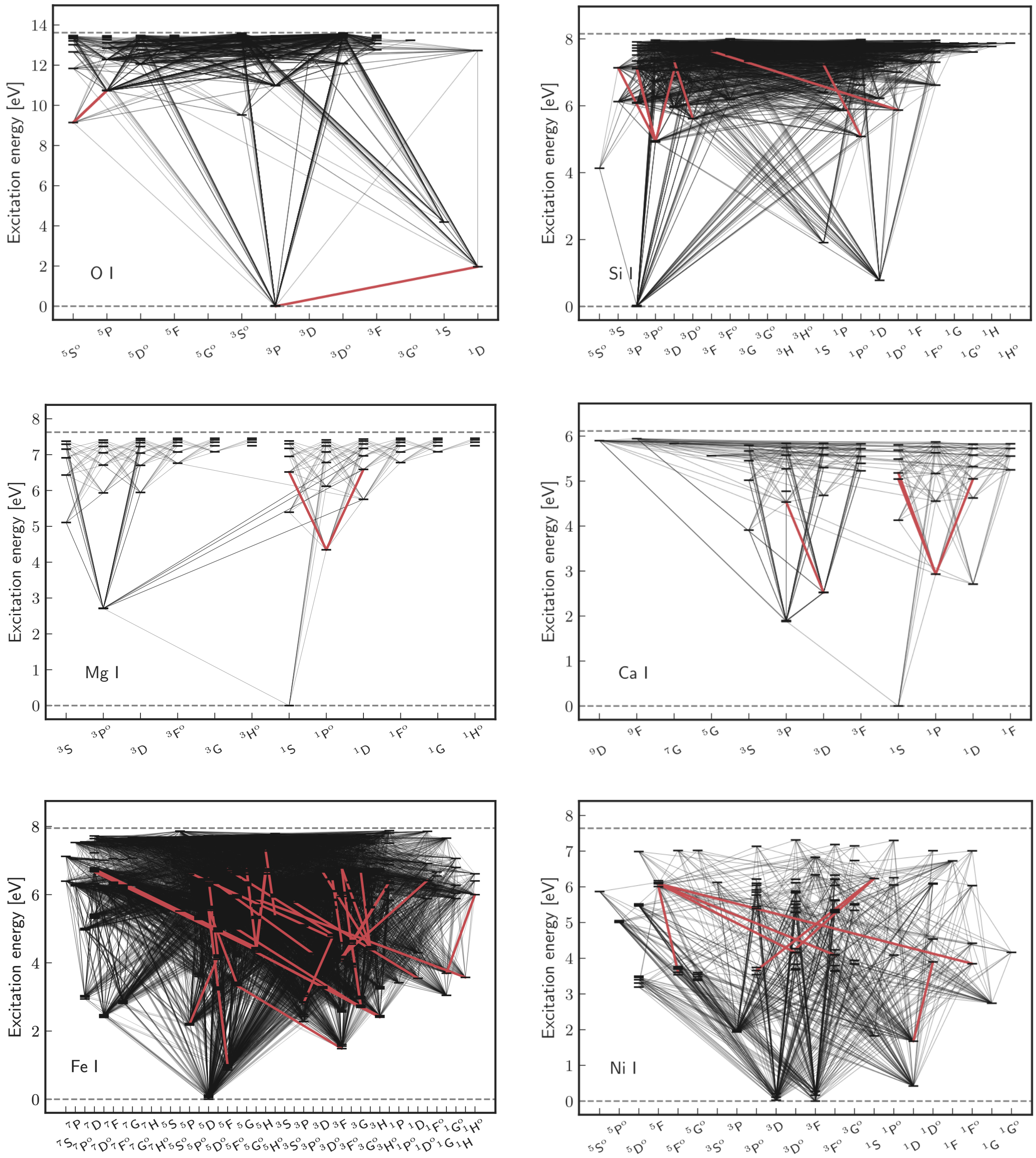

Figure 4.3: Grotrian diagrams for chemical elements treated in NLTE. Energy states are depicted with horizontal dashes and connecting bound-bound radiative transitions are shown with black lines. Red lines correspond to diagnostic transitions used in abundance analysis. Only energy levels following L-S coupling are shown.

induced transitions. Radiative data were adopted from the Kurucz[2] database, and supplemented with new photo-ionisation cross-sections for O I states computed using the R-matrix method (Berrington et al., 1995). This method was also used to derive new data for electron-impact transitions. H induced inelastic processes were computed using the OH molecule computed employing the multi-reference configuration interaction (MRCI) method and the collisional dynamics description presented by Belyaev et al. (2019). The model atom of Ni primarily relies on the same sources of radiative data (NIST[3], Kurucz), whereas collisional data were calculated using the standard formulae presented in (van Regemorter, 1962, Seaton, 1962, Drawin, 1968).

The Mg model atom is described in detail in Zhao et al. (1998) and in Mashonkina (2013), and it was slightly updated in Bergemann et al. (2017). The model includes 86 energy states, of which 85 represent Mg I, and it is closed by Mg II. Radiative transitions were adopted from the Opacity Project (The Opacity Project Team, 1995). 453 of these transitions connect the energy levels in Mg I and for 65 states bound-free transition were included. The collisional data were taken from Mauas et al. (1988) and Zhao et al. (1998) for $e^- + $ Mg collisions, and Barklem et al. (2012) was the main source for H I impact excitation and charge exchange processes. Electron-impact ionisation rate coefficients were computed using the Seaton (1962) formula.

The Fe model is described in detail in Bergemann et al. (2012b) and it was recently updated by Semenova et al. (2020). Fe I has probably the most complex system of energy levels of all species in the periodic table. Therefore, representing them in a model is a major numerical challenge. In the Kurucz database, over 37 000 energy levels and over 6 million transitions are available. The model we employ in this work contains 637 Fe I states and 58 Fe II states, which are connected via 19 267 radiative bound-bound transitions. Fine-structure levels of Fe I are included up to $\sim$7 eV. We also include very high-excitation energy levels of Fe I, using the super-levels and super-lines following Bergemann et al. (2012b). The uppermost energy state in Fe I (a super-level) is thus located at 7.88 eV, only 0.07 eV from the first ionisation threshold (7.95 eV) representing the ground state (term) of Fe II. We note that it is common to use fine structure levels for Fe II, however, all ionisation photo-ionisation cross-sections and charge transfer rates are defined for LS states (not for fine structure levels). We tested whether using the actual ionisation thresholds for Fe II levels or representing them as terms has an impact on our results, and found that the difference in abundance space was only 0.01 dex, that is negligible compared to other sources of error in the analysis. We note that the NIST database is very incomplete for the Fe I structure

---

[2] `http://kurucz.harvard.edu/`

[3] `https://physics.nist.gov`

above 7.5 eV. We therefore also tested more compact atomic models of Fe, devoid of energy levels higher than 7.50 eV in the Fe I system, and we found that using more compact models does not affect the abundances determined from Fe I lines by more than 0.01 dex.

Bound-free radiative cross-sections were taken from Bautista et al. (2017), whereas the rates of transitions caused by collisions with e^- and H atoms were computed using the new quantum-mechanical estimates of the cross-sections by Bautista et al. (2017) and Barklem (2018), respectively. The photo-ionisation cross-sections were tabulated in a fine energy grid, to resolve resonances. This is particularly important, because Fe I (and other Fe-group species) react very sensitively to the radiation field, and over-ionisation is indeed the main process behind non-negligible NLTE effects, especially at low metallicity (Bergemann & Nordlander, 2014, Amarsi et al., 2016).

The atomic model of Si is based on the model presented by Bergemann et al. (2013), however, with important updates to the radiative and collisional part of the atom. The f-values and damping constants for the Si I lines were substituted by the most recent data available in the Kurucz database[4]. The rate coefficients describing processes in inelastic collisions between Si I and H atoms were adopted from Belyaev et al. (2014) and from a database by Paul Barklem[5]. The rate coefficients describing the charge transfer and mutual neutralisation reactions were adopted from Belyaev et al. (2014).

4.2.5 New oscillator strengths for N and O

To compute the new values of oscillator strengths, we adopt different independent approaches.

For the O I lines, we used the pseudo-relativistic Hartree-Fock method, originally introduced by Cowan (1981) modified to account for core-polarization effects (HFR+CPOL), as described e.g. by Quinet et al. (1999) and Quinet et al. (2002) and the fully relativistic multiconfiguration Dirac-Hartree-Fock (MCDHF) approach developed by Grant (2007) and Froese Fischer et al. (2016) with the latest version of GRASP (General Relativistic Atomic Structure Program), known as GRASP2018 (Froese Fischer et al., 2019). In our HFR+CPOL calculations, the valence-valence interactions were considered among a set of configurations including $2p^4$, $2p^3\,nl$ (with nl up to 6h) and all single and double excitations from 2s, 2p to 3s, 3p, 3d orbitals while the core-valence correlations were modelled by a core-polarization potential corresponding to a He-like O VII ionic core with a dipole polarizability $\alpha_d = 0.0026\ a_0^3$ (Johnson et al., 1983) and a cut-off radius $r_c = 0.198\ a_0$. The latter value corresponds to the calculated HFR value of $<r>$ of the outermost core orbital

---

[4] `http://kurucz.harvard.edu/atoms/1400/`, based on Kurucz 2016 calculations

[5] `https://github.com/barklem`

Table 4.3: Comparison of $\log gf$-values for the O I transitions. See text.

Reference	Transition				
	777.1 nm	777.4 nm	777.5 nm	630.0 nm	$3s\,^5\mathrm{S^o}$ - $3p\,^5\mathrm{P}$
Hibbert et al. (1991)					
CIV3(L)[a]	0.371	0.225	0.003		0.702
CIV3(V)[a]	0.333	0.187	−0.035		0.664
Jönsson & Godefroid (2000)					
MCHF(L)[b]					0.682
MCHF(V)[b]					0.679
Civiš et al. (2018)					
QDT[c]	0.317	0.170	−0.051		0.647
Storey & Zeippen (2000)					
SST[d]				−9.72	
This work					
HFR+CPOL[e]	0.350	0.204	−0.018	−9.65	0.681
MCDHF(B)[f]	0.370	0.224	0.002		0.701
MCDHF(C)[f]	0.331	0.184	−0.039		0.662
MCDHF[f]				−9.69	
AST(L)[g]	0.348	0.199	−0.021		
AST(V)[g]	0.326	0.176	−0.043		
Final recommended					
	0.350	0.204	−0.019	−9.69	

---

[a] CIV3 calculations in the length (L) and velocity (V) gauges

[b] Non-relativistic multiconfiguration Hartree-Fock (MCHF) calculations in the length (L) and velocity (V) gauges

[c] Quantum Defect Theory (QDT)

[d] SUPERSTRUCTURE (SST) calculations

[e] Pseudo-relativistic Hartree-Fock method including core-polarization effects (HFR+CPOL)

[f] Fully relativistic multiconfiguration Dirac-Hartree-Fock (MCDHF) calculations in the Babushkin (B) and Coulomb (C) gauges

[g] AUTOSTRUCTURE (AST) calculations in the length (L) and velocity (V) gauges

(1s). For the MCDHF calculations, we adopted a physical model in which valence-valence correlations were considered by means of single and double excitations from the $2p^4$, $2p^33s$, $2p^33p$, $2p^33d$ multireference (MR) configurations to the {9s,9p,9d,6f,6g,6h} orbital active set (where the maximum orbital principal quantum number n_{max} is specified for each orbital azimuthal quantum number $l = s - h$) while the core-valence effects were included by means of single and double excitations from 1s to the active set of orbitals. The convergence of the oscillator strengths for the O I lines was verified by comparing the results obtained using physical models including increasingly large active sets of orbitals, and by observing a good agreement between the gf-values computed within the Babushkin (B) and the Coulomb (C) gauges. The two gauges tend to preferentially weight different parts of the wavefunctions (that is the outer region vs. near-nucleus), and so can be used to quantify the systematic effects.

We also performed large, exhaustive calculations of f-values for the diagnostic lines of O I and N I using the code AUTOSTRUCTURE (Badnell, 2011). We considered all one-, two-, and three-electron promotions from the 2s and 2p orbitals of configurations $2s^2 2p^4$ to excited orbitals nl, with $3 \leq n \leq 6$ and $0 \leq l \leq 4$. We analyzed the convergence or lack thereof of the oscillator strengths with increasingly large configuration expansions, which accounted for hundreds of configurations for each element. In every calculation we made use of term energy corrections and level energy corrections, which are semi-empirical corrections available in AUTOSTRUCTURE. Convergence of calculated oscillator strength values was evaluated by two criteria that are the stability of the numeric values as more configurations are accounted for in the configuration interaction expansion and the agreement between calculated length and velocity gauges of the oscillator strength.

Table 4.4: Solar photospheric abundances derived in NLTE. See the text for details.

El.	A(El), $\sigma_{\rm tot}$ 1D[a] NLTE	A(El), $\sigma_{\rm tot}$ $\langle$3D$\rangle$[b] NLTE [c]	$\Delta_{\rm STAGGER-CO5BOLD}$	$\sigma_{\rm stat}$
C	8.48 ± 0.08	8.56 ± 0.06	0.016	0.05
N	7.88 ± 0.12	7.98 ± 0.10	-0.011	0.1
O	8.74 ± 0.04	8.77 ± 0.04	0.014	0.02
Mg	7.45 ± 0.08	7.55 ± 0.06	0.020	0.06
Si	7.54 ± 0.07	7.59 ± 0.07	0.005	0.06
Ca	6.34 ± 0.05	6.37 ± 0.05	0.026	0.04
Fe	7.49 ± 0.08	7.51 ± 0.06	0.012	0.08
Ni	6.21 ± 0.04	6.24 ± 0.04	0.001	0.07

[a] 1D MARCS model atmosphere
[b] $\langle$3D$\rangle$ STAGGER model atmosphere
[c] LTE for C and N

The comparison of the f-values with the literature estimates is provided in Tab. 4.3. The values obtained with the MCDHF method and with AUTOSTRUCTURE agree to better than 1.5 % for the velocity gauges, and 5 % for the length gauges. Our results are also in a good agreement with the literature, including the values published by Hibbert et al. (1991) and by Jönsson & Godefroid (2000).

Our recommended values for the O I triplet lines are based on our new estimates calculated with both the MCDHF approach and AUTOSTRUCTURE. The final values of oscillator strengths are $\log gf = 0.350, 0.204$, and -0.019 dex for the 777.1, 777.4, and 777.5 nm transitions, respectively. These f-values are nearly identical to those adopted by Bergemann et al. (2021), with a difference of 1.6% only. The 630 nm line is an M1 transition and the transition operator is gauge independent. For this transition, our best value is the MCDHF result ($\log gf = -9.69$ dex), because it includes relativistic and electron correlation effects in more detail than the SST and HFR+CPOL calculations. The differences between different methods and between the two gauges are used to estimate the uncertainties of our f-values using the standard expression used in atomic physics $dT = |gf(\mathrm{B}) - \mathrm{gf(C)}|/\max(\mathrm{gf(B)}, \mathrm{gf(C)})$. It is important to note that there is no reason to prefer one gauge over the other. The convergences of the f-values in both of them demonstrate a similar behaviour. We therefore advocate to use the averages of results obtained in length and velocity form, or their relativistic equivalents.

4.2.6 Line lists

We make use of the line list compiled for the Gaia-ESO survey (GES) described in Heiter et al. (2021), which includes basic atomic data (wavelengths, energy levels, transition probabilities, broadening constants) and quality flags for lines relevant to FGK stars in the wavelength range from 475 to 685 nm and from 849 to 895 nm. The line list was assembled by a dedicated GES working group after a detailed assessment of all available sources of atomic and molecular data, with priority given to experimental data and carefully validated theoretical data. For a subset of atomic transitions tabulated in the line list a pair of flags is given for each transition that indicates the quality of the atomic data (primarily, $\log gf$) and the quality of the line in the stellar spectrum (primarily, blending). For each of these two aspects, the lines were sorted into three categories of decreasing quality, designated 'Y', 'U', and 'N'. The quality assessment was based on a comparison of synthetic and observed spectra for the Sun and Arcturus.

Since the GES line list only includes atomic data published until 2014, we updated the entries whenever more recent datasets have become available in the literature. The data and references for all the spectral lines used for the abundance calculations are given in Tables 4.1 and 4.2. For the diagnostic lines, van der Waals broadening parameters were adopted, where available, from Barklem et al. (2000). Also for the other lines in the linelist, we gave preference to the Anstee-Barklem-O'Mara theory (Anstee & O'Mara 1991 and successive expansions by P.S. Barklem and collaborators). Tables 4.1 and 4.2 give the values in a packed notation where the integer component is the broadening cross-section, σ, in atomic units, and the decimal component is the dimensionless velocity parameter, α. Values less than zero are the logarithm of the broadening width per unit perturber number density at 10 000 K in units of rad s^{-1} cm^3.

The oscillator strengths were adopted from the following sources. For CI, we used the new f-values from Li et al. (2021), which were computed by means of multiconfiguration Dirac-Hartree-Fock and relativistic configuration interaction methods. We note that for most transitions they are systematically lower compared to the commonly used values from Hibbert et al. (1993). For the MgI lines at 5528 Å and 5711 Å we used the experimental gf-values from Pehlivan Rhodin et al. (2017). For the CaI line at 6455.598 Å we updated the value in the GES line list to that recommended in Den Hartog et al. (2021). Also the other CaI lines that we used are included in the list of recommended lines by Den Hartog et al. (2021), and the uncertainties quoted in Table 4.1 are those recommended by Den Hartog et al. (2021)[6]. Most of the lines used for the abundance calculations that are also included in the GES line list have gf-value quality flag 'Y', except for a few Fe lines with flag 'U'. Concerning the blending quality flag, most lines have flag 'Y' or 'U', except for two NiI lines (at 4811.983 and 4814.598 Å) with flag 'N'. However, these two lines are clearly blended only in the spectrum of Arcturus, and much less so in the spectrum of the Sun.

For the wavelength ranges not covered by the GES line list, we used data from the VALD database[7] (Piskunov et al., 1995, Ryabchikova et al., 2015), and complemented them with molecular line lists provided by B. Plez (priv. comm.). It should be noted, though, that special care was taken to select only lines minimally affected by blends. Therefore the inclusion of molecules in the spectrum synthesis is strictly speaking not necessary, except for the modelling of NI lines, which are blended by CN features.

4.3 Model data comparison

Our results for all relevant chemical elements are collected in Table 4.4, and in Table 4.5 we provide the abundances of all species that are relevant to the SSM. To illustrate the quality of the spectral fits, we show selected examples of the best-fit spectra compared to

---

[6] These uncertainties refer to the absolute gf-values, while the uncertainties given in the GES line list are those of the relative measurements quoted in Smith & Raggett (1981) and Smith (1988).

[7] `http://vald.astro.uu.se`

the observed profiles in Fig. 4.4. Abundances measured from individual lines are presented in Table 4.7 in Appendix 4.5.

Table 4.5: Our recommended solar chemical abundances on the astronomical scale $A(i) = \log(N(i)/N_H) + 12$. Uncertainties listed for the meteoritic abundances are purely statistical but a systematic and fully correlated 0.02 dex uncertainty should be included for all elements (Sect. 4.3.3). The last row reports the total Z/X, where the abundances of volatile elements are always taken from the photospheric scale. For the meteoritic scale, the second uncertainty source reflects the fully correlated uncertainty from transforming the cosmochemical scale to the astronomical scale. See the text.

Element	A(El)$_{\text{ph}}$, σ_{tot}	Ref.[a]	A(El)$_{\text{met}}$, σ_{stat}
H	12.0	-	-
C	8.56 ± 0.05	1	-
N	7.98 ± 0.08	1	-
O	8.77 ± 0.04	1	-
F	4.40 ± 0.25	2	4.67 ± 0.09
Ne	8.15 ± 0.11	1	-
Na	6.29 ± 0.02	3	6.33 ± 0.04
Mg	7.55 ± 0.05	1	7.58 ± 0.02
Al	6.43 ± 0.03	4	6.48 ± 0.03
Si	7.59 ± 0.07	1	7.57 ± 0.02
P	5.41 ± 0.03	5	5.48 ± 0.03
S	7.16 ± 0.11	6	7.21 ± 0.03
Cl	$[5.25 \pm 0.12]$	7	5.29 ± 0.07
Ar	$[6.50 \pm 0.10]$	7	-
K	5.14 ± 0.10	3	5.12 ± 0.02
Ca	6.37 ± 0.04	1	6.32 ± 0.03
Sc	3.07 ± 0.04	3	3.09 ± 0.03
Ti	4.94 ± 0.05	8	4.96 ± 0.03
V	3.89 ± 0.08	9	4.01 ± 0.03
Cr	5.74 ± 0.05	10	5.69 ± 0.02
Mn	5.52 ± 0.04	11	5.53 ± 0.03
Fe	7.50 ± 0.06	1	7.51 ± 0.02
Co	4.95 ± 0.04	12	4.92 ± 0.02
Ni	6.24 ± 0.04	1	6.25 ± 0.03
Z/X	0.0225 ± 0.0014		$0.0226 \pm 0.0014 \pm 0.0003$

[a] References: (1) this work (2) Maiorca et al. (2014) (3) Zhao et al. (2016) (4) Nordlander & Lind (2017) (5) Scott et al. (2015b) (6) Caffau et al. (2011) (7) Lodders (2019) (8) Bergemann (2011) (9) Scott et al. (2015a) (10) Bergemann & Cescutti (2010) (11) Bergemann et al. (2019) (12) Bergemann et al. (2010)

The uncertainties of the abundances were derived in analogy to Bergemann et al. (2021). We form uniform distributions of errors using the values representing a) the uncertainty of

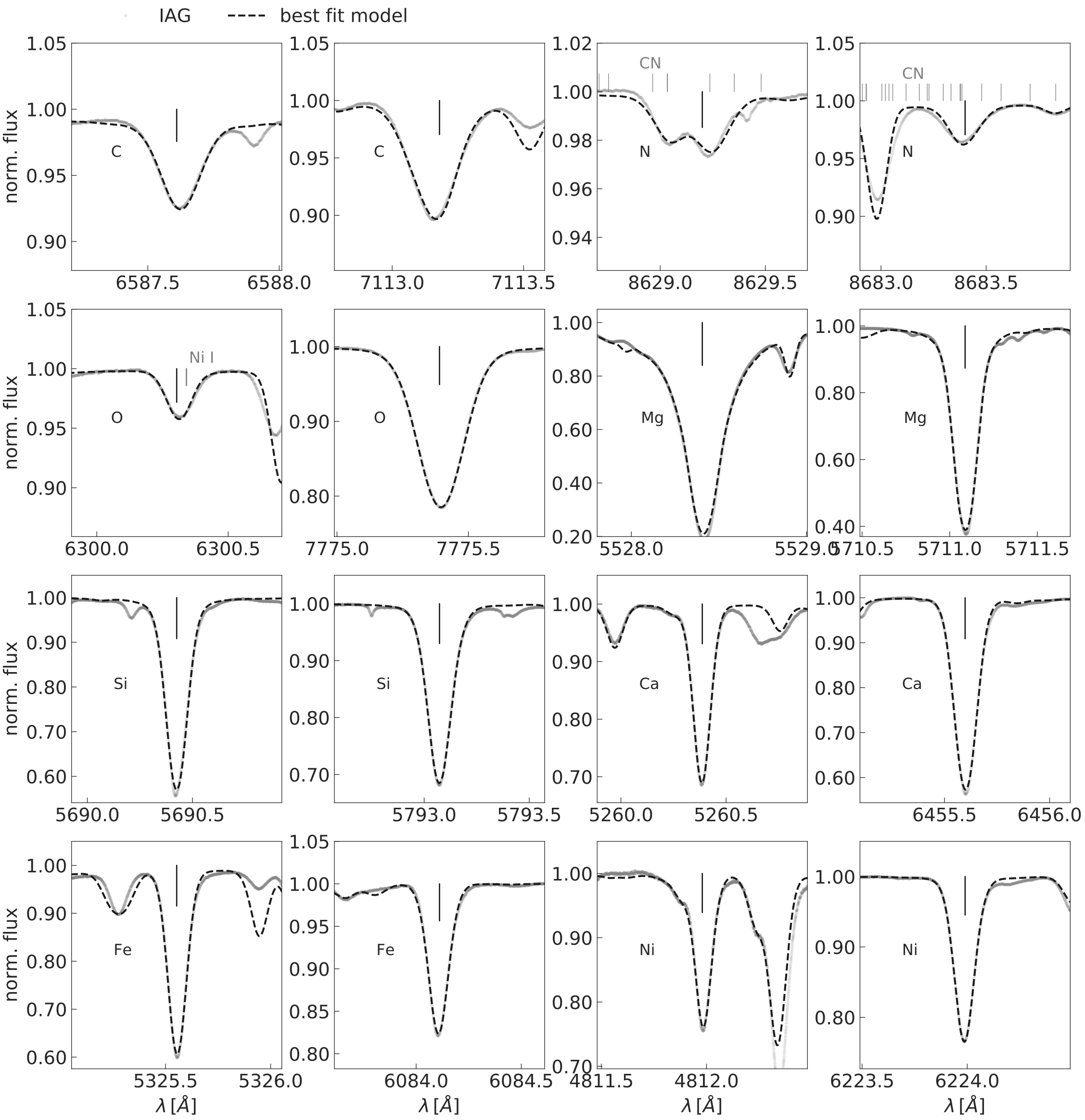

Figure 4.4: Comparison of model and observed line profiles for some of the diagnostic lines.

the transition probability (f-value), b) the systematic uncertainty caused by using different ⟨3D⟩ models, c) the uncertainty caused by the H collisional data (only for elements treated in NLTE), and d) the statistical uncertainty. The latter is represented by the scatter of abundances derived from individual spectral lines of the same chemical element and is stated in the last column of Table 4.4. The uncertainty caused by using different ⟨3D⟩ models is represented by the difference between the abundances derived with ⟨3D⟩ STAGGER and

CO5BOLD models, see fourth column of Table 4.4. The error distributions are then co-added, as the uncertainties are independent. Since the shapes of the distributions are close to Gaussian, we adopt the simple averages and the standard deviations (1σ) of the resulting combined distributions as our final abundances and their corresponding uncertainties, respectively.

4.3.1 New estimates of photospheric abundances

C

Our analysis of the C abundance relies on atomic C lines, because these are the features we expect to be able to measure in the spectra of upcoming facilities, such as 4MOST and WEAVE. Since the diagnostic lines of C I are almost insensitive to NLTE (see below), we rely on $\langle$3D$\rangle$ LTE calculations to obtain the solar C abundance of A(C) $= 8.56 \pm 0.06$ dex. For comparison, the values obtained by Amarsi et al. (2019) and Caffau et al. (2010) are 8.44 ± 0.02 dex and 8.50 ± 0.06 dex, respectively, the latter in agreement with our work. Also, the revised 3D NLTE abundance by Li et al. (2021) is 8.50 ± 0.07 dex, which is consistent with our value. We note that using the new f-values calculated by Li et al. (2021), we obtain a significantly improved agreement between different C I lines, compared to the result obtained using the older f-values from Hibbert et al. (1993). The line-by-line scatter drops from 0.08 dex (with Hibbert et al. 1993 values) to 0.05 dex (with Li et al. 2021 values). Especially, the much lower $\log gf$ for the 7113.18 Å line found by the latter study is essential to bring line into agreement with the other optical lines of C I. This result suggests that the new f-values from Li et al. (2021) are more reliable than the older values from Hibbert et al. 1993.

Another estimate of the solar C abundance was recently presented by Alexeeva & Mashonkina (2015), who obtained (in 3D) A(C) $= 8.43 \pm 0.02$ dex from the analysis of the CH lines, A(C) $= 8.46 \pm 0.02$ dex from the C_2 lines, A(C) $= 8.43 \pm 0.03$ dex from the C I permitted lines, and A(C) $= 8.45$ dex from the forbidden [C I] feature. However, these estimates rely on older Hibbert et al. (1993) data, and after re-normalisation to the Li et al. (2021) f-values[8] their abundance is in excellent agreement with our result. Our analysis of C abundances is carried out in LTE, however, according to 3D NLTE calculations by Amarsi et al. (2019, their Table 2), 3D NLTE and 3D LTE abundances based on our diagnostic lines of C I agree within 0.01 dex.

Our estimate of the C abundance obtained using the CO5BOLD model is less than 0.02

---

[8] The values from Li et al. (2021) are typically 0.05 dex to 0.16 dex lower for the diagnostic optical lines of C I. Hence, the C abundance is correspondingly higher.

dex lower compared to that calculated using the STAGGER model. This suggests that the difference between Caffau et al. (2010) and Amarsi et al. (2019) is likely not caused by the differences between the two 3D solar model atmospheres. The value provided by Asplund et al. (2021) is A(C) $= 8.46 \pm 0.04$ dex, somewhat higher compared to the previous estimate by Asplund et al. (2009).

N

Our estimate of the N abundance relies on the modelling of the two least-blended N I lines in the solar spectrum. For the lack of an NLTE model of N, we resort to the LTE analysis. The recent study by Amarsi et al. (2020a) suggests that the difference between 1D LTE and $\langle 3D \rangle$ NLTE abundances for the optical N I lines are extremely small, and does not exceed 0.005 dex. In this work, we employ the new f-values calculated as described in Sect. 4.2.5. Our recommended value of the solar N abundance thus becomes A(N) $= 7.98 \pm 0.10$ dex. The study by Amarsi et al. (2020a) advocated for the solar N abundance of A(N) $= 7.77 \pm 0.05$ dex, while Asplund et al. (2021) derived N abundance based on both atomic and molecular lines, A(N) $= 7.83 \pm 0.07$, with a value unchanged from that of Asplund et al. (2009), where A(N) $= 7.83 \pm 0.05$ dex. We note, however, that the N abundance has a very minor impact on the overall metallicity, see Sect. 4.4.1 and Fig. 4.7.

In the choice of the solar N value, it is important to stress that in this work we rely on ab-initio atomic and molecular data, and we do not apply any empirical adjustment to the line lists. In particular, all molecular features are included self-consistently in the radiative transfer and spectrum synthesis calculations. In contrast, the solar N abundance provided by Amarsi et al. (2020a) is based on re-scaling the strengths of the CN blends in a semi-empirical approach, by estimating their equivalent widths in the solar disc-center spectrum through a comparison with nearby CN lines. Whereas both approaches have their pro's and contra's, the main value of our strictly theoretical approach is that it is universal and can be applied to any star, not biasing the result by the assumed value of the observed disc-center equivalent widths of the CN blends. We find that abundance obtained using the CO5BOLD model is only 0.011 dex higher compared to that calculated using the STAGGER model.

O

Our result for O, A(O) $= 8.77 \pm 0.04$ dex, is in excellent agreement with the full 3D NLTE analysis by Bergemann et al. (2021, 8.75 ± 0.03 dex). The difference between the two results, which is not significant, is caused by using the flux spectrum and the average $\langle 3D \rangle$ atmosphere model in this work.

Our O abundance is also consistent with the value by Caffau et al. (2008, 8.76 ± 0.07 dex), but it is somewhat higher compared to the estimate by Asplund et al. (2021, 8.69 ± 0.04 dex) and Amarsi et al. (2021, 8.70 ± 0.04 dex). These differences can be attributed to the use of new $\log gf$ values for the O lines, new observational material, and our first self-consistent NLTE radiative transfer for both O and Ni features, which is important for the critical diagnostic [O I] feature at 630 nm. As investigated in Bergemann et al. (2021) in detail, quantitatively, the break-down of systematic difference with Asplund et al. (2021) is as follows. Our new f-values lead to +0.02 dex higher abundances for the 777 nm lines, but −0.03 dex lower values for the 630 nm [O I] line. The IAG data further lead to a $+\sim 0.02$ higher abundance for the 777 nm and +0.03 dex higher values compared to the SST data, the SST data are however affected by the problem of fringing (Sect. 4.4 in Bergemann et al. (2021)). Modelling Ni in NLTE leads to a ~ 0.03 dex higher O abundance inferred from the [O + Ni] feature at 630 nm. There are also very minor differences caused by the continuum placement, model atmospheres, and resolution in radiative transfer modelling. Our results (Table 4.7 for the 630 nm and 777 nm lines are in excellent agreement.

Overall, our new O abundance is closer to the classical values from Grevesse & Sauval (1998) than the previous estimate by Asplund et al. (2021). We also note that according to Caffau et al. (2013), there is still an unresolved mismatch between the 630 nm and 636 nm [O I] lines, with the latter line yielding an the O abundance of 8.78 ± 0.02 dex.

To estimate the difference between the STAGGER and CO5BOLD models, we have furthermore performed a comparative analysis of the results obtained with both simulations. We find that the CO5BOLD model leads to a 0.006 dex lower abundance for the 630 nm forbidden line, and to 0.015 dex lower abundance for the permitted 777 nm O I triplet. This difference is not significant enough to explain the differences between the Caffau et al. (2008) and Asplund et al. (2009) results.

MG

Our estimate of the solar photospheric abundance of Mg is A(Mg) = 7.55 ± 0.06 dex. Comparing with the value obtained by Bergemann et al. (2017), 7.56 ± 0.05 dex, we find a very good agreement. Our results also support the recent detailed analysis of Mg in NLTE by Alexeeva et al. (2018), who find A(Mg)= 7.54 ± 0.11 dex based on Mg I and A(Mg)= 7.59 ± 0.05 dex based on Mg II lines. The comparison of abundances obtained from the CO5BOLD and STAGGER ⟨3D⟩ models (Table 4.4) suggests that the atomic Mg lines used in this work (at 5528 and 5711 Å) are not sensitive to the differences between the ⟨3D⟩ model atmospheres, with the difference in abundance not exceeding 0.02 dex.

The main uncertainty in the analysis of Mg abundances is still associated with the errors of the oscillator strengths and damping parameters. For comparison, the ⟨3D⟩ NLTE solar Mg abundance from Osorio et al. (2015) is considerably higher, 7.66 ± 0.07 dex. The offset could possibly be explained by the differences in the model atom, adopted atomic data, and the choice of lines in the calculations. Osorio et al. (2015) find significant (+0.05 to +0.15 dex) differences between the Mg abundances derived from the Mg I lines using the 1D and ⟨3D⟩ solar model atmospheres. This is confirmed by our analysis.

SI

The Si abundance is a very important parameter in the analysis, as the element has traditionally been used as the main anchor between the solar photospheric and the meteoritic abundance scales (Lodders, 2003, Asplund et al., 2009, Lodders, 2019). Our ⟨3D⟩ NLTE value, $\mathrm{A(Si)} = 7.59 \pm 0.07$ dex is slightly higher compared to the recent 3D NLTE estimate by Amarsi & Asplund (2017) and more recently by Asplund et al. (2021).

For the Si I lines, the NLTE effects are negative, such that NLTE abundances are lower compared to LTE values (Shi et al., 2008, Bergemann et al., 2013, Mashonkina, 2020), which is also supported by our new results. Our NLTE abundances for all lines in the list are $\sim$ 0.03 to 0.05 dex lower compared to LTE. The most recent NLTE estimate of the solar Si abundance, based on the NLTE line-by-line spectrum synthesis, was presented in Mashonkina (2020). They find that NLTE abundances obtained from the solar Si I lines are on average 0.02 to 0.1 dex lower compared to LTE (their Table 2), fully in agreement with our findings. Using their results for the lines in common with our study and re-normalising them to employed in this study f-values, their A(Si) becomes 7.55 dex, fully in agreement with our 1D NLTE estimate. In fact, their solar Si abundance using their preferred f-values would be 7.60 dex for the lines in common between our and their study, thus about 0.1 dex higher compared to Asplund et al. (2021).

Si I lines are similar to Mg I in that the lines are barely affected by the detailed structure of the 3D model atmosphere. The difference between the results based on CO5BOLD and STAGGER does not exceed 0.005 dex.

CA

The solar photospheric abundance of Ca is robust, as our ⟨3D⟩ NLTE calculations show an excellent consistency between different diagnostic lines of Ca I. Our recommended value is $\mathrm{A(Ca)} = 6.37 \pm 0.05$ dex. This value is slightly higher compared to the recommended value from Asplund et al. (2021, 6.30 ± 0.03 dex).

Other recent estimates of the solar Ca abundances were presented by Mashonkina et al. (2017) and Osorio et al. (2019). Mashonkina et al. (2017), performed a 1D NLTE analysis with the solar MARCS model, which resulted in solar abundances of A(Ca) $= 6.33 \pm 0.06$ dex based on Ca I lines and A(Ca) $= 6.40 \pm 0.05$ dex based on Ca II lines with high values of $E_{\rm low}$. The average of these quantities is consistent with our $\langle$3D$\rangle$ NLTE estimate, which is not surprising as their NLTE model atom and the chosen line list are similar to our inputs.

Osorio et al. (2019) also used 1D hydrostatic models in combination with NLTE line formation. However, their solar abundances show a significant scatter, ranging from A(Ca) = 6.0 dex to 6.45 dex, which likely results from the choice of lines in their analysis.

Fe

Our results for the solar Fe abundance are close the recent literature estimates. In $\langle$3D$\rangle$ NLTE, we obtain A(Fe) $= 7.51 \pm 0.06$ dex, which represents the combination of the abundance determined from the Fe I and Fe II lines. The abundances derived from the lines of the neutral species are sensitive to NLTE, which is also known from literature studies (e.g. Bergemann et al., 2012b, Lind et al., 2012). However, the majority of diagnostic lines in our line list have $E_{\rm low} \gtrsim 2.5$ eV, therefore the difference with the LTE abundance is not large and does not exceed 0.1 dex for the majority of Fe I lines. We do not include Fe I lines with low $E_{\rm low}$ values in the abundance analysis, due to their high sensitivity to the choice of model atmosphere, see Sect. 4.2.2. However, this choice of Fe lines affects the final Fe abundance by no more than 0.01 dex. Likewise, the abundance differences obtained from the CO5BOLD and STAGGER models do not exceed 0.012 dex.

Comparing our result with the recent estimates by two different groups, Lind et al. (2017, 7.48 ± 0.04 dex) and Mashonkina et al. (2019, 7.54 dex), we find a good agreement with both studies. The latter estimate is based on the analysis of Fe II lines using the solar MARCS model atmosphere and the f-values from Raassen & Uylings (1998), whereas the former relies on 3D NLTE modelling of the lines of both ionisation species. Also the careful systematic analysis of Fe lines in NLTE by Sitnova et al. (2015) supports our result, although they relied on the Drawin formula to describe Fe+H collisions instead of quantum-mechanical data.

Our solar Fe abundance is also fully consistent with the earlier estimate by Caffau et al. (2007), who found A(Fe)$= 7.52 \pm 0.06$ dex, they also suggest that the result is not sensitive to the choice of f-values. The value from Asplund et al. (2021, 7.46 ± 0.04 dex) is, in contrast, significantly lower compared to our values, to Caffau et al. (2007), and to Mashonkina et al. (2019).

Ni

This work presents the first detailed analysis of the solar photospheric abundance of Ni using ⟨3D⟩ NLTE calculations. Our best estimate is A(Ni) = 6.24 ± 0.04 dex, and it is based on the detailed modelling of 11 lines of Ni I and one line of Ni II using the f-values from Wood et al. (2014).

We do not detect any systematic trend with the excitation potential of the lower energy level or other atomic parameters, which provides confidence in the results. The NLTE effects in the diagnostic solar Ni lines are modest: for the Sun, the differences between 1D NLTE and 1D LTE results are of the order 0.01 dex. However, as shown in Scott et al. (2015a) and in Bergemann et al. (2021), the lines of Ni are sensitive to the temperature structure of the model, and the calculations with models based on 3D RHD simulations yield somewhat higher Ni abundance in LTE and NLTE.

We also find that Ni lines are not very sensitive to the structure of the ⟨3D⟩ model atmospheres. The abundances derived with STAGGER model are within 0.02 dex different from the abundances derived using temporarily spaced CO5BOLD snapshots. However, these differences average out when combining results from individual CO5BOLD snapshots. So the final difference between STAGGER and CO5BOLD is negligible, below 0.001 dex.

4.3.2 Other chemical elements

Ne, Cl, Ar

The analysis of the Ne abundance is beyond the scope of this paper, because the abundance of the element cannot be determined from the solar photospheric spectrum. It is common (e.g. Lodders, 2019) to determine the solar Ne abundance from the Ne/O ratio that can be established independently and by assuming the ratio is the same in the solar photosphere, the absolute Ne abundance is derived.

This procedure was adopted, e.g, by Lodders (2003) to derive the Ne abundance by combining the Ne/O ratio measured in young B type stars and He II regions (Meyer, 1989), in solar active regions (Widing, 1997), and in solar energetic particle events (Reames, 1998) with the photospheric O abundances. Using the Ne/O ratio from Lodders (2003) (Ne/O = 0.152), and adopting our O abundance, we would obtain A(Ne) = 7.95 ± 0.1 dex. This value is consistent with that by Bochsler (2007), who obtained the Ne abundance by combining the solar wind data from the APOLLO foil experiment (Geiss et al., 1972) with a model for the Coulomb-drag fractionation in the solar wind. Juett et al. (2006) determined the Ne/O ratio in the interstellar medium (ISM, 0.185) from the K- and L-shell spectroscopy of nine X-ray binaries. Whether the solar values and the ISM values are consistent is still debated, as the latter is, in particular, prone to systematic effects, such as the choice of the model describing the ionization structure of the Local Bubble (e.g. Breitschwerdt & de Avillez, 2021). The recent analysis of the local ISM data acquired with the IBEX satellite by Park et al. (2014) indicates a significantly higher Ne/O value of 0.33. This estimate supports the earlier values based on ISM data collected with the SWICS spectrometer on Ulysses (Ne/O = 0.26 dex, Gloeckler & Fisk 2007, their Table 3, estimated based on total densities of Ne and O in the local interstellar cloud). It is also consistent with the estimate based on the analysis of *Chandra* X-ray spectra (Ne X, O VIII, OVII) of nearby FGK-type main-sequence stars by Drake & Testa (2005, 0.41). Furthermore, a recent NLTE analysis of 24 B-type stars by Alexeeva et al. (2020) finds non-negligible differences with Ne abundances presented by Meyer (1989).

In the most recent analysis of the SOHO data with new atomic data, Young (2018) found a Ne/O ratio of 0.24 ± 0.05 dex. Using their value, we obtain A(Ne)= 8.15 dex, which is higher than the estimate calculated using the Ne/O fraction from Lodders (2003). In the light of remaining uncertainties associated with the ISM and B-type diagnostics, we have opted for determining our final Ne abundance using the Young (2018) Ne/O ratio, which is based on the SOHO measurements of emission lines from the transition region of the quiet Sun. That value is about 40 % higher compared to an earlier estimate by the same author (Young, 2005), because of the use of more accurate ionization and recombination rate coefficients. We adopt a more conservative error to reflect the uncertainty associated with the latter, as well as the uncertainty of our photospheric O abundance. Our recommended abundance is, thus, A(Ne) $= 8.15 \pm 0.11$ dex. The value is consistent with the estimate by Young (2018), A(Ne) $= 8.08 \pm 0.09$ dex and 8.15 ± 0.10 dex, employing the O values from Asplund et al. (2021) and Caffau et al. (2011), respectively.

For Cl and Ar we adopt the values from Lodders (2019). These elements do not play any significant role in the calculation of the SSM, however, we include them for completeness.

F, NA, K, P, AL, S

We do not redetermine the abundance of these elements in this work, but rely on recent literature values, giving preference to the values that are most consistent with our methodological approach.

The solar abundance of F is taken from the analysis by Maiorca et al. (2014). To the best of our knowledge, no NLTE analysis of F has been performed to date.

For both Na and K, we adopt the estimates from Zhao et al. (2016). They determined the Na abundance in NLTE using six Na I lines and the model atom from Gehren et al. (2004). The error of the Na value adopted for this study was calculated from the line-to-line scatter (presented in Table 2 in Zhao et al. 2016). The study by Scott et al. (2015b) advocated a solar Na abundance of 6.21 ± 0.04 dex.

The abundance of K determined by Zhao et al. (2016) and adopted for this study was based on the NLTE model presented in Zhang et al. (2006). Another NLTE estimate of the solar K abundance by Reggiani et al. (2019), $\mathrm{A(K)} = 5.11$ dex, is fully consistent with that of Zhao et al. (2016).We adopt a conservative uncertainty of A(K) to be 0.1 dex, as neither Zhao et al. (2016) nor Reggiani et al. (2019) provide an uncertainty on their K abundance estimate.

The abundance of P was taken from Scott et al. (2015b) and it is based on LTE, for the lack of NLTE calculations. The value of the Al abundance is taken from the 3D NLTE analysis by Nordlander & Lind (2017).

For S, we adopt the value by Caffau et al. (2007), $\mathrm{A(S)} = 7.16 \pm 0.11$ dex. Their estimate is based on the detailed analysis of several S I lines in the optical and near-IR solar spectrum using the CO5BOLD model atmosphere using NLTE abundance corrections from Takeda et al. (2005). Also the NLTE analyses by Korotin (2009) and Korotin et al. (2017) suggest significant deviations from LTE for the majority of S I lines. Another recent estimate of the solar photospheric S abundance was proposed by Asplund et al. (2021), and it is slightly lower ($\mathrm{A(S)} = 7.12 \pm 0.03$ dex) compared to our adopted value.

FE-PEAK ELEMENTS

For Sc, we refer to the estimate provided by Zhao et al. (2016) using a set of Sc II lines modelled in NLTE with full account for hyperfine splitting (HFS). This estimate is preferred over other values, which were carried out in LTE (e.g. Lawler et al., 2019, Asplund et al., 2021). It shall be noted that both Sc I and Sc II show significant departures from LTE, therefore especially the Sc II-based abundances are typically overestimated (Zhao et al., 2016). Our Sc value is in excellent agreement with the meteoritic abundance.

The solar abundances of Ti, Cr, and Co were adopted from Bergemann (2011), Bergemann & Cescutti (2010), and Bergemann et al. (2010), respectively. All these estimates are based on detailed NLTE modelling, with account for HFS for Co lines and isotopic shifts for Ti.

Our value of the Mn abundance ($\mathrm{A(Mn)} = 5.52 \pm 0.04$ dex) was taken from the detailed analysis in Bergemann et al. (2019). This estimate is based on full 3D NLTE radiative transfer calculations of 13 Mn I lines, using the same 3D STAGGER model atmosphere as employed in this work. Bergemann et al. (2019) showed that taking into account 3D NLTE effects is essential to obtain reliable excitation-ionisation balance for Mn in atmospheric conditions of late-type stars.

4.3.3 Meteoritic abundance scale

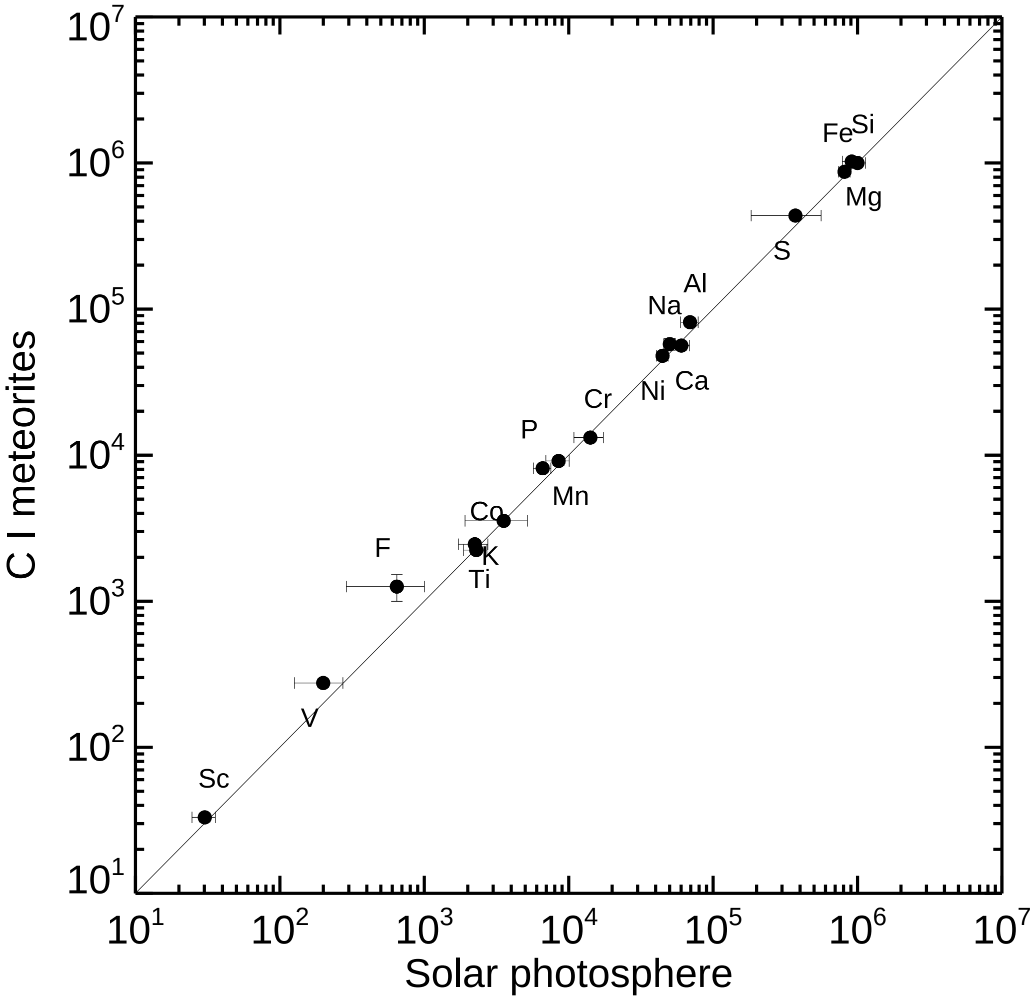

Figure 4.5: Comparison of the photospheric estimates with meteoritic values.

CI-chondrites are a well known source to measure primitive solar system abundances of refractory elements (Lodders, 2003, 2021). Meteoritic measurements have been historically more robust than photospheric determinations and the level of agreement between meteoritic and photospheric abundances has been used as a gauge of the quality of the latter. Bringing the meteoritic abundances to the photospheric scale requires defining an anchor point. Often, the Si abundance has been used for this purpose (Grevesse & Sauval, 1998, Lodders, 2003, Asplund et al., 2021), but groups of elements have also been used (Anders & Grevesse, 1989, Palme et al., 2014).

Regardless of the methodology, meteoritic abundances converted to the photospheric scale have two uncertainty terms. The first one is the intrinsic error associated with the process of the abundance measurement that can be assumed uncorrelated among different elements. The second one is the systematic error associated with the transformation and it is a fully correlated error among all chemical elements. As a result, these two error sources cannot be quadratically added. This error source when meteoritic abundances are used for calculation of solar (stellar) models has been traditionally ignored and, unfortunately, can be equal or even larger than the measurement error. Our goal below is to obtain meteoritic solar abundances for which the systematic component of the error is minimized, i.e. the anchor point is defined more robustly.

To this end, we adopt the CI-chondrite abundances from Lodders (2021) in the cosmochemical scale, defined such that the Si abundance is $N(\mathrm{Si}) = 10^6$. In order to derive meteoritic abundances in the astronomical scale we introduce a scale factor c. We determine the latter by minimizing the quadratic difference between the photospheric and meteoritic scales using the set of five refractory elements that have been newly derived in this work, constructed as

$$\chi^2 = \sum_i \frac{[A(i)_{\mathrm{ph}} - (\log N_i + c)]^2}{\sigma^2_{\mathrm{i,ph}} + \sigma^2_{\mathrm{i,me}}}, \tag{4.1}$$

where the sum extends over Mg, Si, Ca, Fe, and Ni. We obtain an excellent agreement between the two scales, yielding a total $\chi^2_{\mathrm{min}} = 1.27$, for $c = 1.57 \pm 0.02$[9]. The uncertainty in c is determined by the range over which $\Delta\chi^2 = 1$ around the minimum. It represents the systematic uncertainty associated to the meteoritic scale that should be included for all elements and is, in addition, a fully correlated error source among them. For comparison, Lodders (2003) obtained $c = 1.54$ using only Si, but did not include an estimate of the systematic error. The final meteoritic abundances transformed to the solar photospheric abundance scale and the associated measurement errors are listed in Table 4.5. The systematic and fully correlated 0.02 dex error is not included in the table but should always be taken into consideration when assessing the uncertainties due to chemical composition uncertainties in solar and stellar models.

Our final estimate of the solar Z/X ratio is 0.0225, if calculated using the photospheric

---

[9] Before rounding off, the result is $c = 1.567 \pm 0.023$.

abundances only, and 0.0226, if the meteoritic abundances are used for most species, except C,N, and O, for which the photospheric values are used. Our Z/X ratio is 26% higher compared to Asplund et al. (2009), $Z/X = 0.0181$. It very close (within 1%) to the photospheric and meteoritic estimates by Grevesse & Sauval (1998), $Z/X = 0.0231$ and 0.0229) respectively, although the internal distribution of metals, i.e. the mixture, is different. And it is almost 10% higher than the estimate by Caffau et al. (2011), $Z/X = 0.0209$.

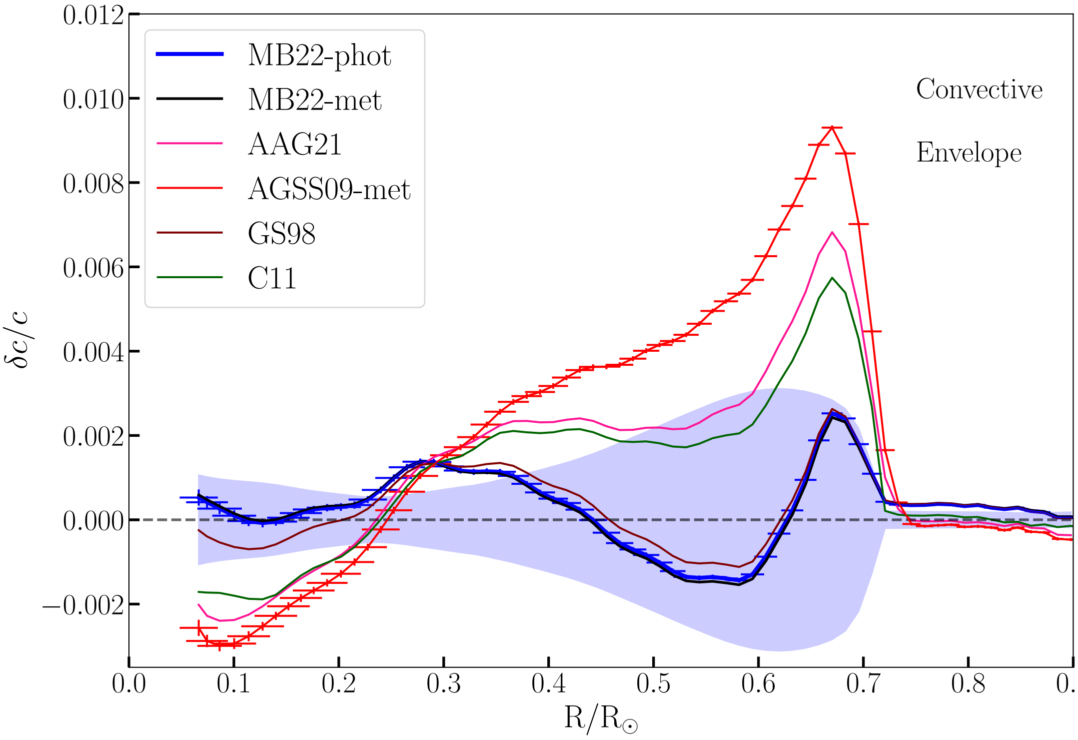

Figure 4.6: The sound speed profiles of the SSM computed using different solar chemical mixtures, Caffau et al. (2011, C11), Asplund et al. (2009, AGSS09-met), Grevesse & Sauval (1998, GS98), Asplund et al. (2021, AAG21), and this work (MB22-phot and MB22-met, see Sect. 4.3.3 for details.). The shaded blue area represents the solar model uncertainties arising from the inputs to the model, see Villante et al. (2014) for details. Error bars in AGSS09-met and MB22-phot lines denote fractional sound speed uncertainties arising from helioseismic data (y-axis) and width of inversion kernels (x-axis).

4.4 SUMMARY

4.4.1 STANDARD SOLAR MODELS

The choice of the solar chemical mixture has a direct impact on SSMs because they are calibrated to reproduce the adopted photospheric chemical mixture at the present-day solar age. In this way, the abundance of metals in the interior of SSMs is determined by the photospheric abundances. Metals are main contributors to the radiative opacity in the solar interior which, in turn, determines the mechanical and thermal structure of the model.

A widely used diagnostic for the quality of SSMs is the comparison of the sound speed profile of the model against the solar profile as inferred from helioseismic techniques. The deficiency of SSMs calibrated on solar mixtures based on results from Asplund (2005), Asplund et al. (2009), and the much better results for SSMs based on the solar mixtures by Grevesse & Noels (1993), Grevesse & Sauval (1998) are well documented (Bahcall et al., 2005, Basu & Antia, 2008, Serenelli et al., 2009, Pinsonneault & Delahaye, 2009, Serenelli et al., 2011, Buldgen et al., 2019). The solar mixture by Caffau et al. (2011) slightly improves the comparison, owing to overall higher (10 to 30%, depending on the element) abundances of CNO with respect to Asplund et al. (2009) and, to a minor extent larger abundances of refractories.

Table 4.6: Main characteristics of SSMs used in this work: depth of convective envelope ($R_{\rm CZ}$), surface helium mass fraction ($Y_{\rm S}$, fractional sound speed rms $\langle \delta c/c \rangle$ and initial helium $Y_{\rm ini}$ and metal $Z_{\rm ini}$ mass fractions.

Model	$R_{\rm CZ}/{\rm R}_\odot$	$Y_{\rm S}$	$\langle \delta c/c \rangle$	$Y_{\rm ini}$	$Z_{\rm ini}$
MB22-phot	0.7123	0.2439	0.0010	0.2734	0.0176
MB22-met	0.7120	0.2442	0.0010	0.2737	0.0178
AAG21	0.7197	0.2343	0.0027	0.2638	0.0155
AGSS09-met	0.7231	0.2316	0.0041	0.2614	0.0149
GS98	0.7122	0.2425	0.0010	0.2718	0.0187
C11	0.7162	0.2366	0.0021	0.2658	0.0169

Here, we have computed new SSMs using the `GARSTEC` code (Weiss & Schlattl, 2008), based on the photospheric and meteoritic solar mixtures provided in Table 4.6 (MB22-phot and MB22-met models respectively). The physics included in the models is the same as in Vinyoles et al. (2017). Atomic opacities have been computed for both flavors of MB22 solar mixtures, using OPCD 3.3 routines (Badnell et al., 2005). Opacities at low temperatures are most sensitive to the chemical composition thus we computed those using the revised MB22 mixture as described in Ferguson et al. (2005).

New helioseismic inversions of the solar sound speed have been performed for all the SSMs used in this work based on the methodology described in Basu et al. (2009) and references therein using the helioseismic data described in Basu (2021). The fractional sound speed differences are shown in Fig. 4.6. For comparison, we overplot the new inversion results

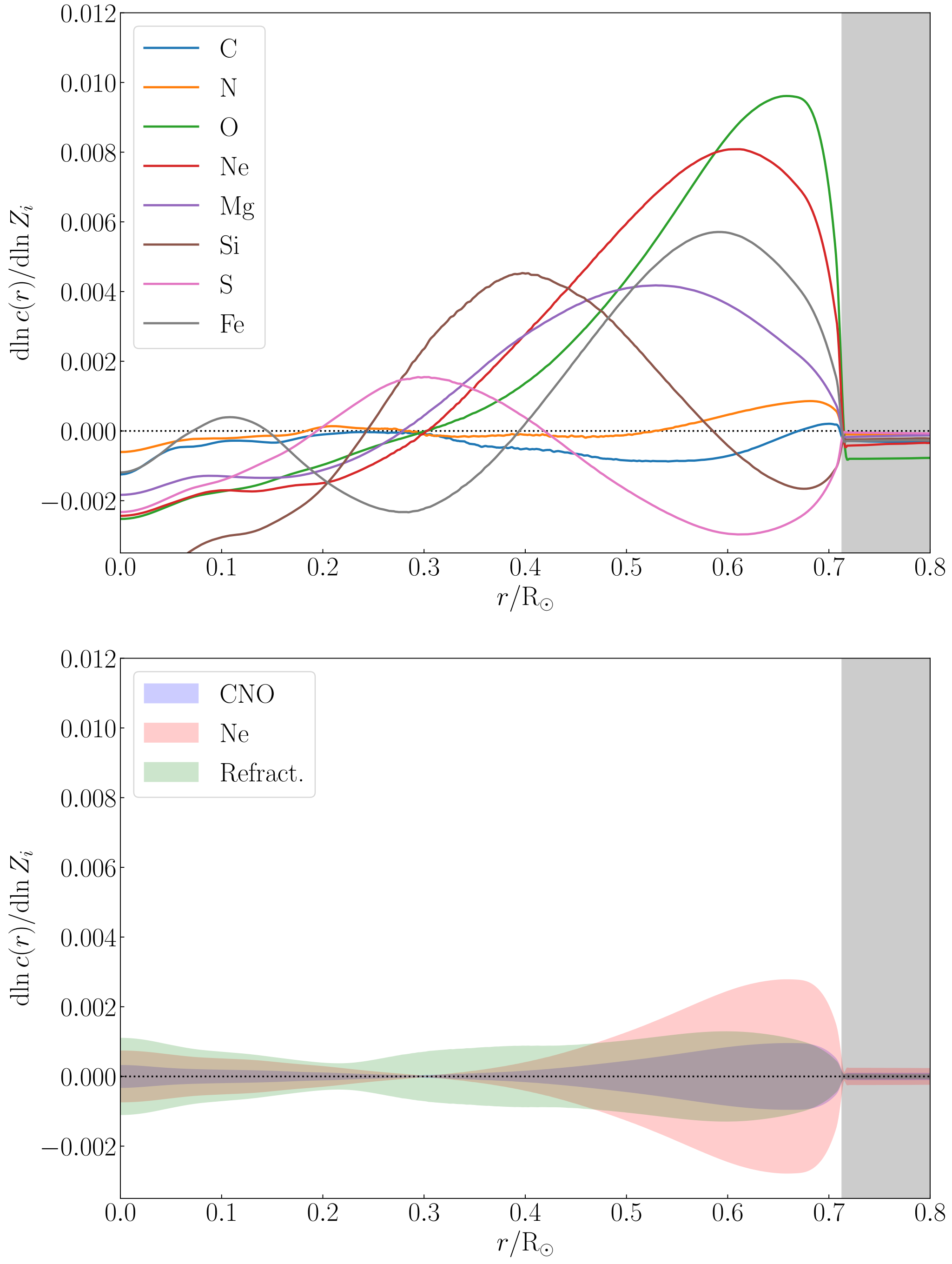

Figure 4.7: Upper panel: Logarithmic partial derivatives of the sound speed with respect to element abundances. Lower panel: fractional 1σ uncertainties in the solar model sound speed based on photospheric abundances for different groups of elements as indicated.

for the SSMs computed with the Asplund et al. (2021) (AAG21), Caffau et al. (2011) (C11), Asplund et al. (2009) (AGSS09-met), and Grevesse & Sauval (1998) (GS98) compositions. The figure also includes, in shaded area, the uncertainty in the sound speed profile due to uncertainties in the SSM inputs computed using the method from Villante et al. (2014) (see also below).

Results show that SSMs based on the solar mixtures obtained in this work reproduce the solar sound speed profile with much higher accuracy than the AGSS09-met model, interestingly, at a comparable level to the GS98 SSM. This is due to the higher metal abundances found in this work, in particular for O, and to a lesser extent refractories, compared to Asplund et al. (2009) results. The similarity between results of the MB22 SSMs and GS98 could be expected given that the global $(Z/X)_\odot$ is very similar. However, it is important to highlight that the internal distribution of elements is different in our and GS98 solar mixtures and the agreement in Z/X is a numerical coincidence. For instance, for two critical elements, O and Si, our values are 15% lower and 10% higher, respectively, compared to GS98. For completeness, we have included a SSM based on the Asplund et al. (2021) composition which shows a partial improvement with respect to the AGSS09-met model, but still far from the SSMs based on the solar mixtures determined in the present work.

To quantify the impact of solar abundances on the sound speed profile, we follow Villante et al. (2014) and show the logarithmic partial derivatives of the sound speed profile with respect to the abundance of individual elements in the left panel of Fig. 4.7. These derivatives depend only slightly on the reference solar mixture but some differences with respect to Villante et al. (2014) can be observed. The right panel of Fig. 4.7 shows the actual fractional sound speed uncertainty in the models due to uncertainties is solar abundances, with chemical elements grouped as indicated in the figure and using the photospheric uncertainties given in Table 4.5. The uncertainty in Ne plays a dominant role in the regions below the convective envelope. The uncertainty due to refractory elements is dominant below $0.45\mathrm{R}_\odot$. This is different from previous results on SSMs (see e.g. Vinyoles et al. 2017) and is due to the larger spectroscopic uncertainties given in the present work.

A summary of relevant characteristics of SSMs used in this work is given in Table 4.6. The depth of the convective envelope, R_{CZ}, and the surface helium abundance Y_{S} are two widely used helioseismic probes of SSMs and should be compared to their observational values, $0.713 \pm 0.001\mathrm{R}_\odot$ (Basu & Antia, 1997) and 0.2485 ± 0.0034 (Basu et al., 2004) respectively. Note that, despite the fact that our photospheric Z/X is almost equal to that of GS98, Z_{ini} in the MB22 models is 5% lower than in the GS98 SSM. This is due to the higher abundance of refractories in our results, which result in a slightly larger opacity in the solar core and a higher Y_{ini} (or lower initial hydrogen) to satisfy the solar luminosity constraint. In addition, we provide the averaged rms of the sound speed fractional difference. While it is beyond the scope of this paper to present a complete analysis of the comparison between SSMs and helioseismic observations, it is clear that our newly derived solar mixture improves the agreement between the observed helioseismic characteristics of the Sun and SSMs. Our results are close to those based on GS98 solar mixture, despite drastically different approaches.

As shown in Fig. 4.5, the agreement between the photospheric and meteoritic scales is excellent. This is also reflected by the similarity of the results obtained with the MB22-photo and MB22-met SSMs.

The SSM presented in the current work provides a good consistency with the solar structure based on helioseismic observations. While SSMs offer an incomplete description of the physics in the solar interior, current results alleviate the need for more complex physics, such as accretion of metal-poor material (Serenelli et al., 2011), energy transport by dark matter particles (Vincent et al., 2015), revision of opacities (Bailey et al., 2015), enhanced gravitational settling and other effects (Guzik & Mussack, 2010).

4.5 Conclusions

In this work, we used new observational material for the Sun, new updated atomic data, and up-to-date NLTE model atoms, to re-analyse the detailed chemical composition of the solar photosphere. For O I, we re-computed the oscillator strengths using several independent approaches, finding excellent agreement between the new values and those adopted in Bergemann et al. (2021). New log(gf) values were also computed for Ni I transitions. We used two families of 3D radiation-hydrodynamics simulations of solar convection, CO5BOLD and STAGGER, to represent the solar atmosphere, which allowed us for the first time to quantify the differences between the abundances inferred with both models. We focused on carrying out the analysis in such a way that it can be applied directly to stars observed within ongoing and upcoming large-scale spectroscopic surveys, such as 4MOST, WEAVE, and SDSS-V.

We provided new estimates of chemical abundances for elements most relevant for the calculations of standard solar models, including C, N, O, Mg, Si, Ca, Fe, and Ni. We complement these results with estimates of the solar abundances of Mn, Ti, Co, Cr, and Sr from our previous studies based on NLTE. Comparing our abundances of refractories with the element ratios based on CI chondrites, we find an excellent agreement between the two scales. We find that for most species our abundances are in good agreement with other literature values obtained with detailed NLTE methods, 1D and 3D model atmospheres (e.g. Caffau et al., 2011, Osorio et al., 2015, Alexeeva et al., 2018, Mashonkina et al., 2019).

We determine the solar photospheric present-day Z/X ratio of 0.0225, when calculated using the photospheric abundances only, and 0.0226, if the meteoritic abundances are used for most species, except C, N, and O, for which the photospheric values are used. Our estimates are 26% higher compared to those determined by Asplund et al. (2021), but they are in a much better agreement with Caffau et al. (2011) and Grevesse & Sauval (1998), the difference being 10% and 1%, respectively. The very close numerical agreement of Z/X with Grevesse & Sauval (1998) is, however, fortuitous, as abundances of individual elements are different in our and their study. Whereas the latter study made use of 1D LTE models, their uncertainties are more conservative (of the order 10 to 20 % for most elements) and appear to be more realistic, which accounts for the difference with Asplund et al. (2009) and Asplund et al. (2021).

Our detailed calculations of SSMs suggest that the presented in this study chemical composition leads to consistent results between the interior structure of the Sun and the helioseismic quantities that match results based on the old spectroscopic results (e.g. Grevesse & Noels 1993, Grevesse & Sauval 1998). It is the first time that SSMs using state-of-the-art spectroscopic results for solar abundances are able to reproduce the solar interior properties as determined through helioseismic techniques. We are confident this works brings us close to the solution of the *solar abundance problem*, arisen in the early 2000s with the initial results on solar O based on 3D models and NLTE line formation (Asplund, 2005), a problem that had defied all attempted solutions in the form of non standard stellar physics. The residual differences can possibly be explained by other systematic limitations of stellar models (Buldgen et al., 2019).

Appendix: Individual Abundances

Below we provide abundances derived from individual lines observed in the solar spectrum. For details on the methods see Sect. 4.2.

Table 4.7: ⟨3D⟩ NLTE abundances derived from individual spectral lines

λ[Å]	A(el)
C I	
5052.160	8.61
6587.610	8.51
7113.180	8.57
N I	
8629.200	8.05
8683.400	7.91
O I	
6300.304	8.75
7771.940	8.76
7774.170	8.78
7775.390	8.79
Mg I	
5528.405	7.51
5711.088	7.59
Si I	
5645.600	7.60
5684.480	7.60
5690.425	7.62
5701.104	7.52
5772.146	7.62
5793.073	7.49
6741.640	7.71
7034.900	7.69
7226.210	7.58
Ca I	
5260.387	6.30
5512.980	6.35
5867.562	6.42
6166.439	6.38
6455.598	6.37
6471.662	6.35
6499.650	6.39
Fe I	
5242.491	7.52
5365.399	7.17
5379.574	7.55
Fe I	
5398.279	7.50
5560.212	7.61
5638.262	7.42
5661.346	7.44
5679.023	7.79
5731.762	7.69
5741.848	7.63
5855.077	7.49
5905.672	7.49
5930.180	7.63
6027.051	7.51
6056.005	7.41
6093.644	7.65
6165.360	7.56
6187.990	7.53
6270.225	7.47
Fe II	
5234.625	7.39
5325.553	7.43
5425.257	7.45
5543.936	7.55
6084.111	7.59
6456.383	7.54
Ni I	
4740.170	6.26
4811.980	6.26
4814.600	6.19
4976.130	6.20
5157.980	6.13
5537.100	6.07
6176.820	6.29
6204.600	6.24
6223.990	6.23
6414.590	6.24
Ni II	
6378.260	6.26

5

Evolution of Ni in the Milky Way.

5.1 Motivation

Nickel is one of the most crucial elements in astrophysics. As discussed in Sect. 1.2, it is one of the end products of nuclear fusion in stars. Nickel naturally occurs in a state of 5 stable isotopes and a number of additional radioisotopes, with ^{58}Ni being the most abundant (68% of isotopic fraction[1]). While the decay of ^{56}Ni isotope to ^{56}Co, and then ^{56}Fe shapes the light curve of the SN Ia explosion – a phenomenon commonly used to estimate distances in cosmology, see Sect. 1.3 – it is usually ^{58}Ni which is most relevant in studies of chemical element production. ^{58}Ni is produced out of the equilibrium during the explosion of a core-collapse SN or SN Ia in the quickly expanding gas encountered by the shock (Woosley & Weaver, 1995, José & Iliadis, 2011). These conditions are known as *α-rich freeze-out*, found in the low densities and high temperatures ($T > 10^9$ K) matter with overabundance of $\alpha-$particles. As a consequence, ^{58}Ni is a sensitive tracer of the explosion physics. As shown in Kirby et al. (2019), ratio of Ni to Fe abundances in Dwarf Galaxies is consistent only with the sub-Chandrasekhar mass progenitors.

Early Galactic chemical evolution (GCE) studies pointed out a good agreement between modelled and observed evolution of Ni in the Milky Way (Timmes et al., 1995). However,

---

[1] `https://www.ciaaw.org/nickel.htm`

recent studies report a systematic discrepancy between the evolution of the observed Ni abundance and the theoretical GCE tracks (Kobayashi et al., 2020, Palla, 2021). While the observed ration of Ni to Fe appears to be relatively constant (e.g. Bensby et al., 2014, Jönsson et al., 2020) and close to solar in stars of all Galactic populations, the GCE models tend to systematically under-produce Ni compared to Fe in the metal-poor regime of older populations. The discrepancy is often attributed to the limitations of the adopted SN models or models of the Galactic structure.

In this Chapter, however, I will focus on the observational data and possible biases resulting from adopted LTE modelling. So far, in the literature the abundances of Ni have been determined under the simplifying assumption of LTE (e.g. Luck & Bond, 1983, Edvardsson et al., 1993, Bensby et al., 2014, Wood et al., 2014, Jönsson et al., 2020). A comprehensive model of Ni for NLTE computations was developed in Bergemann et al. (2021) for the first time and later applied in the analysis of the solar photospheric abundance by Magg et al. (2022). Here we use an updated version of that model atom that includes new quantum-mechanical data for inelastic Ni+H collisions (Voronov et al., 2022).

5.2 Introducing the data

In this work, we make use of the abundances measured in 714 main-sequence stars and subgiants presented in Bensby et al. (2014). This study employed NLTE modelling to estimate $T_{\rm eff}$ and $\log g$ of the sample stars along with the self-consistent estimates of metallicity and micro-turbulence using the NLTE Fe model atom from Lind et al. (2012). However, Ni abundances were inferred under the assumption of LTE. In addition, Bensby et al. (2014) used optical high-resolution spectra with $R \gtrsim 42\,000$ and the SNR exceeding 150, thus ensuring that the errors of the observational origin are minimal. Results from Bensby et al. (2014) are also qualitatively in good agreement with other studies that reported Ni abundances in Galactic populations (e.g. Jönsson et al., 2020, Sakari et al., 2018).

5.3 Results

Fig. 5.1 shows NLTE corrections for the Ni I lines used in Wood et al. (2014) computed for the Sun. NLTE corrections are flat as a function of both the equivalent width of the line (middle panel) and excitation energy (lower panel), with a notably larger scatter around equivalent width below 100 mÅ. We also did not detect any unusual behaviour as a function of wavelength, in contrast to a trend observed by Wood et al. (2014), where spectral lines shorter than 4000 Å yield photospheric solar abundances systematically lower, by $\sim$ 0.1

dex. Average NLTE correction over all lines in case of the Sun is $\sim$ 0.03 dex. With that in mind, it is not surprising that previous studies did not focus on NLTE effects in Ni line formation as such small NLTE effect is not a dominant source of uncertainty, compared e.g. to the uncertainty on atomic data. However, at the lower metallicity $[Fe/H] < -1$, NLTE effects become much more prominent and reach up to $\sim$ 0.4 dex already at [Fe/H]$= -2$. As mentioned in Sect. 5.1, most recent studies point to the significant mismatch between the observed Ni abundances and the theoretical models of GCE in the low-metallicity regime.

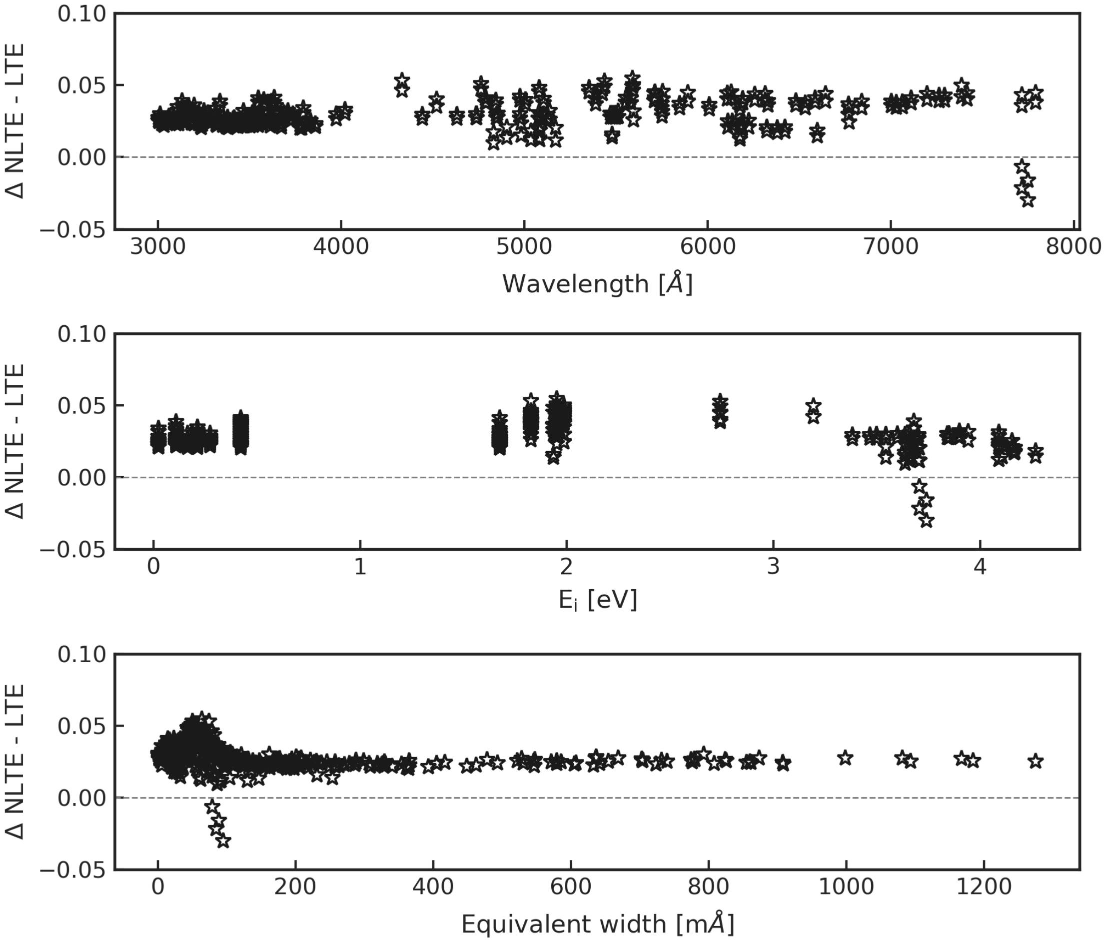

Figure 5.1: NLTE corrections for 327 Ni I lines from Wood et al. (2014) computed for the Sun.

We therefore investigate possible influence of NLTE effects on studies of GCE using an observational sample from Bensby et al. (2014). The NLTE effects were computed following the same procedure as described in Sect. 2.5.1. All 55 Ni lines covering the broad wavelength range from 4686.21 Å to 7826.77 Å from Bensby et al. (2014) were included in the

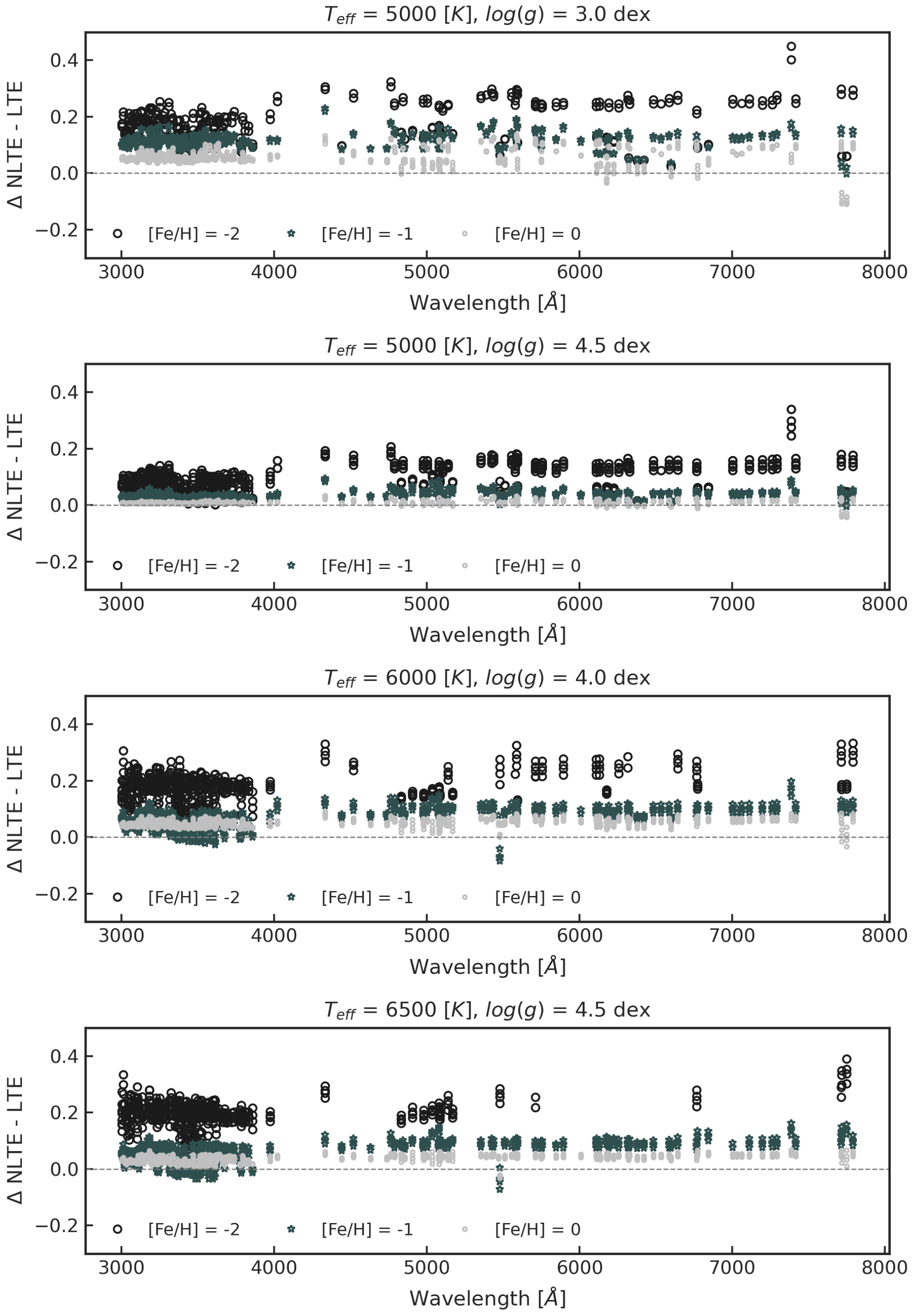

Figure 5.2: NLTE corrections for 327 Ni I lines from Wood et al. (2014) computed for four different model atmospheres at various metallicities.

NLTE computations. We construct a representative set of model atmospheres covering the parameter space investigated in Bensby et al. (2014), making sure to include all relevant evolutionary stages, as demonstrated on Fig. 5.3. The metallicities of the selected model atmospheres range within the bounds of the observed sample ($-3 < [\mathrm{Fe/H}] < +1$). We then computed the NLTE corrections for each diagnostic line assuming the scaled solar Ni/Fe ratio (as LTE [Ni/Fe] distributions are close to the zero). Determination of NLTE corrections using the LTE abundances as the central value is common in abundance calculations (e.g. Souto et al., 2019, Nissen et al., 2021, Roederer & Lawler, 2021). A detailed investigation of the sensitivity of NLTE corrections to the exact abundance of the element can be found in e.g. Eitner et al. (2019). NLTE abundances are then computed using LTE values provided in Bensby et al. (2014) and precomputed NLTE corrections. Comparison of the LTE and NLTE abundances is presented on Fig. 5.4. As expected, NLTE effects drive Ni abundances upwards at lower metallicities, thus eliminating a trend of sub-solar Ni abundances at the metallicity [Fe/H] < -1.0, as seen in the assumption of LTE. On the example of the Ni I line at 6300.341 Å – that blends with the forbidden O I line at 6300.304 Å, Bergemann et al. (2021) showed that combining 3D and NLTE modelling weakens the line even further, thus increasing derived abundance.

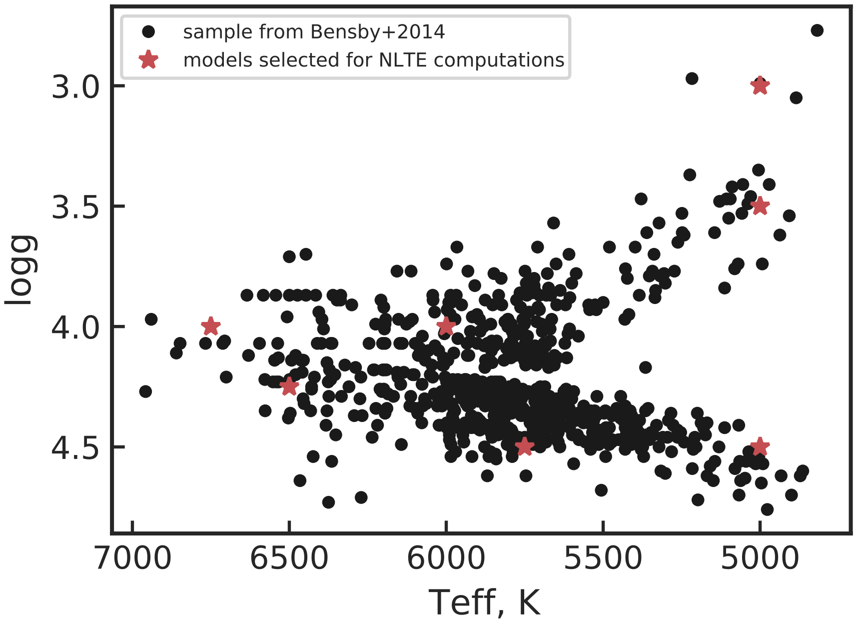

Figure 5.3: Hertzsprung-Russel diagram for the stars analysed in Bensby et al. (2014). Red star symbols mark the representative parameters selected for the NLTE computations.

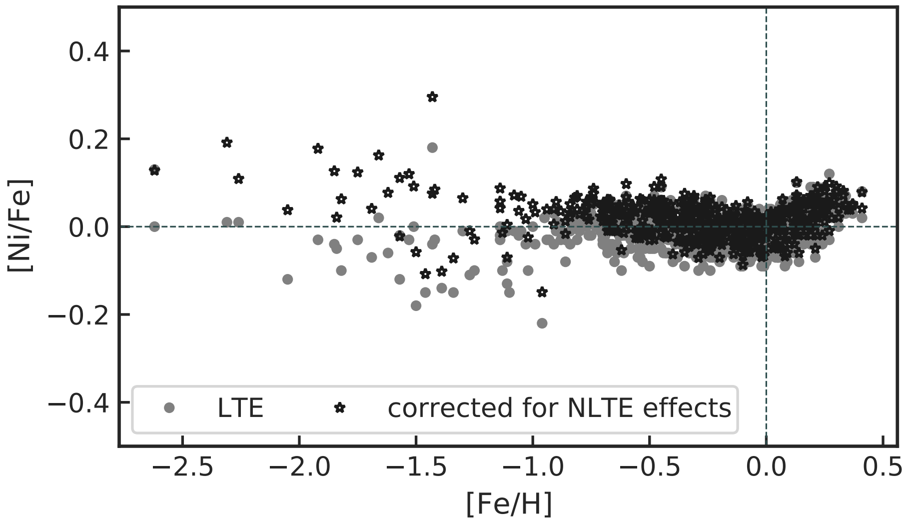

Figure 5.4: Ni abundance relative to Fe abundance from Bensby et al. (2014). Black star symbols correspond to Ni abundance corrected for NLTE effects, see Sect. 5.3 for details.

5.4 SUMMARY AND PERSPECTIVES

We showed that NLTE analysis significantly affects observed evolution of Ni abundance in Galactic populations. The effect is especially prominent at lower metallicities – regime, at which GCE models do not seem to match observations. The latter is usually explained by the limitations of either the SN explosion models, or the GCE models. However, we stress the importance of both precise and accurate abundance analysis, that includes accounting for 3D and NLTE effects.

As shown in Eitner et al. (2022), the NLTE analysis of Mn and Fe in Galactic disk and halo stars concludes that a significant fraction of SN Ia ($> 50\%$) stem from the explosion of sub-Chandrasekhar mass objects. However, such single-element studies do not hold the power to disentangle, e.g. intrinsic differences arising from various sets of SN yields (e.g. Chieffi & Limongi, 2004, Limongi & Chieffi, 2018, Nomoto et al., 2013). In this regard, multi-element analysis, combining e.g. Mn, Ni, and Zn abundances of the Galactic populations is a promising step towards constraining the models of the SN Ia progenitors.

6

Conclusions and future outlook

6.1 SUMMARY

This thesis presents my work on the NLTE radiative transfer and its application to the spectroscopic analysis of individual stars and stellar populations. By simply undertaking the NLTE approach to the spectroscopic analysis our understanding of stellar evolution, and consequently Galactic chemical evolution changes significantly.

First, I show that NLTE effects must be taken into account to disentangle the small-scale effects of secular evolution in stellar populations. A systematic, statistical analysis of the observed abundance distributions in a relatively young star cluster NGC2420 demonstrates that the chemical abundance distributions display significant trends with the evolutionary stages of the stars. By comparing the abundance distributions to the CESTAM models computed taking into account atomic diffusion and different prescriptions for turbulent mixing, as well as mixing induced by rotation, we were able to constrain the depth of the zone in which the turbulent mixing takes place. The obvious but nonetheless important consequence of our study is that accurate identification of membership in stellar associations *cannot* rely on metallicity.

Re-analysing the detailed chemical composition of the solar photosphere using NLTE modelling of multiple species and state-of-the-art observational material and atomic data brought us closer to understanding the long-standing *solar abundance problem*: a mismatch between the solar modelling based on solar composition as compared to asteroseismic observations. We determine the solar photospheric present-day Z/X ratio of 0.0225, also in an excellent agreement with the measurements based on CI chondrites.

Lastly, I present the first broad-range NLTE computations for diagnostic Ni lines used in studies of Galactic chemical enrichment, in particular as a way to constrain explosive physics of SN Ia. These computations show that NLTE effects are uncomfortably large in the regime that is considered to display a puzzling mismatch between the models of chemical evolution and observed abundances in the literature. A 3D modelling of a stellar atmosphere combined with NLTE radiative transfer as well as multi-element combined observational analysis are proposed as the next step towards improved GCE models.

6.2 OUTLOOK

It is an inspiring time for stellar astrophysics. Large spectroscopic surveys are providing a vast amount of unprecedented quality data. Yet, the quality and quantity are expected to continuously improve with the start of the upcoming projects like 4MOST, PLATO, and WEAVE. At the same time one has never had such an abundance of computational resources.

It is thus our responsibility to push for the most realistic physical modelling to make the best out of the available resource. I am excited to see future developments in the 3D modelling, also fully coupled with the radiative transfer. Machine learning methods that are gaining more and more popularity for spectroscopic studies hold an enormous potential for allowing spectral analysis of million-stars samples. Such rich data sets combined with kinematic information from, e.g., the Gaia mission are key to exploring the formation and evolution of our Galaxy and beyond.

Another exciting application of improved stellar modelling is that for the studies of exoplanetary atmospheres. Is there life on planets other than Earth? If so, is it anything like what we are? Being rather philosophical questions, they can be tackled by observing planets similar – or not so much – to our own home. It is only how well we understand bright central star(s) that defines how precise our inference of the planetary traits is.

From the nucleosynthesis perspective, heavy chemical elements as tracers of the most exotic cosmic events have been a promising research direction. This is an appealing opportunity to build connections and collaborations with physicists and chemists – whether they are found in a laboratory or behind a supercomputer – as atomic data is still one of the most crucial parts of spectroscopic studies.

And last but not least, I am exciting to see advances in the modelling of molecular species in the stellar interiors. Molecules have been an essential component in studies of interstellar medium and exoplanetary bodies for a long while and now their importance is being recognised in the field of stellar astrophysics as well. Modelling molecular species comes with many challenges, e.g. a necessity to account for convective movements in the cooler regions of stellar interiors, need for large compilations of line formation data as well as the most state-of-the-art observational material. Yet the effort will be well worth it, as molecules are crucial to understand many aspect of stellar physics. For example the oldest stars in the Universe – our window to the time before most of the known to us chemical elements formed – show almost no features in their observed spectrum other than CH and OH molecular lines (Masseron, 2015, Gallagher et al., 2016).

6.3 LIST OF PUBLICATIONS

First author publications:

- The Gaia-ESO survey: 3D NLTE abundances in the open cluster NGC 2420 suggest atomic diffusion and turbulent mixing are at the origin of chemical abundance variations, 2020, A&A Semenova et al. (2020).
- Observational constraints on the origin of the elements. IV. Standard composition of the Sun, 2022, A&A, Magg et al. (2022)

Co-authorship:

- Solar oxygen abundance, 2021, MNRAS Bergemann et al. (2021)
- The chemical composition of globular clusters in the Local Group, 2022, A&A Larsen et al. (2022)
- Non-LTE Radiative Transfer with Turbospectrum, 2022, Gerber et al. (2022)
- Metal Mixing in the R-Process Enhanced Ultra-Faint Dwarf Galaxy Reticulum II, 2022, Ji et al. (2022)

Acknowledgements

"It was a bright cold day in April, and the clocks were striking thirteen."
– 1984

This thesis and work related would not have been possible without many people helping me on the way.

First of all, I am thankful to my supervisor Maria Bergemann for the supervision and teaching me a lot on the way.

All the work presented in this thesis is a result of close collaborations. My many thanks go to the wonderful colleagues: Aldo Serenelli, Morgan Deal, Bertrand Plez, Ulrike Heiter, Manuel Bautista, all the co-authors mentioned earlier, and of course Maria Bergemann. I did not get to do many research visits as the world of pandemic had its own plans and I highly value all the collaborations that happened over video calls across many time zones.

I was lucky to be able to build on the progress done by the group members: Camilla Hansen, Andy Gallagher, Mikhail Kovalev, Richard Hoppe, Philipp Eitner (who also set a very high standard), thank you for your constant hard work.

Thank you for agreeing to hold my defence to Saskia Hekker, Luca Amendola, Maria Bergemann and Andreas Koch-Hansen, who also kindly agreed to referee this thesis.

My special gratitude goes to the MPIA IT group for their relentless and timely help so crucial for this heavily computational project.

Many thanks to MPIA student representatives for standing for our rights and doing their best to improve the working conditions while pursuing their own PhD.

The team of Astronomy & Astrophysics (A&A): thank you for making the publishing process so easy and smooth. The GES collaboration: for supporting my research and providing a valuable feedback. To 4MOST and PLATO surveys for many insights and discussions and I hope you will have great success in the future.

The work in this thesis was supported by the Collaborative Research centre SFB 881 (project A10), Heidelberg University, of the Deutsche Forschungsgemeinschaft (DFG, German Research Foundation).

To friends and close ones: I hope you do not need to read my thesis to know how much I treasure you.

References

Abbott, B. P., Abbott, R., Abbott, T. D., et al. 2017, Phys. Rev. Lett., 119, 161101

Adibekyan, V. 2019, Geosciences, 9, 105

Alecian, G., & LeBlanc, F. 2002, MNRAS, 332, 891

Alexeeva, S., Chen, T., Ryabchikova, T., et al. 2020, ApJ, 896, 59

Alexeeva, S., Ryabchikova, T., Mashonkina, L., & Hu, S. 2018, ApJ, 866, 153

Alexeeva, S. A., & Mashonkina, L. I. 2015, MNRAS, 453, 1619

Alonso, A., Arribas, S., & Martinez-Roger, C. 1996, A&AS, 117, 227

Alvarez, R., & Plez, B. 1998, A&A, 330, 1109

Amarsi, A. M., & Asplund, M. 2017, MNRAS, 464, 264

Amarsi, A. M., Barklem, P. S., Asplund, M., Collet, R., & Zatsarinny, O. 2018, A&A, 616, A89

Amarsi, A. M., Barklem, P. S., Collet, R., Grevesse, N., & Asplund, M. 2019, A&A, 624, A111

Amarsi, A. M., Grevesse, N., Asplund, M., & Collet, R. 2021, arXiv e-prints, arXiv:2109.04752

Amarsi, A. M., Grevesse, N., Grumer, J., et al. 2020a, A&A, 636, A120

Amarsi, A. M., Lind, K., Asplund, M., Barklem, P. S., & Collet, R. 2016, MNRAS, 463, 1518

Amarsi, A. M., Lind, K., Osorio, Y., et al. 2020b, A&A, 642, A62

Anders, E., & Grevesse, N. 1989, Geochim. Cosmochim. Acta, 53, 197

Angulo, C. 1999, in American Institute of Physics Conference Series, Vol. 495, American Institute of Physics Conference Series, 365–366

Anstee, S. D., & O'Mara, B. J. 1991, MNRAS, 253, 549

—. 1995, MNRAS, 276, 859

Anthony-Twarog, B. J., Tanner, D., Cracraft, M., & Twarog, B. A. 2006, AJ, 131, 461

Arancibia-Silva, J., Bouvier, J., Bayo, A., et al. 2020, A&A, 635, L13

Asplund, M. 2005, ARA&A, 43, 481

Asplund, M., Amarsi, A. M., & Grevesse, N. 2021, A&A, 653, A141

Asplund, M., Grevesse, N., Sauval, A. J., & Scott, P. 2009, ARA&A, 47, 481

Asplund, M., Lambert, D. L., Nissen, P. E., Primas, F., & Smith, V. V. 2006, ApJ, 644, 229

Badnell, N. R. 2011, in American Institute of Physics Conference Series, Vol. 1344, 7th International Conference on Atomic and Molecular Data and Their Applications - ICAMDATA-2010, ed. A. Bernotas, R. Karazija, & Z. Rudzikas, 139–148

Badnell, N. R., Bautista, M. A., Butler, K., et al. 2005, MNRAS, 360, 458

Bahcall, J. N., Serenelli, A. M., & Basu, S. 2005, ApJ, 621, L85

Bailey, J. E., Nagayama, T., Loisel, G. P., et al. 2015, Nature, 517, 56

Bard, A., Kock, A., & Kock, M. 1991, Astron. and Astrophys., 248, 315, (BKK)

Bard, A., & Kock, M. 1994, Astron. and Astrophys., 282, 1014, (BK)

Barklem, P. S. 2018, A&A, 612, A90

Barklem, P. S., & Aspelund-Johansson, J. 2005, Astron. and Astrophys., 435, 373, (BA-J)

Barklem, P. S., Belyaev, A. K., Spielfiedel, A., Guitou, M., & Feautrier, N. 2012, A&A, 541, A80

Barklem, P. S., Piskunov, N., & O'Mara, B. J. 2000, A&AS, 142, 467

Basu, S. 2021, ApJ, 917, 45

Basu, S., & Antia, H. M. 1997, MNRAS, 287, 189

—. 2008, Phys. Rep., 457, 217

Basu, S., Chaplin, W. J., Elsworth, Y., New, R., & Serenelli, A. M. 2009, ApJ, 699, 1403

Basu, S., Mazumdar, A., Antia, H. M., & Demarque, P. 2004, MNRAS, 350, 277

Bautista, M. A., Lind, K., & Bergemann, M. 2017, A&A, 606, A127

Bedell, M., Bean, J. L., Meléndez, J., et al. 2018, ApJ, 865, 68

Belokurov, V., Zucker, D. B., Evans, N. W., et al. 2006, ApJ, 642, L137

Belyaev, A. K., Voronov, Y. V., Mitrushchenkov, A., Guitou, M., & Feautrier, N. 2019, Monthly Notices of the Royal Astronomical Society, 487, 5097

Belyaev, A. K., Voronov, Y. V., Yakovleva, S. A., et al. 2017, The Astrophysical Journal, 851, 59

Belyaev, A. K., Yakovleva, S. A., & Barklem, P. S. 2014, A&A, 572, A103

Belyaev, A. K., Yakovleva, S. A., Guitou, M., et al. 2016, A&A, 587, A114

Bensby, T., Feltzing, S., & Oey, M. S. 2014, A&A, 562, A71

Bergemann, M. 2011, MNRAS, 413, 2184

Bergemann, M., & Cescutti, G. 2010, A&A, 522, A9

Bergemann, M., Collet, R., Amarsi, A. M., et al. 2017, ApJ, 847, 15

Bergemann, M., Hansen, C. J., Bautista, M., & Ruchti, G. 2012a, A&A, 546, A90

Bergemann, M., Kudritzki, R.-P., Würl, M., et al. 2013, ApJ, 764, 115

Bergemann, M., Lind, K., Collet, R., Magic, Z., & Asplund, M. 2012b, MNRAS, 427, 27

Bergemann, M., & Nordlander, T. 2014, arXiv e-prints, arXiv:1403.3088

Bergemann, M., Pickering, J. C., & Gehren, T. 2010, MNRAS, 401, 1334

Bergemann, M., Sesar, B., Cohen, J. G., et al. 2018, Nature, 555, 334

Bergemann, M., Gallagher, A. J., Eitner, P., et al. 2019, A&A, 631, A80

Bergemann, M., Hoppe, R., Semenova, E., et al. 2021, MNRAS, doi:10.1093/mnras/stab2160

Berrington, K. A., Eissner, W. B., & Norrington, P. H. 1995, Computer Physics Communications, 92, 290

Bertelli Motta, C., Pasquali, A., Richer, J., et al. 2018, MNRAS, 478, 425

Blackwell, D. E., Petford, A. D., Shallis, M. J., & Simmons, G. J. 1982a, MNRAS, 199, 43

Blackwell, D. E., Petford, A. D., & Simmons, G. J. 1982b, MNRAS, 201, 595

Blanco-Cuaresma, S., & Fraix-Burnet, D. 2018, A&A, 618, A65

Blanco-Cuaresma, S., Soubiran, C., Heiter, U., et al. 2015, A&A, 577, A47

Bland-Hawthorn, J., & Gerhard, O. 2016, ARA&A, 54, 529

Bochsler, P. 2007, A&A, 471, 315

Boesgaard, A. M., Lum, M. G., & Deliyannis, C. P. 2020, ApJ, 888, 28

Böhm-Vitense, E. 1958, ZAp, 46, 108

Borexino Collaboration, Agostini, M., Altenmüller, K., Appel, S., et al. 2020, Nature, 587, 577

Bossini, D., Vallenari, A., Bragaglia, A., et al. 2019, A&A, 623, A108

Bragaglia, A., & Tosi, M. 2006, AJ, 131, 1544

Breitschwerdt, D., & de Avillez, M. A. 2021, Ap&SS, 366, 94

Bressan, A., Marigo, P., Girardi, L., et al. 2012, MNRAS, 427, 127

Buder, S., Lind, K., Ness, M. K., et al. 2019, A&A, 624, A19

Buder, S., Sharma, S., Kos, J., et al. 2021, MNRAS, 506, 150

Buldgen, G., Salmon, S. J. A. J., Noels, A., et al. 2019, A&A, 621, A33

Bullock, J. S., & Johnston, K. V. 2005, ApJ, 635, 931

Burbidge, E. M., Burbidge, G. R., Fowler, W. A., & Hoyle, F. 1957, Reviews of Modern Physics, 29, 547

Caffau, E., Faraggiana, R., Bonifacio, P., Ludwig, H. G., & Steffen, M. 2007, A&A, 470, 699

Caffau, E., Ludwig, H. G., Bonifacio, P., et al. 2010, A&A, 514, A92

Caffau, E., Ludwig, H. G., Malherbe, J. M., et al. 2013, A&A, 554, A126

Caffau, E., Ludwig, H. G., Steffen, M., et al. 2008, A&A, 488, 1031

Caffau, E., Ludwig, H. G., Steffen, M., Freytag, B., & Bonifacio, P. 2011, Sol. Phys., 268, 255

Cantat-Gaudin, T., Jordi, C., Vallenari, A., et al. 2018, A&A, 618, A93

Canuto, V. M., Goldman, I., & Mazzitelli, I. 1996, ApJ, 473, 550

Carlsson, M. 1986, Uppsala Astronomical Observatory Reports, 33

Casagrande, L., Ramírez, I., Meléndez, J., Bessell, M., & Asplund, M. 2010, A&A, 512, A54

Casagrande, L., Schönrich, R., Asplund, M., et al. 2011, A&A, 530, A138

Casagrande, L., & VandenBerg, D. A. 2018, MNRAS, 479, L102

Casagrande, L., Portinari, L., Glass, I. S., et al. 2014, MNRAS, 439, 2060

Casagrande, L., Lin, J., Rains, A. D., et al. 2021, MNRAS, 507, 2684

Castelli, F., & Kurucz, R. L. 2010, A&A, 520, A57

Chaboyer, B., Fenton, W. H., Nelan, J. E., Patnaude, D. J., & Simon, F. E. 2001, ApJ, 562, 521

Chieffi, A., & Limongi, M. 2004, ApJ, 608, 405

Civiš, S., Kubelík, P., Ferus, M., et al. 2018, ApJS, 239, 11

Collet, R., Asplund, M., & Trampedach, R. 2007, A&A, 469, 687

Cordoni, G., Milone, A. P., Marino, A. F., et al. 2018, ApJ, 869, 139

Costa, G., Girardi, L., Bressan, A., et al. 2019, A&A, 631, A128

Cowan, R. D. 1981, The theory of atomic structure and spectra

De Silva, G. M., Freeman, K. C., Bland-Hawthorn, J., Asplund, M., & Bessell, M. S. 2007, AJ, 133, 694

Deal, M., Alecian, G., Lebreton, Y., et al. 2018, A&A, 618, A10

Deal, M., Goupil, M. J., Marques, J. P., Reese, D. R., & Lebreton, Y. 2020, A&A, 633, A23

Deal, M., Richard, O., & Vauclair, S. 2016, A&A, 589, A140

Deliyannis, C. P., Anthony-Twarog, B. J., Lee-Brown, D. B., & Twarog, B. A. 2019, AJ, 158, 163

Deliyannis, C. P., & Pinsonneault, M. H. 1990, ApJ, 365, L67

Den Hartog, E. A., Lawler, J. E., Sneden, C., et al. 2021, ApJS, 255, 27

Donor, J., Frinchaboy, P. M., Cunha, K., et al. 2020, arXiv e-prints, arXiv:2002.08980

Dotter, A., Conroy, C., Cargile, P., & Asplund, M. 2017, ApJ, 840, 99

Drake, J. J., & Testa, P. 2005, Nature, 436, 525

Drawin, H.-W. 1968, Zeitschrift fur Physik, 211, 404

Edvardsson, B., Andersen, J., Gustafsson, B., et al. 1993, A&A, 275, 101

Eggenberger, P., Maeder, A., & Meynet, G. 2005, A&A, 440, L9

Eitner, P., Bergemann, M., Hansen, C. J., et al. 2020, A&A, 635, A38

Eitner, P., Bergemann, M., & Larsen, S. 2019, A&A, 627, A40

Eitner, P., Bergemann, M., Ruiter, A. J., et al. 2022, arXiv e-prints, arXiv:2206.10258

El-Badry, K., Rix, H.-W., Ting, Y.-S., et al. 2018, MNRAS, 473, 5043

Ezzeddine, R., Sitnova, T., Frebel, A., Mashonkina, L., & Plez, B. 2018, in IAU Symposium, Vol. 334, Rediscovering Our Galaxy, ed. C. Chiappini, I. Minchev, E. Starkenburg, & M. Valentini, 259–262

Ezzeddine, R., Frebel, A., Roederer, I. U., et al. 2019, ApJ, 876, 97

Ferguson, J. W., Alexander, D. R., Allard, F., et al. 2005, ApJ, 623, 585

Fields, B. D. 2011, Annual Review of Nuclear and Particle Science, 61, 47

Fraser, M., Casey, A. R., Gilmore, G., Heger, A., & Chan, C. 2017, MNRAS, 468, 418

Frebel, A., Aoki, W., Christlieb, N., et al. 2005, Nature, 434, 871

Freeman, K., & Bland-Hawthorn, J. 2002, ARA&A, 40, 487

Freytag, B., Steffen, M., Ludwig, H. G., et al. 2012, Journal of Computational Physics, 231, 919

Froese Fischer, C., Gaigalas, G., Jönsson, P., & Bieroń, J. 2019, Computer Physics Communications, 237, 184

Froese Fischer, C., Godefroid, M., Brage, T., Jönsson, P., & Gaigalas, G. 2016, Journal of Physics B: Atomic, Molecular and Optical Physics, 49, doi:10.1088/0953-4075/49/18/182004

Fuhr, J. R., Martin, G. A., & Wiese, W. L. 1988, Journal of Physical and Chemical Reference Data, Volume 17, Suppl. 4. New York: American Institute of Physics (AIP) and American Chemical Society, 1988, 17, (FMW)

Gaia Collaboration, Prusti, T., de Bruijne, J. H. J., et al. 2016, A&A, 595, A1

Gaia Collaboration, Brown, A. G. A., Vallenari, A., et al. 2018, A&A, 616, A1

Gallagher, A. J., Bergemann, M., Collet, R., et al. 2020, A&A, 634, A55

Gallagher, A. J., Caffau, E., Bonifacio, P., et al. 2016, A&A, 593, A48

Gao, X., Lind, K., Amarsi, A. M., et al. 2018, MNRAS, 481, 2666

—. 2020, MNRAS, 497, L30

Garz, T. 1973, A&A, 26, 471, (GARZ)

Gehren, T., Liang, Y. C., Shi, J. R., Zhang, H. W., & Zhao, G. 2004, A&A, 413, 1045

Geiss, J., Buehler, F., Cerutti, H., & Eberhardt, P. 1972, Solar-Wind Composition Experiment, Vol. 289, 15

Gent, M. R., Bergemann, M., Serenelli, A., et al. 2022, A&A, 658, A147

Gerber, J. M., Magg, E., Plez, B., et al. 2022, arXiv e-prints, arXiv:2206.00967

Gilmore, G., Wyse, R. F. G., & Norris, J. E. 2002, ApJ, 574, L39

Gilmore, G., Randich, S., Asplund, M., et al. 2012, The Messenger, 147, 25

Gloeckler, G., & Fisk, L. A. 2007, Space Sci. Rev., 130, 489

Gordon, K. D., Gies, D. R., Schaefer, G. H., Huber, D., & Ireland, M. 2019, The Astrophysical Journal, 873, 91

Grant, I. 2007, Relativistic Quantum Theory of Atoms and Molecules: Theory and Computation, Springer Series on Atomic, Optical, and Plasma Physics (Springer New York)

Gratton, R. G., Bonifacio, P., Bragaglia, A., et al. 2001, A&A, 369, 87

Grevesse, N., & Noels, A. 1993, in Origin and Evolution of the Elements, ed. N. Prantzos, E. Vangioni-Flam, & M. Casse, 15–25

Grevesse, N., & Sauval, A. J. 1998, Space Sci. Rev., 85, 161

Grupp, F. 2004a, A&A, 420, 289

—. 2004b, A&A, 426, 309

Gruyters, P., Nordlander, T., & Korn, A. J. 2014, A&A, 567, A72

Gruyters, P., Lind, K., Richard, O., et al. 2016, A&A, 589, A61

Gustafsson, B., Edvardsson, B., Eriksson, K., et al. 2008, A&A, 486, 951

Guzik, J. A., & Mussack, K. 2010, ApJ, 713, 1108

Haberreiter, M., Schmutz, W., & Hubeny, I. 2008, A&A, 492, 833

Hansen, C. J., Hansen, T. T., Koch, A., et al. 2019, A&A, 623, A128

Harutyunyan, G., Steffen, M., Mott, A., et al. 2018, A&A, 618, A16

Hauschildt, P. H., Allard, F., & Baron, E. 1999, ApJ, 512, 377

Hayden, M. R., Bland-Hawthorn, J., Sharma, S., et al. 2020, MNRAS, 493, 2952

Heiter, U., Jofré, P., Gustafsson, B., et al. 2015a, A&A, 582, A49

Heiter, U., Lind, K., Asplund, M., et al. 2015b, Phys. Scr, 90, 054010

Heiter, U., Lind, K., Bergemann, M., et al. 2021, A&A, 645, A106

Hekker, S. 2018, in Astrophysics and Space Science Proceedings, Vol. 49, Asteroseismology and Exoplanets: Listening to the Stars and Searching for New Worlds, ed. T. L. Campante, N. C. Santos, & M. J. P. F. G. Monteiro, 95

Helmi, A., White, S. D. M., de Zeeuw, P. T., & Zhao, H. 1999, Nature, 402, 53

Helmi, A., Williams, M., Freeman, K. C., Bland-Hawthorn, J., & De Silva, G. 2014, ApJ, 791, 135

Henyey, L., Vardya, M. S., & Bodenheimer, P. 1965, ApJ, 142, 841

Hibbert, A., Biemont, E., Godefroid, M., & Vaeck, N. 1991, Journal of Physics B Atomic Molecular Physics, 24, 3943

—. 1993, A&AS, 99, 179

Hubeny, I., Allende Prieto, C., Osorio, Y., & Lanz, T. 2021, arXiv e-prints, arXiv:2104.02829

Hubeny, I., & Mihalas, D. 2014, Theory of Stellar Atmospheres: An Introduction to Astrophysical Non-equilibrium Quantitative Spectroscopic Analysis, Princeton Series in Astrophysics (Princeton University Press)

Husser, T.-O., Kamann, S., Dreizler, S., et al. 2016, A&A, 588, A148

Imbriani, G., Costantini, H., Formicola, A., et al. 2004, A&A, 420, 625

Ishigaki, M. N., Tominaga, N., Kobayashi, C., & Nomoto, K. 2018, ApJ, 857, 46

Jacobson, H. R., Pilachowski, C. A., & Friel, E. D. 2011, AJ, 142, 59

Ji, A. P., Drout, M. R., & Hansen, T. T. 2019, ApJ, 882, 40

Ji, A. P., Simon, J. D., Roederer, I. U., et al. 2022, arXiv e-prints, arXiv:2207.03499

Jofré, P., & Weiss, A. 2011, A&A, 533, A59

Johansson, S., Litzén, U., Lundberg, H., & Zhang, Z. 2003, ApJ, 584, L107

Johnson, W., Kolb, D., & Huang, K.-N. 1983, Atomic Data and Nuclear Data Tables, 28, 333

Jönsson, H., Holtzman, J. A., Allende Prieto, C., et al. 2020, AJ, 160, 120

Jönsson, P., & Godefroid, M. R. 2000, Molecular Physics, 98, 1141

José, J., & Iliadis, C. 2011, Reports on Progress in Physics, 74, 096901

Juett, A. M., Schulz, N. S., Chakrabarty, D., & Gorczyca, T. W. 2006, ApJ, 648, 1066

Keller, S. C., Bessell, M. S., Frebel, A., et al. 2014, Nature, 506, 463

Kippenhahn, R., Weigert, A., & Weiss, A. 2012, Stellar structure and evolution, second edition edn., Astronomy and astrophysics library (Springer), xviii, 604 pages, doi:10.1007/978-3-642-30304-3

Kirby, E. N., Xie, J. L., Guo, R., et al. 2019, ApJ, 881, 45

Kobayashi, C., Karakas, A. I., & Lugaro, M. 2020, ApJ, 900, 179

Kormendy, J., Drory, N., Bender, R., & Cornell, M. E. 2010, ApJ, 723, 54

Korn, A., Grundahl, F., Richard, O., et al. 2006, The Messenger, 125, 6

Korn, A. J., Grundahl, F., Richard, O., et al. 2007, ApJ, 671, 402

Korotin, S., Andrievsky, S., Caffau, E., & Bonifacio, P. 2017, in Astronomical Society of the Pacific Conference Series, Vol. 510, Stars: From Collapse to Collapse, ed. Y. Y. Balega, D. O. Kudryavtsev, I. I. Romanyuk, & I. A. Yakunin, 141

Korotin, S. A. 2009, Astronomy Reports, 53, 651

Kramida, A. 2008, in APS Meeting Abstracts, Vol. 39, APS Division of Atomic, Molecular and Optical Physics Meeting Abstracts, OPR.10

Kurucz, R. L. 1970, SAO Special Report, 309

—. 1979, ApJS, 40, 1

—. 1993, SYNTHE spectrum synthesis programs and line data (Smithsonian Astrophysical Observatory)

—. 2005, Memorie della Societa Astronomica Italiana Supplementi, 8, 14

Laming, J. M., Heber, V. S., Burnett, D. S., et al. 2017, ApJ, 851, L12

Larsen, S. S., Eitner, P., Magg, E., et al. 2022, A&A, 660, A88

Lawler, J. E., Hala, Sneden, C., et al. 2019, ApJS, 241, 21

LeBlanc, F., & Alecian, G. 2004, MNRAS, 352, 1329

Li, W., Amarsi, A. M., Papoulia, A., Ekman, J., & Jönsson, P. 2021, MNRAS, 502, 3780

Limongi, M., & Chieffi, A. 2018, ApJS, 237, 13

Lind, K., Asplund, M., & Barklem, P. S. 2009, A&A, 503, 541

Lind, K., Bergemann, M., & Asplund, M. 2012, MNRAS, 427, 50

Lind, K., Amarsi, A. M., Asplund, M., et al. 2017, MNRAS, 468, 4311

Liu, F., Asplund, M., Yong, D., et al. 2019, arXiv e-prints, arXiv:1902.11008

Lodders, K. 2003, ApJ, 591, 1220

—. 2019, arXiv e-prints, arXiv:1912.00844

—. 2021, Space Sci. Rev., 217, 44

Luck, R. E., & Bond, H. E. 1983, ApJ, 271, L75

Ludwig, H.-G., Caffau, E., Steffen, M., et al. 2009, MemSAI, 80, 711

Maeder, A. 1974, A&A, 32, 177

Magg, E., Bergemann, M., Serenelli, A., et al. 2022, A&A, 661, A140

Magic, Z., Collet, R., Asplund, M., et al. 2013a, A&A, 557, A26

Magic, Z., Collet, R., Hayek, W., & Asplund, M. 2013b, A&A, 560, A8

Maiorca, E., Uitenbroek, H., Uttenthaler, S., et al. 2014, ApJ, 788, 149

Majewski, S. R., Schiavon, R. P., Frinchaboy, P. M., et al. 2017, AJ, 154, 94

Marques, J. P., Goupil, M. J., Lebreton, Y., et al. 2013, A&A, 549, A74

Mashonkina, L. 2013, A&A, 550, A28

—. 2020, MNRAS, 493, 6095

Mashonkina, L., Korn, A. J., & Przybilla, N. 2007, A&A, 461, 261

Mashonkina, L., Ryabchikova, T., & Ryabtsev, A. 2005, A&A, 441, 309

Mashonkina, L., Sitnova, T., & Belyaev, A. K. 2017, A&A, 605, A53

Mashonkina, L., Sitnova, T., Yakovleva, S. A., & Belyaev, A. K. 2019, A&A, 631, A43

Mashonkina, L., Zhao, G., Gehren, T., et al. 2008, A&A, 478, 529

Masseron, T. 2015, in SF2A-2015: Proceedings of the Annual meeting of the French Society of Astronomy and Astrophysics, 303–305

Matt, S. P., Brun, A. S., Baraffe, I., Bouvier, J., & Chabrier, G. 2015, ApJ, 799, L23

—. 2019, ApJ, 870, L27

Mauas, P. J., Avrett, E. H., & Loeser, R. 1988, ApJ, 330, 1008

May, M., Richter, J., & Wichelmann, J. 1974, A&AS, 18, 405, (MRW)

Meléndez, J., & Barbuy, B. 2009, A&A, 497, 611

Meyer, J.-P. 1989, in American Institute of Physics Conference Series, Vol. 183, Cosmic Abundances of Matter, ed. C. J. Waddington, 245–303

Meynet, G., Maeder, A., & Mowlavi, N. 2004, A&A, 416, 1023

Michaud, G., Alecian, G., & Richer, J. 2015, Atomic Diffusion in Stars (Springer International Publishing Switzerland), doi:10.1007/978-3-319-19854-5

Michaud, G., Fontaine, G., & Beaudet, G. 1984, ApJ, 282, 206

Michaud, G., Richer, J., & Vick, M. 2011, A&A, 534, A18

Morel, P., & Lebreton, Y. 2008, Ap&SS, 316, 61

Mucciarelli, A., Salaris, M., Lovisi, L., et al. 2011, MNRAS, 412, 81

Nieva, M. F., & Przybilla, N. 2012, A&A, 539, A143

Nieva, M. F., & Simón-Díaz, S. 2011, A&A, 532, A2

Nissen, P. E., Silva Aguirre, V., Christensen-Dalsgaard, J., et al. 2017, A&A, 608, A112

Nissen, P. E., Silva-Cabrera, J. S., & Schuster, W. J. 2021, A&A, 651, A57

Nomoto, K., Kamiya, Y., & Nakasato, N. 2013, in Binary Paths to Type Ia Supernovae Explosions, ed. R. Di Stefano, M. Orio, & M. Moe, Vol. 281, 253–260

Nordlander, T., Amarsi, A. M., Lind, K., et al. 2017, A&A, 597, A6

Nordlander, T., Korn, A. J., Richard, O., & Lind, K. 2012, ApJ, 753, 48

Nordlander, T., & Lind, K. 2017, A&A, 607, A75

Nordlund, Å., Stein, R. F., & Asplund, M. 2009, Living Reviews in Solar Physics, 6, 2

O'Brian, T. R., & Lawler, J. E. 1991, Phys. Rev. A, 44, 7134, (BL)

O'Brian, T. R., Wickliffe, M. E., Lawler, J. E., Whaling, W., & Brault, J. W. 1991, Journal of the Optical Society of America B Optical Physics, 8, 1185, (BWL)

Önehag, A., Gustafsson, B., & Korn, A. 2014, A&A, 562, A102

Osorio, Y., Barklem, P. S., Lind, K., et al. 2015, A&A, 579, A53

Osorio, Y., Lind, K., Barklem, P. S., Allende Prieto, C., & Zatsarinny, O. 2019, A&A, 623, A103

Ouazzani, R. M., Marques, J. P., Goupil, M. J., et al. 2019, A&A, 626, A121

Palla, M. 2021, MNRAS, 503, 3216

Palme, H., Lodders, K., & Jones, A. 2014, Solar System Abundances of the Elements, ed. A. M. Davis, Vol. 2, 15–36

Pancino, E., Carrera, R., Rossetti, E., & Gallart, C. 2010, A&A, 511, A56

Park, J., Kucharek, H., Möbius, E., et al. 2014, ApJ, 795, 97

Pehlivan Rhodin, A., Hartman, H., Nilsson, H., & Jönsson, P. 2017, A&A, 598, A102

Pinsonneault, M. H., & Delahaye, F. 2009, ApJ, 704, 1174

Piskunov, N., & Valenti, J. A. 2017, A&A, 597, A16

Piskunov, N. E., Kupka, F., Ryabchikova, T. A., Weiss, W. W., & Jeffery, C. S. 1995, A&AS, 112, 525

Plez, B. 2012, Turbospectrum: Code for spectral synthesis, ascl:1205.004

Pont, F., & Eyer, L. 2004, MNRAS, 351, 487

Price-Whelan, A. M., Hogg, D. W., Rix, H.-W., et al. 2020, arXiv e-prints, arXiv:2002.00014

Proffitt, C. R., & Michaud, G. 1991, ApJ, 380, 238

Prša, A., Harmanec, P., Torres, G., et al. 2016, The Astronomical Journal, 152, 41

Quinet, P., Palmeri, P., Biémont, E., et al. 2002, Journal of alloys and compounds, 344, 255

Quinet, P., Palmeri, P., Biémont, E., et al. 1999, MNRAS, 307, 934

Raassen, A. J. J., & Uylings, P. H. M. 1998, A&A, 340, 300

Ramírez, S. V., & Cohen, J. G. 2003, in IAU Symposium, Vol. 210, Modelling of Stellar Atmospheres, ed. N. Piskunov, W. W. Weiss, & D. F. Gray, D2

Randich, S., Gilmore, G., & Gaia-ESO Consortium. 2013, The Messenger, 154, 47

Randich, S., Sestito, P., Primas, F., Pallavicini, R., & Pasquini, L. 2006, A&A, 450, 557

Reames, D. V. 1998, Space Sci. Rev., 85, 327

Recio-Blanco, A., de Laverny, P., Kordopatis, G., et al. 2014, A&A, 567, A5

Reetz, J. 1991, Diplomarbeit, Universität München

Reetz, J. 1999, Ap&SS, 265, 171

Reggiani, H., Amarsi, A. M., Lind, K., et al. 2019, A&A, 627, A177

Reiners, A., Mrotzek, N., Lemke, U., Hinrichs, J., & Reinsch, K. 2016, A&A, 587, A65

Richard, O. 2005, in EAS Publications Series, ed. G. Alecian, O. Richard, & S. Vauclair, Vol. 17, 43–52

Richard, O., Michaud, G., & Richer, J. 2001, ApJ, 558, 377

—. 2002, ApJ, 580, 1100

Richer, J., Michaud, G., & Proffitt, C. R. 1992, ApJS, 82, 329

Richer, J., Michaud, G., Rogers, F., et al. 1998, ApJ, 492, 833

Richer, J., Michaud, G., & Turcotte, S. 2000, ApJ, 529, 338

Roederer, I. U., & Lawler, J. E. 2021, ApJ, 912, 119

Rogers, F. J., & Nayfonov, A. 2002, ApJ, 576, 1064

Ruchti, G. R., Bergemann, M., Serenelli, A., Casagrande, L., & Lind, K. 2013, MNRAS, 429, 126

Ruffoni, M. P., Den Hartog, E. A., Lawler, J. E., et al. 2014, MNRAS, 441, 3127

Rutten, R. J. 2003, Radiative Transfer in Stellar Atmospheres

Ryabchikova, T., Piskunov, N., Kurucz, R. L., et al. 2015, Phys. Scr, 90, 054005

Sakari, C. M., Placco, V. M., Farrell, E. M., et al. 2018, ApJ, 868, 110

Salaris, M. 2016, Astronomische Nachrichten, 337, 805

Salaris, M., & Cassisi, S. 2017, Royal Society Open Science, 4, 170192

Salaris, M., Pietrinferni, A., Piersimoni, A. M., & Cassisi, S. 2015, A&A, 583, A87

Schönrich, R., & Bergemann, M. 2014, MNRAS, 443, 698

Schönrich, R., & Binney, J. 2009, MNRAS, 396, 203

Schuler, S. C., Andrews, J. J., Clanzy, V. R., et al. 2021, AJ, 162, 109

Scott, P., Asplund, M., Grevesse, N., Bergemann, M., & Sauval, A. J. 2015a, A&A, 573, A26

Scott, P., Grevesse, N., Asplund, M., et al. 2015b, A&A, 573, A25

Seaton, M. J. 1962, in Atomic and Molecular Processes, ed. D. R. Bates, 375

Seaton, M. J. 2005, MNRAS, 362, L1

Semenova, E., Bergemann, M., Deal, M., et al. 2020, A&A, 643, A164

Serenelli, A., Johnson, J., Huber, D., et al. 2017, ApJS, 233, 23

Serenelli, A. M. 2010, Ap&SS, 328, 13

Serenelli, A. M., Basu, S., Ferguson, J. W., & Asplund, M. 2009, ApJ, 705, L123

Serenelli, A. M., Bergemann, M., Ruchti, G., & Casagrande, L. 2013, MNRAS, 429, 3645

Serenelli, A. M., Haxton, W. C., & Peña-Garay, C. 2011, ApJ, 743, 24

Sharma, S., Pandey, A. K., Ogura, K., et al. 2006, AJ, 132, 1669

Shi, J. R., Gehren, T., Butler, K., Mashonkina, L. I., & Zhao, G. 2008, A&A, 486, 303

Siegel, M. H., LaPorte, S. J., Porterfield, B. L., Hagen, L. M. Z., & Gronwall, C. A. 2019, AJ, 158, 35

Sitnova, T., Zhao, G., Mashonkina, L., et al. 2015, ApJ, 808, 148

Smiljanic, R., Pasquini, L., Charbonnel, C., & Lagarde, N. 2010, in IAU Symposium, Vol. 268, Light Elements in the Universe, ed. C. Charbonnel, M. Tosi, F. Primas, & C. Chiappini, 357–358

Smiljanic, R., Korn, A. J., Bergemann, M., et al. 2014, A&A, 570, A122

Smith, G. 1988, Journal of Physics B Atomic Molecular Physics, 21, 2827, (S)

Smith, G., & Raggett, D. S. J. 1981, Journal of Physics B Atomic Molecular Physics, 14, 4015, (SR)

Sonoi, T., Samadi, R., Belkacem, K., et al. 2015, A&A, 583, A112

Souto, D., Cunha, K., Smith, V. V., et al. 2018, ApJ, 857, 14

Souto, D., Allende Prieto, C., Cunha, K., et al. 2019, ApJ, 874, 97

Spite, F., & Spite, M. 1982, A&A, 115, 357

Steinmetz, M., Guiglion, G., McMillan, P. J., et al. 2020, AJ, 160, 83

Storey, P. J., & Zeippen, C. J. 2000, MNRAS, 312, 813

Takeda, Y., Hashimoto, O., Taguchi, H., et al. 2005, PASJ, 57, 751

The Opacity Project Team. 1995, The opacity project (Institute of Physics Publications, Bristol, UK)

Théado, S., Vauclair, S., Alecian, G., & LeBlanc, F. 2009, ApJ, 704, 1262

Thévenin, F., Charbonnel, C., de Freitas Pacheco, J. A., et al. 2001, A&A, 373, 905

Timmes, F. X., Woosley, S. E., & Weaver, T. A. 1995, ApJS, 98, 617

Tremblay, P.-E., Ludwig, H.-G., Freytag, B., Steffen, M., & Caffau, E. 2013, A&A, 557, A7

Turcotte, S., Richer, J., & Michaud, G. 1998, ApJ, 504, 559

Uitenbroek, H., & Criscuoli, S. 2011, ApJ, 736, 69

Ulrich, R. K. 1986, ApJ, 306, L37

Unsöld, A. 1955, Physik der Sternatmospharen, MIT besonderer Berucksichtigung der Sonne.

van Regemorter, H. 1962, ApJ, 136, 906

Vauclair, S. 1999, in Astronomical Society of the Pacific Conference Series, Vol. 171, LiBeB Cosmic Rays, and Related X- and Gamma-Rays, ed. R. Ramaty, E. Vangioni-Flam, M. Cassé, & K. Olive, 48

Verma, K., & Silva Aguirre, V. 2019, MNRAS, 489, 1850

Vick, M., Michaud, G., Richer, J., & Richard, O. 2013, A&A, 552, A131

Villante, F. L., Serenelli, A. M., Delahaye, F., & Pinsonneault, M. H. 2014, ApJ, 787, 13

Vincent, A. C., Scott, P., & Serenelli, A. 2015, Phys. Rev. Lett., 114, 081302

Vinyoles, N., Serenelli, A. M., Villante, F. L., et al. 2017, ApJ, 835, 202

Vögler, A., & Schüssler, M. 2007, A&A, 465, L43

Voronov, Y. V., Yakovleva, S. A., & Belyaev, A. K. 2022, ApJ, 926, 173

Watson, D., Hansen, C. J., Selsing, J., et al. 2019, Nature, 574, 497

Weiss, A., & Schlattl, H. 2008, Ap&SS, 316, 99

Widing, K. G. 1997, ApJ, 480, 400

Wolnik, S. J., Berthel, R. O., & Wares, G. W. 1971, ApJ, 166, L31+, (WBW)

Wood, M. P., Lawler, J. E., Sneden, C., & Cowan, J. J. 2014, ApJS, 211, 20

Woosley, S. E., & Weaver, T. A. 1995, ApJS, 101, 181

Yakovleva, S. A., Belyaev, A. K., & Bergemann, M. 2020, Atoms, 8, 34

Yong, D., Grundahl, F., Nissen, P. E., Jensen, H. R., & Lambert, D. L. 2005, A&A, 438, 875

Young, P. R. 2005, A&A, 444, L45

—. 2018, ApJ, 855, 15

Zhang, H. W., Butler, K., Gehren, T., Shi, J. R., & Zhao, G. 2006, A&A, 453, 723

Zhang, Q.-S., Li, Y., & Christensen-Dalsgaard, J. 2019, ApJ, 881, 103

Zhao, G., Butler, K., & Gehren, T. 1998, A&A, 333, 219

Zhao, G., Mashonkina, L., Yan, H. L., et al. 2016, ApJ, 833, 225

Zhou, Y., Asplund, M., & Collet, R. 2019, ApJ, 880, 13

Zhou, Y., Nordlander, T., Casagrande, L., et al. 2021, MNRAS, 503, 13

Acronyms

⟨3D⟩ average 3D. 24, 29

1D one-dimensional. 19, 23, 24, 26, 29, 40, 43–45

3D three-dimensional. 24–26, 103, 104, 106

CoG curve of growth. 15, 28, 69

GCE Galactic chemical evolution. 99–101, 104, 106

LTE local thermodynamic equilibrium. 2, 9, 18, 21, 22, 25, 26, 28, 29, 31, 40, 42, 44–46, 63, 64, 66, 67, 77, 97, 100, 103

MHD magnetohydrodynamical. 24

MS main-sequence. 34, 35, 38, 46, 50, 55, 57–59

NLTE not assuming local thermodynamic equilibrium. 2, 3, 9, 10, 20, 22, 25, 26, 28–32, 40, 42–46, 55, 56, 61, 63, 64, 66, 69, 70, 73, 75, 77, 81, 96, 97, 100–107

RGB red giant branch. 33–35, 39, 45, 55–58, 61–64

SGB sub-giant branch. 34, 55, 58

SN supernova. 3, 5–7, 21, 99, 100, 104, 106

SNR signal-to-noise ratio. 36, 100

SSM standard solar model. 66, 79, 88, 92, 93, 95–97

TO turn-off. 34, 35, 39, 43, 46, 55, 61